# Highly-Ionized High-Velocity Gas In the Vicinity of the Galaxy

K.R. Sembach<sup>1</sup>, B.P. Wakker<sup>2</sup>, B.D. Savage<sup>2</sup>, P. Richter<sup>2,3</sup>, M. Meade<sup>2</sup>, J.M. Shull<sup>4</sup>, E.B. Jenkins<sup>5</sup>, G. Sonneborn<sup>6</sup>, and H.W. Moos<sup>7</sup>

#### ABSTRACT

We report the results of a FUSE study of high velocity O VI absorption along complete sight lines through the Galactic halo in directions toward 100 extragalactic objects and 2 halo stars. The high velocity O VI traces a variety of phenomena, including tidal interactions with the Magellanic Clouds, accretion of gas, outflowing material from the Galactic disk, warm/hot gas interactions in a highly extended Galactic corona, and intergalactic gas in the Local Group. We identify 85 high velocity O VI features at  $\geq 3\sigma$  confidence at velocities of  $-500 < v_{LSR} < +500$  km s<sup>-1</sup>. There are an additional 6 confirmed or very likely (> 90% confidence) features plus 2 tentative detections between  $v_{LSR} = +500$  and +1200 km s<sup>-1</sup>; these very high velocity O VI features trace intergalactic gas beyond the Local Group. The 85 O VI features have velocity centroids ranging from  $-372 \lesssim \bar{v}_{LSR} \lesssim -90 \text{ km s}^{-1} \text{ to } +93 \lesssim \bar{v}_{LSR} \lesssim +385 \text{ km s}^{-1}$ , line widths b  $\,\sim 16-81~{\rm km\,s^{-1}}$  with an average of  $\langle \rm b \rangle = 40\pm14~{\rm km\,s^{-1}},$  and an average O VI column density  $\langle \log N \rangle = 13.95 \pm 0.34$  with a median value of 13.97. Values of b greater than the 17.6 km s<sup>-1</sup> thermal width expected for O VI at  $T \sim 3 \times 10^5$  K indicate that additional non-thermal broadening mechanisms are common. The O VI  $\lambda 1031.926$  absorption is detected at  $\geq 3\sigma$  confidence along 59 of the 102 sight lines surveyed. The high velocity O VI detections indicate that  $\sim 60\%$  of the sky (and perhaps as much as  $\sim 85\%$ , depending on data quality considerations) is covered by high velocity  $H^+$ associated with the O VI.  $N({\rm H}^+) \gtrsim 4 \times 10^{16}~{\rm cm}^{-2}$  if the high velocity hot gas has a metallicity similar to that of the Magellanic Stream. About 30% of the sky is covered

<sup>&</sup>lt;sup>1</sup>Space Telescope Science Institute, 3700 San Martin Dr., Baltimore, MD 21218 (sembach@stsci.edu

<sup>&</sup>lt;sup>2</sup>Department of Astronomy, University of Wisconsin, 475 N. Charter St., Madison, WI 53706

<sup>&</sup>lt;sup>3</sup>Current address: Observatorio Astrofisico di Arcetri, Largo E. Fermi 5, Florence, Italy

<sup>&</sup>lt;sup>4</sup>Center for Astrophysics and Space Astronomy, Department of Astrophysical and Planetary Sciences, University of Colorado, Boulder, CO 80309

<sup>&</sup>lt;sup>5</sup>Princeton University Observatory, Peyton Hall, Princeton, NJ 08544

<sup>&</sup>lt;sup>6</sup>Laboratory for Astronomy and Solar Physics, Code 681, NASA Goddard Space Flight Center, Greenbelt, MD 20771

<sup>&</sup>lt;sup>7</sup>Department of Physics & Astronomy, The Johns Hopkins University, 3400 N. Charles St., Baltimore, MD 21218

by the hot, high velocity H<sup>+</sup> at a level of  $N({\rm H}^+) \gtrsim 4 \times 10^{17}~{\rm cm}^{-2}$ , which is similar to the detection rate found for H I 21 cm emission produced by warm neutral gas at a comparable column density level. Some of the high velocity O VI is associated with known H I structures (the Magellanic Stream, Complex A, Complex C, the Outer Spiral Arm, and several discrete H I HVCs). Some of the high velocity O VI features have no counterpart in H I 21 cm emission, including discrete absorption features and positive velocity absorption wings extending from  $\sim 100$  to  $\sim 300$  km s<sup>-1</sup> that blend with lower velocity absorption produced by the Galactic thick disk/halo. The discrete features may typify clouds located in the Local Group, while the O VI absorption wings may be tidal debris or material expelled from the Galactic disk. Most of the O VI features have velocities incompatible with those of the Galactic halo, even if the halo has decoupled from the underlying Galactic disk. The reduction in the dispersion about the mean of the high velocity O VI centroids when the velocities are converted from the LSR to the GSR and LGSR reference frames is necessary (but not conclusive) evidence that some of the clouds are located outside the Galaxy. Most of the O VI cannot be produced by photoionization, even if the gas is irradiated by extragalactic ultraviolet background radiation. Several observational quantities indicate that collisions in hot gas are the primary ionization mechanism responsible for the production of the O VI. These include the ratios of O VI column densities to those of other highly ionized species (C IV, N V) and the strong correlation between N(O VI) and O VI line width. Consideration of the possible sources of collisional ionization favors production of some of the O VI at the boundaries between cool/warm clouds of gas and a highly extended  $(R \gtrsim 70 \text{ kpc})$ , hot  $(T > 10^6 \text{ K})$ , low-density  $(n \lesssim 10^{-4} - 10^{-5} \text{ cm}^{-3})$  Galactic corona or Local Group medium. The existence of a hot, highly extended Galactic corona or Local Group medium and the prevalence of high velocity O VI are consistent with predictions of current galaxy formation scenarios. Distinguishing between the various phenomena producing high velocity O VI in and near the Galaxy will require continuing studies of the distances, kinematics, elemental abundances, and physical states of the different types of high velocity O VI found in this study. Descriptions of galaxy evolution will need to account for the highly ionized gas, and future X-ray studies of hot gas in the Local Group will need to consider carefully the relationship of the X-ray absorption/emission to the complex high velocity absorption observed in O VI.

Subject headings: Galaxy: halo – intergalactic medium – ISM: clouds – ISM: evolution – ISM: kinematics and dynamics – ultraviolet: ISM

#### 1. INTRODUCTION

Understanding galaxy formation and evolution requires observational information about hot, highly ionized gas in and near galaxies. Numerical simulations of cosmological structure formation in the presence of cold dark matter indicate that a significant fraction of the baryonic material at low redshift should be shock-heated to temperatures of  $10^5 - 10^7$  K as the gas collapses and forms clusters and groups of galaxies (e.g., Cen & Ostriker 1999; Davé et al. 1999, 2001). This reservoir of hot gas is detectable through ultraviolet absorption-line measurements (Tripp, Savage, & Jenkins 2000; Savage et al. 2002a), but a complete picture of how the hot gas in galaxies and the intergalactic medium (IGM) are related does not yet exist because a variety of internal and external processes affect the heating and distribution of the interstellar gas in and around galaxies. In addition to the galaxy formation process, the accretion of satellite galaxies, tidal interactions, star formation, galactic winds, and galaxy-IGM interactions may all contribute to the production of hot gas. To some extent, all of these activities operate in and around our own galaxy, so studying the hot gas in the immediate environment of the Milky Way is a logical step in assessing the relevance and roles of these processes locally.

One of the primary science objectives of the Far Ultraviolet Spectroscopic Explorer (FUSE) mission is to determine the properties of hot, highly ionized gas in the low-redshift universe. A key component of this research has been the study of O VI absorption along many sight lines through the Galactic halo. Such observations were not possible until FUSE was launched because previous observatories lacked either the spectral resolution or sensitivity to study the velocity structure of the O VI absorption toward distant background sources. Among the most interesting results to date is the detection of O VI in high velocity clouds (HVCs) (Sembach et al. 2000; Murphy et al. 2000). For decades astronomers have studied the neutral (H I) content of the clouds and have debated the origin and location of the high velocity gas. While it is generally accepted that no single model can account for all of the observed properties of the H I HVCs (see Wakker & van Woerden 1997 for a review), there is no unanimity on the fundamental properties of the different types of HVCs. With the re-introduction of the idea that some of the H I HVCs could be located outside of the Milky Way if they are embedded in halos of dark matter (Blitz et al. 1999), the possible range of locations and cloud properties has widened. Determining the ionization and hot gas content of the high velocity gas bears directly on the locations of the clouds and their interactions with other components of the gaseous interstellar and intergalactic media.

The O VI  $\lambda\lambda 1031.926, 1037.617$  doublet lines in the far-ultraviolet spectral region are the best lines to use for kinematical investigations of hot  $(T\gtrsim 10^5-10^6\,\mathrm{K})$  gas in the low-redshift universe. Oxygen is the most abundant element heavier than helium, and the O VI lines have large oscillator strengths  $(f_{1032}=0.133,\,f_{1038}=0.0661;\,\mathrm{Morton}\,1991)$ . X-ray spectroscopy of higher ionization lines (e.g., O VII, O VIII) is possible with XMM-Newton and the Chandra X-ray Observatory for a small number of sources, but the spectral resolution  $(\mathrm{R}\equiv\lambda/\Delta\lambda\lesssim1000)$  is modest compared to that afforded by FUSE (R  $\sim 15,000$ ). Lower ionization lines observable at high spectral resolution at ultraviolet wavelengths are generally either much weaker than the O VI lines (e.g., N V  $\lambda\lambda1238.821,1242.804$ ) or are better tracers of collisionally ionized gas at temperatures  $T\lesssim10^5\,\mathrm{K}$  (e.g., C IV  $\lambda\lambda1548.195,1550.770$ , C III  $\lambda977.020$ , Si IV  $\lambda\lambda1393.755,1402.770$ , Si III  $\lambda1206.500$ ). This latter set of ions is also considerably more susceptible to photoionization than

O VI since the photoionization cross sections of the ions are large and the ionization potentials are less than 54 eV, the energy of the He II ionization edge. O VI can be produced by photoionization under special conditions involving a hard radiation field and a very low gas density, but as we will show later, this does not appear to be a viable production mechanism for *most* of the O VI observed in and near the Milky Way.

This article is one in a series of three papers devoted to FUSE observations of O VI absorption along complete paths through the Galactic halo in the directions of quasars, active galactic nuclei (AGNs), and BL Lac objects. The other two papers include a catalog with basic measurements and illustrations of all of the O VI profiles obtained in the survey (Wakker et al. 2002) and a companion study of the O VI absorption associated with the thick disk of the Milky Way (Savage et al. 2002b). Here, we concentrate on the properties of the O VI absorption at high velocities with respect to those expected for gas participating in differential Galactic rotation (generally, "high velocity" refers to  $100 < |v_{LSR}| < 400 \text{ km s}^{-1}$  in this paper). High velocity O VI absorption associated with the Magellanic Clouds is discussed elsewhere (Friedman et al. 2000; Danforth et al. 2002; Hoopes et al. 2001, 2002; Howk et al. 2002b).

This paper is organized as follows. In §2 we describe the observations and data reduction. We present the O VI HVC measurements in §3 and describe the general types of high velocity gas seen in §4. Section 5 contains information about the column densities, sky covering fractions, velocities, and line widths of the O VI absorption. In §6 we discuss the high velocity O VI features associated with previously identified high velocity clouds, while §7 specifies the few sight lines that show high velocity H I 21 cm emission with no corresponding O VI absorption. Section 8 highlights new high velocity gas detected only in O VI absorption. In §9 we consider how the high velocity gas is ionized. Section 10 describes the general kinematical behavior of the high velocity gas. Section 11 contains a discussion of the high velocity O VI features and the implications of this work for understanding hot gas in the low-redshift universe. We conclude with a summary of results in §12.

## 2. OBSERVATIONS AND DATA REDUCTION

Full details of the FUSE observations and data reduction for the objects surveyed for high velocity O VI are given by Wakker et al. (2002). We summarize some of the key points here. The objects included in this study form an incomplete flux-limited sample of extragalactic objects drawn primarily from the FUSE Science Team O VI, D/H, and AGN programs conducted in the first two years of the mission (December 1999 – November 2001). Publicly available Guest Investigator (GI) observations have been included when it is clear that the science goals of our study and those of the GI do not conflict. Most of the objects are either quasars or low-redshift Type 1 Seyfert galaxy nuclei, which have relatively smooth continua in the wavelength region of interest. A few additional background sources, such as bright regions of low-redshift starburst galaxies and two high latitude stars located > 5 kiloparsecs from the Galactic disk, have been included as well. Neither stellar sight line included in the sample (vZ 1128, PG 0832+675) shows evidence of high velocity O VI

absorption. Of the more than two hundred objects considered, only about half had data suitable for studies of the O VI lines. Total exposure times ranged from  $\sim 5$  ksec to  $\sim 600$  ksec per object, with a median of  $\sim 16$  ksec per object.

FUSE contains four co-aligned spectrographs that cover the 905–1187 Å spectral region. The optics (a mirror and a holographically-ruled diffraction grating) in two of the channels are coated with aluminum and lithium-fluoride (LiF) for maximum throughput above 1000 Å. The other two channels contain optics with SiC coatings for maximum throughput below 1000 Å. Each object was centered in the  $30'' \times 30''$  (LWRS) aperture of the LiF1 channel, which is also the channel used for guiding. In the remaining channels, the objects sometimes drifted around in the LWRS apertures. These drifts do not affect our study since each photon event recorded by the microchannel plate detectors is time-tagged and can be corrected for these motions. Descriptions of the FUSE instrumentation and on-orbit performance are given by Moos et al. (2000, 2002) and Sahnow (2000a, 2000b). Additional information can be found in the FUSE Observer's Guide.

All of the data were reduced in a homogeneous fashion with the standard FUSE pipeline software (CALFUSE v1.8.7) available from the Johns Hopkins University. The O VI lines are covered by all four FUSE channels, but we have opted to use data from only the two most sensitive channels (LiF1, LiF2), which have optics coated with Al+LiF. These two channels account for roughly 76% of the FUSE effective area at the wavelengths of the O VI lines. For the higher signal-to-noise ratio (S/N) observations, we used only the data from the LiF1 channel and checked this result with the LiF2 data. However, we combined the two independent measurements for lower S/N observations to increase the detection confidence (see Wakker et al. 2002). To maximize S/N, we used data obtained during both orbital day and night since the O VI lines are in spectral regions unaffected by terrestrial airglow emission. The fully sampled FUSE data have a FWHM velocity resolution of  $\sim 20-25~{\rm km\,s^{-1}}$  ( $R \sim 12,000-15,000$ ).

We set the zero point of the FUSE wavelength scale for each observation by referencing the observed Ar I  $\lambda 1048.220$  and Si II  $\lambda 1020.699$  absorption features to the H I 21 cm emission observed in each direction [see Wakker et al. (2002) for a description of the method and information about the H I data used in these comparisons]. This comparison was done for the low velocity portions of the profiles. H<sub>2</sub> absorption features in the 1020–1040 Å spectral region provided an additional consistency check on the wavelength scales for some sight lines. We estimate a wavelength uncertainty of  $\sim 0.03$  Å ( $\sim 10~{\rm km\,s^{-1}}$ ) for the fully reduced data. None of the conclusions of this study are affected by this zero-point uncertainty. Unless otherwise specified, all velocities in this

<sup>&</sup>lt;sup>8</sup>On-line at http://fuse.pha.jhu.edu/support/guide/guide.html.

 $<sup>^9</sup>$ For a subset of the observations, we compared the CALFUSE v1.8.7 processed data to the data processed with the latest (v2.0.5) available software. We found no significant differences in the reduced datasets in the spectral regions considered in this study, except for  $\sim \pm 30~{\rm km\,s^{-1}}$  differences in the velocity calibration. See Wakker et al. (2002) for additional information about the zero-point velocity scale differences between the two processing versions for objects in our sample.

paper are referred to the Local Standard of Rest (LSR) reference frame, which has a standard solar motion of 19.5 km s<sup>-1</sup> in the direction  $l_{std} = 56^{\circ}$ ,  $b_{std} = 23^{\circ}$  (Mihalas & Binney 1981).

Figure 1 contains the fully reduced FUSE spectra between 1015 Å and 1040 Å for three sight lines through the Galactic halo (NGC 7469, PG 1116+215, and PG 1259+593). These sight lines exhibit varying degrees of complexity in their observed O VI absorption and in the amount of blending with other atomic and molecular lines in the bandpass. All three sight lines contain high velocity O VI absorption that is observable in the 1031.926 Å line. Toward NGC 7469 and PG 1259+593, the high velocity O VI  $\lambda$ 1037.617 absorption is blended with either C II\*  $\lambda$ 1037.012 or with nearby molecular hydrogen lines, whose wavelengths are indicated in the top panel. Similar illustrations of high velocity O VI absorption observed toward AGNs and QSOs by FUSE in this spectral region are given by Oegerle et al. (2000), Savage et al. (2000, 2002a, 2002b), Sembach et al. (2000, 2001b), and Heckman et al. (2001).

#### 3. MEASUREMENTS

In our study of high velocity O VI, we draw upon the measurements and detailed sight line comments presented in the FUSE O VI catalog paper (Wakker et al. 2002) for the 102 objects with sufficient data quality to study the absorption. The catalog contains information about line strengths (equivalent widths), velocities, and contamination by other absorption features. The catalog includes illustrations of the observed absorption profiles and some basic statistical information about the properties of the absorption and data quality. We present a complete list of the high velocity O VI features in Table 1, sorted by Galactic longitude. The table entries include the name of the background continuum source observed, the Galactic coordinates (l,b) of the background source, a data quality factor (Q), an "identification" (ID) for the high velocity O VI absorption based on the correspondence with Galactic structures or high velocity gas observed in H I 21 cm emission, the velocity range spanned by the O VI  $(v_{min}, v_{max})$ , the average velocity and width of the O VI absorption ( $\bar{v}$  and b), the logarithmic column density, and the significance of the O VI  $\lambda 1031.926$  absorption-line detection  $(W_{\lambda}/\sigma_W)$ , where  $\sigma_W$  is the error in the equivalent width due to statistical noise fluctuations and continuum placement uncertainties). The data quality factor is an indicator of the continuum S/N (per 20 km s<sup>-1</sup> resolution element) in the spectrum near the O VI lines as follows: Q = 1 (S/N = 3 - 5), Q = 2 (S/N = 5 - 9), Q = 3 (S/N = 9 - 14),  $Q = 4 \ (S/N > 14).$ 

## 3.1. Identifying the High Velocity O VI Absorption

The derived properties of the high velocity gas depend in part upon the adopted separation of the high velocity absorption from lower velocity absorption arising in the nearby Galactic disk and halo. In regions of the sky where there is little high velocity gas observed in other species (e.g., H I, C II, C IV), the nearby O VI absorption is generally found at  $-100 \le v_{LSR} \le +100$  km s<sup>-1</sup>, which we adopt as the typical velocity range of the Galactic thick disk and halo O VI absorption (see Savage et al. 2002b). We define absorption outside this velocity range as high velocity gas, with a few minor exceptions to account for directions where there is reason to believe that the thick disk absorption extends to higher velocities. For example, differential Galactic rotation may broaden the profiles in some directions, particularly low latitude sight lines in the  $l = 90^{\circ}$  and  $l = 270^{\circ}$  directions, as well as at longitudes in the general direction of the Galactic center. In a few cases we contracted the thick disk limits and allowed the high velocity gas integration to extend to lower velocities by  $\sim 10 - 20$  km s<sup>-1</sup> to account for absorption associated with known high velocity features (e.g., Mrk 817, which exhibits O VI absorption in Complex C at velocities  $v_{LSR} < -90$  km s<sup>-1</sup>). For 5 lines of sight, the separation is based on O VI velocity structure. We list the integration limits ( $v_{min}$ ,  $v_{max}$ ) for the high velocity gas in Table 1.

We examined the FUSE spectra for absorption produced by the stronger member of the O VI  $\lambda\lambda 1031.926, 1037.617$  doublet because the higher velocity portions of the weaker line ( $\lambda 1037.617$ ) are usually severely blended with other interstellar lines. We searched for absorption at velocities  $-1200 < v_{LSR} < +1200 \text{ km s}^{-1}$ , and with few exceptions all of the identified O VI absorption is confined to the  $|v_{LSR}| < 400 \text{ km s}^{-1}$  velocity range. The few possible cases where higher velocity features may be present are described in Appendix A of the O VI catalog (Wakker et al. 2002) and are not considered further here.

The identification of high velocity O VI  $\lambda 1031.926$  requires careful consideration of the absorption produced by nearby lines of other atomic and molecular species (see Sembach 1999 for model templates of the absorption in the FUSE bandpass). At negative velocities, the primary lines that blend with O VI  $\lambda 1031.926$  are the H<sub>2</sub> (6–0) P(3) line at 1031.191 Å (–214 km s<sup>-1</sup> with respect to the rest wavelength of the O VI line) and the Cl I lines at 1031.885 Å (-303 km s<sup>-1</sup>) and  $1031.507 \,\mathrm{\mathring{A}} \,(-122 \,\mathrm{km}\,\mathrm{s}^{-1})$ . At positive velocities, the primary contaminant is the H<sub>2</sub> (6–0) R(4) line at  $1032.349 \,\text{Å} \,(+123 \,\text{km}\,\text{s}^{-1})$ . Of these, the  $H_2$  lines are the most important, since even small  $H_2$  column densities in the J=3 or J=4 rotational levels produce detectable absorption lines;  $20\,\mathrm{mÅ}$  features correspond to  $N_J$  as low as  $(1-2)\times 10^{14}~\mathrm{cm}^{-2}$  (see, e.g., Figure 1, top panel). We carefully modeled the strengths of the  $H_2$  J=3 and J=4 lines in the O VI wavelength region using other H<sub>2</sub> lines in the same rotational levels at other wavelengths (see Wakker et al. 2002 for a description of the procedure). A weak transition of Co II at 1031.542 Å (-112 km s<sup>-1</sup>) produces negligible absorption along the low-density sight lines studied in this work.<sup>10</sup> The deuterated hydrogen HD (6-0) R(0)  $\lambda$ 1031.912 line, which occurs at low velocities (-4 km s<sup>-1</sup> with respect to O VI  $\lambda 1031.926$ ), can be important for studies of the interstellar medium (ISM) in the Galactic disk and halo but has not yet been observed in absorption at high velocities. HD is detected toward only one object in our sample (NGC 7469, at low velocity) and is not important for our study of

<sup>&</sup>lt;sup>10</sup>For  $N(\text{H\,I}) = 10^{21} \text{ cm}^{-2}$ , a cosmic (meteoritic) abundance ratio (Co/H) = 8.13 × 10<sup>-8</sup> (Anders & Grevesse 1989), and a typical interstellar Co depletion  $\delta_{Co} \leq 0.03$  (Federman et al. 1993), we expect  $W_{1032}(\text{Co\,II}) \ll 1 \text{ mÅ}$ .

the high velocity gas along this sight line, though it must be accounted for in our study of the halo gas in this direction (Savage et al. 2002b).

Another possible source of confusion with the high velocity O VI  $\lambda 1031.926$  absorption is redshifted H I and metal-line absorption in the intergalactic medium along the sight line or in the immediate environment of the QSO/AGN. The most important lines to search for within  $\pm 500$  km s<sup>-1</sup> of the O VI  $\lambda 1031.926$  line are H I Ly $\beta$  ( $z \sim 0.0044 - 0.0077$ ) and H I Ly $\gamma$  ( $z \sim 0.0593 - 0.0628$ ), but we also found instances of H I Ly $\delta$  ( $z \sim 0.0847 - 0.0883$ ), H I Ly $\epsilon$  ( $z \sim 0.0985 - 0.1022$ ), C III  $\lambda 977.020$  ( $z \sim 0.054 - 0.0580$ ), Si II  $\lambda 1020.699$  ( $z \sim 0.0093 - 0.0127$ ), and S III  $\lambda 1012.502$  ( $z \sim 0.0175 - 0.0209$ ). Whenever possible, we have checked existing Hubble Space Telescope (HST) data for corresponding Ly $\alpha$  absorption or FUSE data for other H I Lyman series lines to confirm or refute such identifications. The middle and bottom panels of Figure 1 contain several examples of intervening absorption lines arising in the IGM. We refer the reader to Wakker et al. (2002) for comments about IGM absorption features near the O VI lines.

## 3.2. Column Densities

We derived the column densities listed in Table 1 from the apparent optical depths of the O VI  $\lambda 1031.926$  absorption lines under the assumption that there is no unresolved saturated structure in the profiles. The apparent column density as a function of velocity,  $v \, (\text{km s}^{-1})$ , is given by  $N_a(v) = (m_e c)(\pi e^2)^{-1} \tau_a(v) (f\lambda)^{-1} = 3.768 \times 10^{14} \tau_a(v) (f\lambda)^{-1} [\text{cm}^{-2} (\text{km s}^{-1})^{-1}], \text{ where the}$ wavelength  $\lambda$  is given in Ångstroms, and the optical depth is related to the estimated continuum intensity and the observed line intensity through the relation  $\tau_a(v) = \ln[I_c(v)/I(v)]$ . The  $N_a(v)$ profiles represent valid, instrumentally-blurred versions of the actual column density profiles when no unresolved saturated structures are present or when the absorption is weak  $(\tau_{max} \lesssim 1-3)$ . In such cases,  $N = \int N(v)dv = \int N_a(v)dv$ ; see Savage & Sembach (1991) for a discussion of the applicability of the apparent optical depth method and uncertainties involved in calculating column densities from  $N_a(v)$  profiles. At the spectral resolution afforded by FUSE, the O VI lines are fully resolved for gas at temperatures  $T \gtrsim 1.4 \times 10^5 \, \mathrm{K}$ . At lower temperatures, the lines may still be resolved if the turbulent motions in the cloud are modest. For example, if  $b_{turb} \approx 8 \text{ km s}^{-1}$ , the lines will be resolved for  $T \gtrsim 8 \times 10^4 \,\mathrm{K}$ . At lower temperatures, the abundance of O VI in collisionally ionized gas is expected to be less than a few percent of the total oxygen abundance, even in non-equilibrium cooling situations (Shapiro & Moore 1976).

We report two errors for each of the column densities in Table 1. The first error  $(\sigma_{sc})$  is a quadrature addition of the uncertainties associated with continuum placement and statistical (Poisson) noise propagated through the line profile following the procedures outlined by Sembach & Savage (1992). This error accounts for most of the uncertainty involved in making an objective estimate of the line strength. The second error  $(\sigma_{sys})$  is a quadrature addition of systematic uncertainties accounting for fixed-pattern noise, choice of velocity integration limits, and removal of H<sub>2</sub> features. This error, which often dominates the total error, accounts for some of the more

subjective decisions that must be made when measuring the line strength. To be conservative, we have made generous allowances for the various components of  $\sigma_{sys}$ . The fixed-pattern noise component of the systematic error accounts for an intensity uncertainty of  $\sim 10\%$  integrated over the width of one resolution element. Fixed-pattern noise structures can mimic weak, high velocity absorption lines. This pattern can vary from one observation to the next, depending upon the positions of the spectra on the microchannel plates. Whenever possible, we checked the data from multiple instrument channels (LiF1, LiF2) to determine the impact of fixed-pattern noise on the observed absorption features. The velocity integration component of the systematic error accounts for changes of  $\pm 15~{\rm km\,s^{-1}}$  in the values of  $v_{min}$  and  $v_{max}$ . The H<sub>2</sub> decontamination component accounts for modest uncertainties in the profile shapes and strengths of the model H<sub>2</sub> lines used to deblend the absorption ( $\Delta v_0 = 10~{\rm km\,s^{-1}}$ ,  $\Delta b = 10~{\rm km\,s^{-1}}$ , and  $\Delta [I/I_c] = 0.2$ ). Wakker et al. (2002) describe all of these sources of error and the methods used to calculate them.

We estimated  $3\sigma$  upper limits to the column densities for the 43 sight lines for which we find no evidence of high velocity O VI absorption in the following manner. We scaled the equivalent width error  $(\sigma_W)$  obtained for the Galactic thick disk/halo component of the absorption found by Wakker et al. (2002) to a value appropriate for an integration range of 100 km s<sup>-1</sup>. We then calculated the corresponding  $3\sigma$  column density limit assuming the linear curve-of-growth relation between  $W_{\lambda}$  and N:  $W_{\lambda} = (\pi e^2)(m_e c^2)^{-1}Nf\lambda^2$ . For O VI  $\lambda$ 1031.926, the  $3\sigma$  column density limit is  $N(\text{cm}^{-2}) < 2.4 \times 10^{12} \ \sigma_W(\text{mÅ})$ , where  $\sigma_W$  is the scaled equivalent width error. Table 2 contains the Galactic coordinates (l,b), data quality (Q), scaled equivalent width error  $(\sigma_W)$ , and column density limit for each of the 43 sight lines. Notes appended to the entries indicate whether the listed limits may be affected by other absorption features.

The values of N(O VI) listed in Table 1 should be free of saturation effects if the O VI is collisionally ionized. If the gas is photoionized, the temperature may be as low as  $\sim 10^4$  K. Consider the following conservative example. A single isolated Gaussian O VI  $\lambda 1031.926$  feature that arises in  $10^4$  K gas and has no additional broadening beyond its thermal width (b  $\approx 3.2 \text{ km s}^{-1}$ ) must have an intrinsic central optical depth  $\tau_{max}(v) \approx 1$  before a 0.10 dex saturation correction is required for a FUSE observation of the  $\lambda 1031.926$  line. When observed at the resolution of FUSE, this line has a maximum apparent optical depth  $\tau_{a,max}(v) \approx 0.21$  and a maximum apparent column density per unit velocity  $N_{a,max}(v) \approx 6 \times 10^{11}$  cm<sup>-2</sup> (km s<sup>-1</sup>)<sup>-1</sup>. For comparison, an isolated O VI  $\lambda 1031.926$  line with  $\tau_{max}(v) \approx 1$  and b  $\approx 15 \text{ km s}^{-1}$  observed by FUSE would have  $\tau_{a,max}(v) \approx 0.75$  and  $N_{a,max}(v) \approx 2 \times 10^{12} \text{ cm}^{-2} \text{ (km s}^{-1})^{-1}$ . Since all but a few of the observed O VI features have line widths well in excess of the instrumental width, cold narrow components can contribute only a fraction of the total observed columns, and therefore the effects of these components on the resulting  $N_a(v)$  profiles is diminished by broader components (i.e., their central optical depths would have to be much greater than unity to impact the total column density by 0.1 dex.)

 $<sup>^{11}</sup>$ Only two of the objects considered in this study (Ton S210, HE 0226-4110) were observed with special focal-plane image motions to reduce the fixed-pattern noise in the spectra.

Ideally, one would like to check explicitly whether unresolved saturated structure is present in the observed O VI absorption profiles by comparing the values of  $N_a(v)$  for both lines of the doublet. In practice, this is difficult to do for high velocity O VI since the high velocity portions of the 1037.617 Å line are often blended with other Galactic absorption features. The comparison at high velocities is possible in two cases (ESO 572-G34 and PG 1116+215), and no unresolved saturated structure is found. For sight lines where it is possible to examine the low velocity portions of the profiles, the  $\lambda 1031.926$  and  $\lambda 1037.617$  results are usually in good agreement, implying that saturation corrections for absorption in the thick disk/halo of the Galaxy are not required for most of the observations. Wakker et al. (2002) illustrate the  $N_a(v)$  profiles for the two O VI lines for all of the objects surveyed. In 17 of the 22 cases where a comparison of  $N_{a,\lambda 1037}/N_{a,\lambda 1032}$  can be made, the ratio is unity to within the  $1\sigma$  uncertainties. In the remaining 5 cases, the values of  $N_{a,\lambda 1037}/N_{a,\lambda 1032}$  range from  $\sim 1.1$  to 1.6, with 4 of the 5 cases having saturation corrections of less than 0.25 dex (see Savage et al. 2002b). Since the high velocity O VI absorption features are generally weaker than the thick disk/halo features, saturation corrections for the high velocity gas are small enough that they do not affect the scientific conclusions of this study.

We show examples of the O VI apparent column density profiles for the Mrk 509, ESO 572-G34, and PG 1116+215 sight lines in Figure 2. Toward Mrk 509, the thick disk/halo O VI  $\lambda$ 1031.926 absorption at low velocities is several times stronger than the high velocity absorption. The  $\lambda$ 1037.617 absorption is blended with other features at high velocities, so a direct comparison of the  $N_a(v)$  profiles at  $v_{LSR} < -100~{\rm km\,s^{-1}}$  is not possible. However, the good agreement in the  $N_a(v)$  profiles between  $-50~{\rm and}~+100~{\rm km\,s^{-1}}$  suggests that the weaker, high velocity absorption seen in the  $\lambda$ 1031.926 line should not be affected by unresolved saturated structure. Toward both ESO 572-G34 and PG 1116+215, the high velocity and thick disk/halo absorption features have comparable strengths and widths. The good agreement in the  $N_a(v)$  profiles at velocities between  $-50~{\rm and}~+250~{\rm km\,s^{-1}}$  shows that the data are unaffected by unresolved saturated structure. Thus, the  $N_a(v)$  profiles for these sight lines are also valid instrumentally-smeared representations of the true values of N(v). Since the high velocity O VI line widths and column densities are correlated (see §9.3), we conclude that saturation effects do not strongly influence the O VI column densities derived for the high velocity gas.

#### 3.3. Velocity Centroids and Line Widths

For each sight line where high velocity O VI is observed, we calculated the centroid velocity of the absorption by integrating the first moment of the apparent optical depth profiles,  $\bar{v} = \int v \, \tau_a(v) dv / \int \tau_a(v) dv$ , over the velocity range  $(v_{min} \text{ to } v_{max})$  used for the column density calculation. We calculated the velocity widths by integrating the second moments of the apparent optical depth profiles,  $b = \sqrt{2 \int (v - \bar{v})^2 \tau_a(v) dv} / \int \tau_a(v) dv$ , over the same velocity range. The factor of  $\sqrt{2}$  in this equation scales the derived width to an approximate Doppler spread parameter; for a single Gaussian component this relationship is exact:  $b = \sqrt{2}\sigma$ . Most of the high velocity

O VI features observed are weak  $[\tau_a(v) < 1]$ . Therefore, the derived value of the line width can be sensitive to the integration limits and to noise fluctuations near the ends of the integration range. It is best to examine the values of b for the sample in a statistical sense rather than regarding these as robust measures of the high velocity widths for individual sight lines. We list values of  $\bar{v}$  and b in Table 1.

#### 4. GENERAL GROUPS OF HIGH VELOCITY FEATURES

In the top panel of Figure 3, we identify the 102 sight lines in our sample. In this Hammer-Aitoff projection, the Galactic anti-center is at the center of the plot, and Galactic longitude increases from right to left. The name of each object listed in Table 1 appears next to each point. The absence of data points at low Galactic latitudes ( $-15^{\circ} \lesssim b \lesssim 15^{\circ}$ ) is the result of selecting objects sufficiently far away from the Galactic plane to avoid significant extinction of far-ultraviolet radiation.<sup>12</sup> Several other regions of the figure are also sparsely populated, including the Galactic center region for  $0^{\circ} \lesssim b \lesssim 70^{\circ}$  and the anti-center region for  $-60^{\circ} \lesssim b \lesssim 0^{\circ}$ .

Along 59 of the 102 sight lines we detect high velocity O VI  $\lambda 1031.926$  absorption with integrated (total) values of  $W_{\lambda}/\sigma_W \geq 3.0$ . Whenever possible, we have identified the high velocity O VI absorption features listed in Table 1 with corresponding high velocity features observed in H I 21 cm emission. H I data of varying quality exist for all of the sight lines considered here. The available single-dish radio data are shown by Wakker et al. (2002). The sources of H I data include the Leiden-Dwingeloo survey (Hartmann & Burton 1997), NRAO 140-foot telescope observations (Murphy et al. 1996), the Villa Elisa survey (Arnal et al. 2000; Morras et al. 2000), and Effelsberg 100 m telescope observations (see Wakker et al. 2001).

For some sight lines, the correspondence in the velocities and celestial coordinates of the O VI and H I allow for a straight-forward association to be made, but for many features the association with H I emission is much less certain. Even in cases where there is obvious H I emission at the velocities of the O VI absorption, one must keep in mind that the exact relationship between the H I and O VI can be complicated by ionization differences (neutral versus ionized) and beam size effects (typically 9'-36' for the H I emission versus a micro-arcsecond beam size for the O VI absorption). With these caveats in mind, we split the sample of high velocity O VI features into several categories, which are listed in Table 3. We summarize the number of features in each category, the Galactic coordinates spanned by the O VI features observed in each category (not necessarily the full range spanned by the H I), and the mean O VI column densities ( $\langle \log N \rangle \pm \sigma_{\langle \log N \rangle}$ ), central velocities ( $\langle \bar{v} \rangle$ ), and velocity widths ( $\langle b \rangle$ ). Several of these classifications contain high velocity O VI features with relatively unambiguous H I counterparts (Complex A, Complex C, the Outer Arm, and the

 $<sup>^{12}</sup>A$  reddening of E(B–V) = 0.10 magnitudes corresponds to a flux reduction factor of 4 at 1032 Å (i.e.,  $A_{\lambda}$  = 1.5 mag) for the standard Galactic interstellar extinction curve with a total to selective extinction ratio  $R_{\rm V}=3.1$  (Cardelli, Clayton, & Mathis 1989).

Magellanic Stream). Other classifications contain high velocity O VI features that do not have obvious H I counterparts, and these are labeled as either Local Group clouds or as "Other". We discuss the above categories of features and selection criteria in more detail in §§6 and 8.

We show the locations and various categories of O VI features on the sky in the bottom panel of Figure 3. Each category is represented by a different symbol. We include the 43 null detections listed in Table 2 to indicate directions that have been searched for O VI but do not have any detectable high velocity gas at a level consistent with the data quality of the observations. Most of these null detections (34/43) occur in the northern Galactic sky, and several occur within a few degrees of sight lines where high velocity O VI is present.

# 5. RESULTS FOR THE SAMPLE OF HIGH VELOCITY O VI ABSORPTION FEATURES

Eighty-five high velocity O VI absorption features are present along 59 of the 102 complete halo sight lines having sufficient FUSE data quality to detect high velocity O VI  $\lambda 1031.926$  absorption at a significance of  $\gtrsim 3\sigma$ . Most of these detections are for absorption features with equivalent widths  $\geq 30 \,\mathrm{mÅ}$ . Six detections have  $W_{\lambda} < 30 \,\mathrm{mÅ}$ . We include a weak feature toward PG 1259+593 with  $W_{\lambda} \approx 14 \,\mathrm{mÅ}$  even though the formal detection confidence is only  $\sim 2.3\sigma$  since the data quality is excellent and the feature is likely real. In this section, we provide information about the column densities, sky covering factors, and velocities of the O VI absorption.

## 5.1. Column Densities

We plot a histogram of the logarithmic column densities of the high velocity O VI features in Figure 4, where we have binned the data into 0.10 dex intervals. The minimum and maximum (logarithmic) column densities are 13.06 and 14.59, respectively, with an average value of  $\langle \log N \rangle = 13.95 \pm 0.34$  and a median of 13.97. (The value of  $\log \langle N \rangle = 14.06 \pm_{0.71}^{0.22}$  is similar.) The average high velocity O VI column density is a factor of  $\sim 2.7$  times (0.42 dex) lower than the value of  $\langle \log N \rangle = 14.38 \pm 0.18$  reported for the Galactic thick disk/halo O VI by Savage et al. (2002b). The thick disk/halo distribution of column densities, which is indicated in Figure 4 with a dashed line, is reasonably well represented as a Gaussian distribution. However, the observed velocity distribution for the high velocity O VI is skewed and considerably broader because it is possible to trace lower column density features at velocities where blending with other O VI absorption is minimal. Low column density features exist in the thick disk/halo distribution as well (see Jenkins 1978a), but they are presumably blended with stronger O VI features at similar velocities. The lowest O VI column density observed for the Milky Way thick disk/halo ( $\log N = 13.88$  toward Mrk 1095, not counting upper limits; Savage et al. 2002b) is comparable to the mean of the high velocity sample.

There are 17 sight lines for which the high velocity gas dominates the total O VI absorption;

these include ESO 265-G23, HE 1115-1735, MRC 2251-178, Mrk 304, Mrk 335, Mrk 926, Mrk 1502, NGC 588, NGC 595, NGC 1705, NGC 7469, NGC 7714, PG 0052+251, PG 1626+554, PG 2349-014, PHL 1811, and UGC 12163. In these directions the total O VI column densities of the high velocity gas are  $\sim 0.31 \pm 0.18$  dex higher than those of the Galactic thick disk/halo.

We plot the total high velocity O VI column density as a function of thick disk/halo O VI column density in the top panel of Figure 5. This plot shows roughly an order of magnitude scatter in the high velocity gas columns at all values of  $N(\text{O VI})_{\text{MW}}$  encountered along these sight lines. Within this scatter there is an apparent anti-correlation of  $N(\text{O VI})_{\text{HV}}$  and  $N(\text{O VI})_{\text{MW}}$ . For the 53/59 sight lines where good measures of both quantities are possible (excluding upper limits), we find a linear correlation coefficient of -0.26 and a slope  $\Delta \log N_{\text{HV}}/\Delta \log N_{\text{MW}} \approx -0.40$  (indicated by the dashed line). The Spearman rank correlation probability that the two populations are uncorrelated is only 5%, which indicates that the two populations are anti-correlated at about the  $2\sigma$  level. If the six upper limits on  $\log N_{\text{MW}}$  are included in the analysis as measured values, the significance of the all-sky anti-correlation increases to  $2.8\sigma$ , with an even higher significance if the actual values are less than the measured limits. (If the actual values are a factor of two less than the limits, then the significance of the anti-correlation climbs to  $3\sigma$ .)

A weak anti-correlation between  $\log N_{\rm MW}$  and  $\log N_{\rm HV}$  may be expected if some of the high velocity gas is lower velocity disk/halo gas that has been displaced to high velocities by energetic processes occurring within the Galaxy (e.g., supernovae). We estimate the approximate fraction of gas that would need to be displaced to cause the observed anti-correlation by considering a subset of the data points shown in the figure. If the high velocity data points with  $\log N({\rm O~VI})_{\rm HV} < 14$  are removed from this plot, the correlation disappears. For these 22 data points,  $\langle N({\rm O~VI})_{\rm HV}/N({\rm O~VI})_{\rm MW+HV} \rangle = 0.40 \pm 0.21$ . Thus, an average displacement of  $\lesssim 40\%$  of the total O VI along these sight lines would be sufficient to produce the observed trend. Sixteen of the 22 sight lines occur in the northern sky, where the thick disk/halo O VI distribution is enhanced relative to the southern sky.

Selection effects likely influence the trend seen in the top panel of Figure 5. The enhancement of thick disk/halo O VI in the northern sky (Savage et al. 2002b) together with the low values of  $N(\text{O VI})_{\text{MW}}$  along southern sight lines containing large columns of high velocity O VI at longitudes  $30^{\circ} < l < 130^{\circ}$  (MS, MSe, LG categories - see Table 3) results in the general trend seen. The anti-correlation is weakened if data points in the northern and southern Galactic sky are considered separately. In the north, the data points have a distribution that shows an anti-correlation at  $< 1\sigma$  confidence. In the south, the anti-correlation has a significance of  $\sim 1.5\sigma$  if limits are included, and  $\sim 1.0\sigma$  if the limits are omitted. Thus, we conclude that much of the observed anti-correlation may simply be due to differences in the Milky Way and HVC distributions in the two hemispheres.

In the bottom panel of Figure 5 we plot the integrated high velocity O VI column density against the integrated 0.25 keV X-ray intensity along the 59 sight lines where high velocity O VI is detected. The soft X-ray data points are from the ROSAT all-sky survey (Snowden et al. 1997) and

are R1+R2 band averages of the eight 12′ pixels ( $\sim 1150~\rm arcmin^2$  total) surrounding each sight line, ignoring the pixel directly along the sight line to avoid the X-ray emission from the background AGN or QSO being observed. The anti-correlation of  $N({\rm O~VI})_{\rm HV}$  with  $I({\rm X})$  is slightly stronger here than in the top panel of Figure 5. The trend largely disappears if sight lines with  $\log N({\rm O~VI})_{\rm HV} < 14$  are omitted from consideration. Interestingly, a similar comparison of  $I({\rm X})$  with  $N({\rm O~VI})_{\rm MW}$  by Savage et al. (2002b) reveals no correlation between  $N({\rm O~VI})_{\rm MW}$  and  $I({\rm X})$ , which if taken at face value seems to indicate that the X-ray and high velocity O VI are coupled more strongly. This too may be the result of selection effects. The interpretation of this plot is complicated by various problems encountered when comparing infinitesimal point source absorption-line observations with low resolution (both spatial and spectral) X-ray emission observations. Besides sampling different paths through the ISM, additional factors such as strong spectral attenuation in the X-ray band by intervening hydrogen, small scale structure in the ISM, and strong X-ray signals from foreground ISM gas make it difficult to quantify the X-ray emission associated explicitly with the high velocity gas. Future high-resolution X-ray observations will be needed to determine if this trend holds up under more careful scrutiny.

## 5.2. Sky Distribution – Column Densities

The absorption-line measurements for the individual sight lines in our study sample gas along very small solid angles. However, it is possible to construct a rough picture of the O VI distribution on the sky when the sight lines are considered together. Figure 6 contains all-sky plots of the distribution of high velocity O VI column densities. In the top panel, the column densities are coded for each sight line according to symbol size, with filled circles representing detections and downward-pointing triangles indicating upper limits. In cases where multiple features are present along a sight line, the filled circle is split, and the values for the individual features are coded accordingly. In the bottom panel of Figure 6, we plot a small filled circle, to indicate the precise location of each sight line, surrounded by a color-coded region (12° in radius) indicating the high velocity O VI column densities of the features listed in Table 1. In some directions, the region consists of several colors since multiple high velocity features are present. For sight lines where no high velocity gas is detected (see Table 2), we color-code the column densities of the upper limits with small (2.5° radius) circles. Each sight line can be identified by cross-referencing its position with the object names in Figure 3. Large O VI column densities for the high velocity gas occur in the southern Galactic hemisphere in directions associated with either the Magellanic Stream (e.g., Fairall 9, NGC 1705) or possible extragalactic clouds (e.g., Mrk 304, Mrk 926). In a few cases (e.g., ESO 265-G23, ESO 572-G34), large column densities also occur in the northern Galactic sky.

A comparable map of the sky distribution of Galactic thick disk/halo O VI column densities is shown and discussed by Savage et al. (2002b). The O VI catalog paper contains maps of the high velocity O VI column densities in narrow velocity channels. These maps allow one to examine the column densities as a function of velocity and position as well as the relationship of the high

velocity O VI to lower velocity O VI.

## 5.3. Sky Covering Factor

To make a meaningful estimate of the sky covering factor of the high velocity gas, it is important to note that the data quality varies from sight line to sight line. If we consider only the highest quality (Q=4) sight lines in the O VI sample, we find that 22 of 26 sight lines have total high velocity O VI equivalent widths  $\Sigma W_{1032} \geq 30 \,\text{mÅ}$  at a detection confidence  $[W_{1032}/\sigma_W]_{tot} \geq 3.0$ . The remaining four Q=4 sight lines (NGC 1068, PG 0804+761,VII Zw 118, and vZ 1128) have equivalent width errors that would allow high confidence detections of 30 mÅ features if they were present (see Table 2). The Q=4 sight lines are scattered across the sky and are not unique to one particular region. At lower data qualities (Q=1-3), the percentage of sight lines with  $\Sigma W_{1032} \geq 30 \,\text{mÅ}$  detected at high confidence drops to about 50%, with few of the non-detection sight lines having sufficient data quality to rule out weak absorptions. Fifty-nine of the 102 sight lines in the sample have total high velocity O VI equivalent widths  $\Sigma W_{1032} > 30 \,\text{mÅ}$  at a detection confidence  $[W_{1032}/\sigma_W]_{tot} \geq 3.0$ . Thus, a key result of our survey is that a large fraction (at least 58% and perhaps as many as 85%) of the sight lines contain high velocity O VI with  $\Sigma W_{1032} > 30 \,\text{mÅ}$ .

At higher equivalent width thresholds,  $\Sigma W_{1032} \gtrsim 100\,\mathrm{mÅ}$ , the effect of data quality on the resulting detection rate is diminished considerably. We find that  $\sim 42\%$  of the Q=4 sight lines have  $\Sigma W_{1032} \gtrsim 100\,\mathrm{mÅ}$  at  $3\sigma$  confidence, compared to  $\sim 38\%$  for the Q=1-3 sight lines. There is no significant difference in the detection rate within the individual data quality intervals at this threshold. We list the numbers and percentages of sight lines containing high velocity O VI for various equivalent width thresholds and data qualities in Table 4. Values for equivalent width thresholds of less than  $100\,\mathrm{mÅ}$  for Q=1-3 sight lines are likely incomplete and should probably be treated as lower limits. These numbers are useful for comparisons with detection rates for other O VI absorption systems, such as the weak IGM O VI absorbers (see Savage et al. 2002a) or the Galactic thick disk/halo. Positive detections of O VI associated with the thick disk/halo occur for 91 of the 102 sight lines in our sample, and the eleven non-detections occur for sight lines where the data quality is marginal (Savage et al. 2002b).

We provide a more detailed estimate of the sky covering fraction of high velocity O VI in Table 5, where we list the numbers and percentages of sight lines in our sample having total high velocity O VI column densities,  $\Sigma N({\rm O~VI})_{\rm HV}$ , greater than a column density threshold,  $N_0$ . We list values for the entire sample as well as for several slices in Galactic longitude and latitude  $(0^{\circ} < l < 180^{\circ}, 180^{\circ} < l < 360^{\circ}; b < 0^{\circ}, b > 0^{\circ})$ . Note that values of the covering fraction for  $N_0 \lesssim 10^{14}~{\rm cm}^{-2}$  are subject to data quality biases of the type discussed above and may underestimate the true covering fractions. For the entire sample, we find that  $\sim 60\%$  of the sight lines surveyed (and likely more if the data quality could be improved) contain high velocity O VI with  $N \geq 10^{13}~{\rm cm}^{-2}$ , and  $\sim 30\%$  have  $N \geq 10^{14}~{\rm cm}^{-2}$ . These two O VI column density thresholds correspond roughly to  $N({\rm H}^+) \gtrsim 10^{16} Z^{-1}$  and  $\gtrsim 10^{17} Z^{-1}$ , respectively, where Z is the metallicity

of the hot gas (on a linear scale where Z=1 is solar), and the ionized hydrogen column density of the hot gas is  $N(\mathrm{H}^+)=N(\mathrm{O~VI})~(\mathrm{O/H})_{\odot}^{-1}~\mathrm{f}_{OVI}^{-1}~Z^{-1}$ . In making these estimates of  $\mathrm{H}^+$  in the O VI-bearing gas, we adopt a reference abundance  $(\mathrm{O/H})_{\odot}=5.45\times10^{-4}$  (Holweger 2001) and an O VI ionization fraction  $\mathrm{f_{O\,VI}}\equiv(\mathrm{O~VI/O})\lesssim~0.2$ , which is the maximum value expected under conditions of either collisional ionization or photoionization (see §9 and Tripp & Savage 2000).

Assuming that the high velocity O VI covering factors listed in Table 5 provide a fair representation of the entire sky, we find that roughly 30–35% of the sky is covered by the hot, high velocity  $H^+$  at a level of  $\gtrsim 4 \times 10^{17}$  cm<sup>-2</sup> if the gas has a typical metallicity comparable to that of the Magellanic Stream,  $Z_{MS} \sim 0.2-0.3$  (Lu et al. 1998; Gibson et al. 2000; Sembach et al. 2001a). (At this column density, data quality issues do not seriously affect this estimate). This  $N(H^+)$  estimate would increase by a factor of  $\sim 2$  if the metallicity is closer to the value of  $Z \sim 0.1$  found for Complex C in the directions of Mrk 290 (Wakker et al. 1999) and PG 1259+593 (Richter et al. 2001). The covering factor of the hot, high velocity  $H^+$  inferred from the high velocity O VI measurements is similar to the high velocity H I covering factor at a comparable column density level. In a sensitive survey of H I 21 cm emission in 860 directions, Lockman et al. (2002) find that  $\sim 37\%$  of the sky is covered by high velocity H I at a  $4\sigma$  detection threshold of  $\sim 8 \times 10^{17}$  cm<sup>-2</sup>.

We note that the detection rate of high velocity gas in the southern Galactic hemisphere appears to be slightly higher than for northern latitudes. For the full sample, we find high velocity detection rates of 75% (27/36) and 36% (13/36) for  $N_0 = 10^{13}$  and  $10^{14}$  cm<sup>-2</sup> and  $b < 0^{\circ}$ , compared to 48% (32/66) and 27% (18/66) for  $b > 0^{\circ}$ . The values for the two hemispheres differ by about  $1.5\sigma$  if the sight lines are drawn from a random population. Small number statistics, data quality, and selection effects can play important roles in such comparisons. For example, a relatively large percentage of the northern sight lines (9/66) lie in the general direction of Complex C, where high velocity O VI is prevalent (see §6.1). Therefore, it is desirable to diversify and increase both the sample size and data quality (preferably by factors of 2 or more) to test whether the trend we note in the current sample is a general feature of the high velocity sky or a subtle selection effect.

#### 5.4. Velocity Centroids

The top panel of Figure 7 contains a histogram of the high velocity O VI feature centroids in the LSR reference frame. These centroids are the profile-weighted velocities (first moments) derived by integrating the apparent optical depth profiles over the velocity ranges listed in Table 1. The most extreme velocity centroids are found for the sight lines toward NGC 588 ( $v_{LSR} \approx -372~{\rm km\,s^{-1}}$ ), NGC 4670 ( $v_{LSR} \approx +363~{\rm km\,s^{-1}}$ ), and Mrk 478 ( $v_{LSR} \approx +385~{\rm km\,s^{-1}}$ ). The average negative velocity centroid is  $-202\pm77~{\rm km\,s^{-1}}$ , and the average positive velocity centroid is  $187\pm70~{\rm km\,s^{-1}}$ . The distribution of velocities is relatively symmetric about  $v_{LSR} = 0~{\rm km\,s^{-1}}$ . The histogram is sampled in 20 km s<sup>-1</sup> velocity bins. The dashed line in the figure shows a Gaussian fit to the observed centroids. The Gaussian has a width  $\sigma_{\langle \bar{v} \rangle} \approx 207~{\rm km\,s^{-1}}$  (b  $\approx 293~{\rm km\,s^{-1}}$ ; FWHM  $\approx 488~{\rm km\,s^{-1}}$ ) and is centered at  $\sim -33~{\rm km\,s^{-1}}$ . Both  $\langle \bar{v} \rangle$  and  $\sigma_{\langle \bar{v} \rangle}$  are uncertain because of the absence

of points at  $|v_{LSR}| \lesssim 100 \text{ km s}^{-1}$ .

For comparison with the distribution of high velocity centroids in the LSR reference frame, we also show the distributions in the Galactic Standard of Rest (GSR) and the Local Group Standard of Rest (LGSR) in the middle and bottom panels of Figure 7. Velocities in these reference frames are related to the LSR velocity through the equations  $v_{GSR} = v_{LSR} + 220 \, (\,\mathrm{km}\,\mathrm{s}^{-1}) \, \sin(l) \cos(b)$  and  $v_{LGSR} = v_{GSR} - 62 \, (\,\mathrm{km}\,\mathrm{s}^{-1}) \, \cos(l) \cos(b) + 40 \, (\,\mathrm{km}\,\mathrm{s}^{-1}) \, \sin(l) \cos(b) - 35 \, (\,\mathrm{km}\,\mathrm{s}^{-1}) \, \sin(b)$  (Karachentsev & Makarov 1996). In both cases the dispersion in the high velocity gas centroids is smaller than in the LSR reference frame ( $\sigma_{\langle \bar{v} \rangle} \approx 144 \, \mathrm{km}\,\mathrm{s}^{-1}$  in the GSR, and  $\sigma_{\langle \bar{v} \rangle} \approx 128 \, \mathrm{km}\,\mathrm{s}^{-1}$  in the LGSR).

In Table 6 we list the means and standard deviations of the high velocity feature centroids for the four Galactic regions with either  $b < 0^{\circ}$  or  $b > 0^{\circ}$ , and  $l < 180^{\circ}$  or  $l > 180^{\circ}$ . Values of  $\langle \bar{v} \rangle \pm \sigma_{\langle \bar{v} \rangle}$  are given for the LSR, GSR, and LGSR reference frames. The numbers of high velocity features in each Galactic region are listed at the bottom of the table. In most quadrants and in the total sample the mean centroid velocity is smaller in the GSR than in the LSR. In all but one quadrant ( $l > 180^{\circ}, b > 0^{\circ}$ ) the dispersions in the centroids are also smaller in the GSR than in the LSR, suggesting that this is a better reference frame for describing the velocities. In other words, the high velocity O VI in our sample has an observed distribution of bulk velocities that is more evenly and tightly clustered about the velocity of the Galactic center than about the velocity expected for gas participating in differential Galactic rotation at the Galactocentric radius of the Sun (with the important caveat that the HVC features were selected in a manner to avoid LSR velocities  $|v_{LSR}| \lesssim 100 \text{ km s}^{-1}$ ). A similar result, which applies to the velocity distribution of neutral hydrogen clouds and is subject to many of the same kinds of selection effects, has been used to support arguments for an extragalactic location for some of the H I HVCs (e.g., Blitz et al. 1999).

Features designated EPn dominate the high velocity O VI absorption in the discrepant quadrant for which the standard deviation of the values of  $\bar{v}$  is larger in the GSR than in the LSR ( $l > 180^{\circ}, b > 0^{\circ}$ ). This group of clouds is not better represented in the GSR reference frame and is distinct from the other categories in this regard. As noted in the previous section, some of these features may trace thick disk/halo gas accelerated to high velocities.

We illustrate the velocities of the O VI features in the LSR reference frame in Figure 8, where we show the dependence of the velocity on both Galactic longitude (top panel) and Galactic latitude (bottom panel). The vertical bars on each point indicate the velocity widths (b-values) of the observed features, not the errors in  $\bar{v}$ . At  $l > 180^{\circ}$ , all but one feature have positive LSR velocities; the exception is the LG feature toward Ton S210, which is located near the south Galactic pole. At  $l < 180^{\circ}$ ,  $\bar{v} > 0$  km s<sup>-1</sup> for only 8 features, while  $\bar{v} < 0$  km s<sup>-1</sup> for 43 features. This strong segregation of velocities in Galactic longitude is also apparent in the latitude plot in the bottom panel of Figure 8.

We provide a similar plot for the longitude dependence in the GSR reference frame in Figure 9.

Despite showing a somewhat tighter clustering of data points about  $v_{GSR} = 0 \text{ km s}^{-1}$ , there is still considerable scatter in the velocity centroids as a function of longitude  $(\sigma_{\langle \bar{v} \rangle} \sim 144 \text{ km s}^{-1} \text{ for the whole sample})$ . The dashed lines in the figure bound the range of velocities expected for Galactic disk sight lines with  $|b| < 20^{\circ}$  and  $|v_{LSR}| \lesssim 100 \text{ km s}^{-1}$ . As expected, few points fall in this zone because of sample selection effects. In the GSR reference frame, the general velocity distribution of data points clusters more tightly about zero velocity than in the LSR reference frame. The few sight lines that fall in the range of velocities expected for the thick disk/halo include Ton S210 ( $l \approx 225^{\circ}$ ) and several sight lines in the general direction of Complex C ( $l \sim 80 - 110^{\circ}$ ; Mrk 817, Mrk,876, PG 1351+640, PG 1415+451, and PG 1626+554). Both Complex C and the compact HVC toward Ton S210 are likely extragalactic clouds that will be discussed further in §6.

#### 5.5. Sky Distribution – Velocities

In Figure 10 we plot the distribution of O VI centroid velocities projected onto the sky for both the LSR and GSR reference frames. The projection is the same as that in Figure 6, with the Galactic anti-center at the center of the plots. In each direction we plot a small filled circle to indicate the precise location of the sight line, with a corresponding a color-coded region indicating velocity if high velocity O VI absorption is detected. In some directions, the region contains several colors since multiple high velocity features are present within the 12° radius of the region. Each sight line can be identified by cross-referencing its position with the object names in Figure 3. The color coding of the velocities (blue/green = negative velocities, orange/red = positive velocities) is the same in both panels. A comparison of the two panels shows that the color shading in the GSR panel is generally lighter, indicating that the velocities are smaller in this reference frame, as discussed above.

We show a similar plot for the H I high velocity sky observed in 21 cm emission in Figure 11a, where we have coded the velocities in the same color system, but at the finer spatial resolution afforded by the H I data. Figures 11b and 11c display the same data in azimuthal equal-area projections looking up toward the north Galactic pole and down toward the south Galactic pole. Several large structures or groups of H I high velocity clouds are visible in Figure 11, including: 1) the Magellanic Stream, which passes through the south Galactic pole and extends up to  $b \sim -30^{\circ}$ , with positive velocities for  $l \gtrsim 180^{\circ}$  and negative velocities for  $l \lesssim 180^{\circ}$ ; 2) high velocity cloud Complex C, which covers a large portion of the northern Galactic sky between  $l = 30^{\circ}$  and  $l = 150^{\circ}$  and has velocities of roughly -100 to -170 km s<sup>-1</sup>; 3) the extreme positive velocity clouds in the northern sky (EPn), which are located in the general region  $180^{\circ} \lesssim l \lesssim 330^{\circ}$ ,  $b \approx 30^{\circ}$ ; and 4) the Galactic center negative velocity (GCN) clouds located near  $l \sim 45^{\circ}$ ,  $-60^{\circ} \lesssim b \lesssim -30^{\circ}$ .

In Figures 11a-c, we have indicated the positions and velocities of the high velocity O VI features with filled circles having the same color coding scale as the H I data. If multiple high velocity features are present, the circle is subdivided into multiple colored regions. Small open circles (or "X" marks for the two stellar sight lines) denote the directions where no high velocity

- O VI is detected (see Table 2). Several key points about these figures are worth highlighting:
- 1) There is excellent velocity correspondence between the H I and O VI in Complex C, with sight lines passing near to Complex C, but not through the high velocity H I, showing no O VI absorption (see §6.1).
- 2) Toward Complex A, there is a close pair of sight lines exhibiting an O VI detection (Mrk 106) and a non-detection (Mrk 116) (see §6.2).
- 3) The high velocity component toward NGC 3310 ( $l = 156.6^{\circ}, b = +54.1^{\circ}$ ) has a velocity similar to that of Complexes A and C, even though there is no H I 21 cm emission detected along the sight line at these velocities.
- 4) The H 1821+643 sight line contains O VI absorption at the velocities of the Outer Arm as well as at more negative velocities (see §6.4). The progression of velocities between the Outer Arm and Complex C is relatively smooth.
- 5) In the  $l < 180^{\circ}$ , b < 0 quadrant of the sky there are often two negative velocity components, with the highest negative velocity components occurring in the Magellanic Stream (MS) or the extension of the Magellanic Stream (MSe) at velocities typical of the Stream (see §6.3). Components with  $\bar{v} \sim -120~{\rm km\,s^{-1}}$  concentrate to longitudes less than those of the Stream, whereas components at  $l \sim 120^{\circ} 140^{\circ}$  have velocities typical of the Stream.
- 6) There is good velocity correspondence between the H I and O VI velocities in the positive velocity portion of the Magellanic Stream at  $l > 180^{\circ}$  (see §6.3). The O VI features off the main axis of the Stream at these longitudes have velocities similar to those of the H I near the Stream.
- 7) In the  $l > 180^{\circ}$ , b > 0 quadrant of the sky there are positive velocity O VI and H I features, sometimes at similar velocities. These are some of the EPn features listed in Tables 1 and 3. In some cases, the O VI features have substantially higher velocities than the H I. The  $-277 \, \mathrm{km \, s^{-1}}$  feature toward ESO 265-G23 ( $l = 285.9^{\circ}$ ,  $b = +16.6^{\circ}$ ) has a velocity and location close to that of H I in the leading arm of the Magellanic Stream identified by Putman et al. (1998); H I at similar velocities is seen  $\sim 1^{\circ}$  away.
- 8) At  $l \sim 180^{\circ}$ ,  $b > 0^{\circ}$  there is high velocity O VI with  $\bar{v} \sim +150 \text{ km s}^{-1}$ . Some of these features are broad absorption wings extending from the lower velocity absorption produced by the Galactic thick disk/halo (see §8.1).
- 9) There may be high velocity H I near the  $+143~{\rm km\,s^{-1}}$  O VI feature toward PKS 0405-12 ( $l=204.9^{\circ}, b=-41.8^{\circ}$ .
- 10) High velocity O VI features toward Mrk 478 ( $l=59.2^{\circ},b=+65.0^{\circ},\ \bar{v}\approx+385\ \mathrm{km\,s^{-1}}$ ), NGC 4670 ( $l=212.7^{\circ},b=+88.6^{\circ},\ \bar{v}\approx+363\ \mathrm{km\,s^{-1}}$ ), and Ton S180 ( $l=139.0^{\circ},b=-85.1^{\circ},\ \bar{v}\approx+251\ \mathrm{km\,s^{-1}}$ ) stand out as having particularly unusual velocities compared to those of other O VI features in similar regions of the sky. These features are classified as 0th in Table 1, and may be located outside the Local Group (i.e., in the IGM).
- 11) Sight lines that contain both negative and positive high velocity features include Mrk 509,

Ton S180, and several Complex C sight lines (Mrk 817, Mrk 876, PG 1259+593, PG 1351+640, and PG 1626+554).

Although not shown in Figures 10 and 11, O VI and H I are also present at intermediate velocities ( $|v_{LSR}| \sim 30-80~{\rm km\,s^{-1}}$ ) along many of the sight lines considered in this work. The intermediate velocity O VI absorption and its relationship to the intermediate velocity H I sky are discussed briefly by Savage et al. (2002b). The kinematics, elemental abundances, molecular content, and locations of the intermediate velocity clouds (IVCs) indicate that they are part of the Galactic processes that circulate and distribute interstellar material in the thick disk and halo of the Galaxy (Houck & Bregman 1990; Richter et al. 2001, 2002). The IVC population appears in most cases to be distinct from higher velocity phenomena traced in H I (see Wakker 2001), and it is likely that the O VI IVC population is not strongly connected with the high velocity phenomena we observe in O VI absorption. There is no general correlation in the amount of intermediate and high velocity H I or O VI observed along the sight lines in our sample.

Table 7 contains a general breakdown of the number of sight lines containing negative and positive high velocity O VI features. For several cuts in Galactic longitude and latitude we list the number of sight lines containing at least one high velocity O VI component with a velocity centroid,  $\bar{v}$ , exceeding a threshold velocity,  $v_0$ . The table quantifies the graphical results shown in Figures 8 and 10, namely that the  $l < 180^{\circ}$  region of the sky contains predominantly negative velocities, while the  $l > 180^{\circ}$  region of the sky contains predominantly positive velocities. Combined, roughly 58% (59/102) of the sight lines have O VI features with  $|\bar{v}| > 90 \text{ km s}^{-1}$ , and 28% (29/102) have O VI features with  $|\bar{v}| > 200$ . A small percentage of sight lines, 11% (11/102), has  $|\bar{v}| > 300$ , and of these all but 3 (Mrk 478, NGC 1705, and NGC 4670) are located in the southern Galactic hemisphere at  $45^{\circ} < l < 135^{\circ}$ . Data quality affects these percentages since weak features ( $W_{1032} \lesssim 100 \text{ mÅ}$ ) are below the detection limit for some sight lines. Thus, the percentages enclosed within parentheses in Table 7 are best treated as lower limits. For comparison, we also tabulate the all-sky percentages for the highest quality (Q = 4) sight lines within square brackets in Table 7. As expected, the Q = 4 sight line percentages are higher than those for the entire sample.

#### 5.6. Line Widths

The observed line widths of the high velocity O VI features range from b  $\sim 16$  to  $\sim 81~\rm km\,s^{-1}$ . We show the distributions of b-values for the high velocity gas and thick disk/halo absorption in Figure 12. These b-values have not been corrected for a small amount of instrumental broadening (b<sub>inst</sub>  $\sim 12-15~\rm km\,s^{-1}$ ). The average high velocity feature width is  $\langle b \rangle = 40\pm14~\rm km\,s^{-1}$  if all of the high velocity features listed in Table 1 are considered. In some cases, the line widths are less reliable since they depend strongly on the exact choice of the velocity cutoff between thick disk/halo absorption and the high velocity absorption used in the calculation of b. Thus, one must be careful about interpreting the meaning of the line width for some sight lines, especially when the thick

disk/halo and high velocity portions of the absorption merge without recovery to the continuum at intermediate velocities. These less reliable values of b are enclosed in parentheses in Table 1. For the 19 features having reliable b-values,  $\langle b \rangle = 42 \pm 12 \, \text{km s}^{-1}$ , which is indistinguishable from the value for the entire sample.

The average high velocity line width is smaller than the value of  $\langle b \rangle = 60 \pm 15 \text{ km s}^{-1}$  found for the low velocity O VI (Savage et al. 2002b). This is due in part to the reduced blending of the high velocity gas as well as the multi-component nature of the low velocity gas, which by definition occurs between  $-100 \lesssim v_{LSR} \lesssim 100 \text{ km s}^{-1}$ . If the broadening is purely thermal in nature, the smallest Doppler widths in the high velocity sample (b  $\sim 16 \text{ km s}^{-1}$ ) correspond to temperatures of  $\sim 3 \times 10^5 \text{ K}$ , the temperature at which O VI peaks in abundance under conditions of collisional ionization equilibrium (Sutherland & Dopita 1993). These small widths are only slightly larger than the instrumental resolution, so it is possible that the temperatures may be lower in these few cases. The larger line widths are likely dominated by turbulent broadening, shear, or flows rather than thermal broadening at high temperatures since the fractional abundance of O VI decreases rapidly at  $T \gtrsim 10^6 \text{ K}$  (i.e.,  $b_{thermal} \gtrsim 34 \text{ km s}^{-1}$ ) (Shapiro & Moore 1976; Sutherland & Dopita 1993).

# 6. O VI ASSOCIATED WITH PREVIOUSLY IDENTIFIED HIGH VELOCITY CLOUDS

We detect high velocity O VI along every sight line in our sample for which there is a known high velocity H I cloud observed in 21 cm emission along the sight line. These H I HVCs include large complexes of gas, such as Complex C and the Magellanic Stream, as well as smaller isolated clouds. We discuss some of these high velocity features in this section.

## 6.1. Complex C

High velocity cloud Complex C is a large assembly of high velocity gas in the northern Galactic sky between  $l \sim 30^{\circ}$  and  $l \sim 150^{\circ}$ . It is well-known for its substantial H I content and distance (M > 1.2 × 10<sup>6</sup> M<sub>☉</sub>; d > 5 kpc, z > 3.5 kpc; van Woerden et al. 1999a; Wakker 2001), lack of molecular hydrogen (Murphy et al. 2000; Richter et al. 2001), and substantially sub-solar abundances. The metallicity of Complex C is  $Z \sim 0.1$  (Wakker et al. 1999; Richter et al. 2001), but may be as high as  $Z \sim 0.3$  in some locations (Gibson et al. 2001a). The gas in Complex C has LSR velocities ranging from approximately –100 to –170 km s<sup>-1</sup>, which is sufficient to separate the absorption from both the Milky Way thick disk/halo absorption in this direction (extending out to  $v_{LSR} \sim -100$  km s<sup>-1</sup>) and intermediate velocity absorption features along the path to Complex C, such as the Intermediate Velocity Arch ( $v_{LSR} \sim -55$  km s<sup>-1</sup>) (see Wakker 2001). Complex C contains ionized gas as revealed through previous observations of O VI absorption (Murphy et al.

2000; Sembach et al. 2000) and H $\alpha$  emission (Tufte, Reynolds, & Haffner 1998; Wakker et al. 1999).

Nine of the sight lines in our sample pass through Complex C and contain O VI absorption at velocities characteristic of the high velocity neutral gas. These are Mrk 279, Mrk 290, Mrk 501, Mrk 506, Mrk 817, Mrk 876, PG 1259+593, PG 1351+640, and PG 1626+554. We illustrate the H I 21 cm emission in the region of sky containing Complex in Figure 13 to show the general morphology of the neutral gas in these directions. Two velocity ranges,  $-200 < v_{LSR} < -150$  km s<sup>-1</sup> (top panel) and  $-150 < v_{LSR} < -100$  km s<sup>-1</sup> (bottom panel), are shown to illustrate the differences in the H I structure in these velocity ranges. These H I data are from the Leiden-Dwingeloo survey (Hartmann & Burton 1997). In the more negative velocity map, the two sight lines that lie in densest concentrations of H I are Mrk 876 and PG 1351+640. In the less negative velocity map, all of the sight lines lie in the direction of some H I emission, and additional intermediate and high velocity features (IV Arch, Complex A, Complex K) are identified.

The O VI detections toward Complex C are clearly visible in the all-sky maps shown in Figures 10 and 11. We plot the O VI  $\lambda 1031.926$  and C II  $\lambda 1036.337$  absorption profiles for each of the 9 Complex C sight lines in Figure 14. The O VI absorption traces highly ionized gas, while the C II absorption traces a combination of neutral and weakly ionized gases. Included for each sight line is the H I 21 cm emission profile from Murphy et al. (unpublished, see Wakker et al. 2002) for comparison with the absorption features. The single-dish NRAO 140-foot telescope 21 cm emission measurements have a beam size of 21' (FWHM), a channel spacing of  $\sim 1-2$  km s<sup>-1</sup>, and a  $3\sigma$  sensitivity of  $\sim (1-2) \times 10^{18}$  cm<sup>-2</sup> for a 50 km s<sup>-1</sup> integration range. The 21 cm emission provides information about the velocity structure of the primary neutral gas concentrations along the sight lines, while the C II profile reveals the total velocity extent of the neutral plus weakly ionized gas.

O VI absorption is present at the velocities of the H I 21 cm emission in Complex C. Thus, the highly ionized and neutral gases appear to be kinematically related in these different directions. Values of log  $N({\rm O~VI})$  range from 13.67 to 14.35, with an average of 13.93 and a standard deviation of 0.25 dex. The O VI centroids range from a low of  $\sim -110~{\rm km\,s^{-1}}$  (PG 1259+593) to a high of  $\sim -150~{\rm km\,s^{-1}}$  (Mrk 279, Mrk 876, PG 1626+554). We summarize the relative velocities and column densities of the H I and O VI in Table 8. The O VI and H I velocities track each other reasonably well, with a typical scatter of  $\sim 15~{\rm km\,s^{-1}}$ . There is no obvious dependence of the O VI column density on the H I column density. For example, two sight lines (Mrk 279 and PG 1351+540) with log  $N({\rm O~VI}) \approx 13.67$  have H I columns that differ by 0.46 dex, and two sight lines (Mrk 506 and Mrk 876) with log  $N({\rm O~VI}) \approx 14.06$  have H I columns that differ by 0.66 dex. However, there is a weak trend for the ratio of the two species to change with position across Complex C, with higher values of  $N({\rm H~I})/N({\rm O~VI})$  at higher longitudes.

The strong C II and O VI lines have similar negative velocity extents along each sight line. The C II traces very small amounts of H I, as well as H<sup>+</sup>, so it is difficult to know if the velocity extents of the neutral and highly ionized gas are identical, but this result is at least suggestive that

they are similar.

Several additional sight lines in the O VI survey pass near Complex C but do not have high velocity O VI detections. We comment briefly on a few of these sight lines below.

Mrk 205 ( $l=125.45^{\circ}, b=+41.67^{\circ}$ ) has marginal FUSE data ( $Q=1, S/N \sim 4$ ), resulting in a  $3\sigma$  upper limit of log  $N(O\ VI) < 13.79$  for the high velocity gas at Complex C velocities. High-resolution Space Telescope Imaging Spectrograph (STIS) data show that the sight line intercepts neutral gas at Complex C velocities (Tripp et al. 2002), but the FUSE data are insufficient for an analysis of the absorption.

The Mrk 487 sight line ( $l = 87.84^{\circ}, b = +49.03^{\circ}$ ) has a C II  $\lambda 1036.337$  absorption feature near  $-140~{\rm km\,s^{-1}}$ . There is no detectable H I 21 cm emission at this velocity along the sight line, but nearby Complex C sight lines (e.g., Mrk 290, PG 1626+554) show C II absorption at similar velocities. No high velocity O VI is present at a level of  $\log N < 14.03~(3\sigma)$ , even though the sight line passes only  $2.6^{\circ}$  from the Mrk 290 sight line, where high velocity O VI is detected with  $\log N \approx 14.20$ . This separation corresponds to a linear dimension of  $\sim 220~({\rm z}~/5~{\rm kpc})$  pc.

3C 249.1 ( $l=130.39^{\circ}, b=+38.55^{\circ}$ ) lies a bit further off Complex C than Mrk 205 but is still only a few degrees from the edge of moderately strong H I 21 cm emission between -150 and -100 km s<sup>-1</sup> (see Figure 13). No high velocity O VI is present at a level of  $\log N < 13.83$  ( $3\sigma$ ).

The NGC 3310 sight line ( $l=156.60^{\circ}, b=+54.06^{\circ}$ ) has a high velocity O VI component at velocities near those of Complex C, but no H I 21 cm emission is detected at this velocity or at lower velocities typical of Complex A. The O VI feature has a velocity of  $\sim -162~{\rm km\,s^{-1}}$  and is classified as 0th in Table 1.

PG 1444+407 ( $l=69.90^{\circ}, b=+62.72^{\circ}$ ), PG 1415+451 ( $l=84.72^{\circ}, b=+65.32^{\circ}$ ), and SBS 1415+437 ( $l=81.96^{\circ}, b=+66.20^{\circ}$ ) all lie to the north of Complex C, off of the main H I 21 cm emission. No high velocity O VI is detected at Complex C velocities.

#### 6.2. Complex A

Sight lines to two extragalactic objects in our sample (Mrk 106, Mrk 116) pass through high velocity cloud Complex A. Complex A is located at a distance of 4–10 kpc (z = 2.6–6.8 kpc), has a mass of  $\sim 2.0 \times 10^6$  M<sub> $\odot$ </sub>, and has H I velocities of  $-210 \lesssim v_{LSR} \lesssim -140$  km s<sup>-1</sup> (van Woerden et al. 1999b; Wakker 2001). We detect O VI absorption with log  $N \approx 13.81$  ( $W_{1032} \approx 65$  m Å)

between -150 and -100 km s<sup>-1</sup> toward Mrk 106. This absorption strength is comparable to that of the weaker detections toward Complex C (e.g., Mrk 279, Mrk 501, Mrk 817, PG 1351+640). The centroid of the absorption (-125 km s<sup>-1</sup>) is shifted by +32 km s<sup>-1</sup> from the centroid of the H I 21 cm Complex A feature in this direction. The O VI detection is weak, with  $W_{1032}/\sigma_W = 3.0$ . Thus, while it is plausible that the absorption could be due to Complex A, a higher quality FUSE spectrum of this object would be desirable to confirm both the strength and velocity of this feature.

We do not detect high velocity O VI toward Mrk 116, and set a  $3\sigma$  limit of  $\log N < 13.49$ . At the distance of Complex A, the 2° separation of Mrk 116 and Mrk 106 corresponds to a linear separation of 140–350 pc. One other object in our sample, PG 0832+675, lies in front of Complex A and does not exhibit any O VI or low ionization species at Complex A velocities (see also Ryans et al. 1997 for a non-detection of Ca II  $\lambda 3933.663$  absorption). The lack of C II absorption in the FUSE data sets the lower limit to the distance of Complex A.

#### 6.3. The Magellanic Stream

The Magellanic Stream is a complex of high velocity gas that has been tidally torn from the Magellanic Clouds as they interact with the Milky Way. The Stream is readily visible in the H I maps shown in Figure 11. It consists of gas at both positive and negative velocities, with a zero velocity crossing near the south Galactic pole. The H I 21 cm emission of the Stream covers nearly 1000 square degrees on the sky (see Putman 2000). Several sight lines in our sample either intersect the H I Stream (Fairall 9, NGC 7714, NGC 7469, PG 2349-014) or lie very near to it on the sky and have velocities similar to the Stream velocities (NGC 1705, PKS 0558-304). We classify these as MS sight lines in Table 3. An additional 12 objects lie in the general vicinity of the Magellanic Stream; we label these as possible extensions of the Magellanic Stream (MSe). The association of the MSe O VI features with the H I gas of the Magellanic Stream is less certain than for the MS sight lines since there is no detectable 21 cm emission at Stream velocities along these sight lines. Since the MSe and LG features in this region of the sky have similar velocities, it is possible that some of the MSe features may eventually be more properly identified as Local Group clouds.

We show the H I 21 cm emission profiles and O VI and C II absorption profiles for six MS/MSe sight lines in Figure 15. In the four cases where both high velocity H I and O VI are detected, the O VI absorption is broader than the H I. For the three MS sight lines with negative Stream velocities, the high velocity O VI absorption overlaps (or nearly overlaps in the case of NGC 7714) the velocities of the H I and extends to considerably less negative velocities. We tentatively classify the O VI feature toward NGC 7714 ( $\bar{v} = -259 \text{ km s}^{-1}$ ), as well as the higher velocity features toward NGC 7469 ( $\bar{v} = -304 \text{ km s}^{-1}$ ) and PG 2349-014 ( $\bar{v} = -326 \text{ km s}^{-1}$ ) as being associated with the Magellanic Stream, while the remaining lower velocity features for the latter two sight lines may or may not be associated with the Stream (these are designated LG in Table 1). The O VI column densities of the MS components for these three sight lines are similar:  $\log N = 14.18 \text{ (NGC 7469)}$ , 14.13 (NGC 7714), and 14.00 (PG 2349-014).

For the three primary MS/MSe sight lines with positive Stream velocities, the situation is also complex. The association of the high velocity H I and O VI is fairly clear for Fairall 9. However, NGC 1705 and PKS 0558-304 both lie near to the Stream H I, but neither sight line intersects any obvious Stream H I emission (see Figure 15). The velocities of the O VI absorption features are similar to those of other H I clouds cataloged by Wakker & van Woerden (1991) in the neighborhood of these two directions, but the association of these O VI clouds with the Magellanic Stream is less clear than for Fairall 9 since they lie several degrees off of the main axis of the Stream. Nevertheless, small H I clouds associated with the Stream lie in the same area of the sky as these sight lines (Putman et al. 2002). The two sight lines exhibit high velocity C II absorption at velocities similar to those of the O VI. Given the similarity of the positive velocity O VI absorption to that seen at negative velocities in the other Stream directions, we tentatively classify the positive velocity O VI features shown in Figure 15 as highly ionized Magellanic Stream or Magellanic Stream extension gas. These features have O VI column densities of  $\log N = 14.33$  (Fairall 9), 14.31 and 13.78 (NGC 1705), and 13.68 (PKS 0558-504). We note that the only other MSe sight line in this region of the sky, HE 0226-4410, has a slightly smaller velocity ( $\bar{v} = 164 \text{ km s}^{-1}$ ) and a similar column density ( $\log N = 13.98$ ).

The highest velocity portions of the C II  $\lambda 1036.337$  absorption along the 6 sight lines shown in Figure 15 occur at velocities similar to those of the high velocity O VI absorption. At positive velocities, the C II absorption is completely confused with low velocity C II\*  $\lambda 1037.012$  absorption in the ISM (at +195 km s<sup>-1</sup> with respect to C II). As in the case of Complex C, the relationship between O VI and C II suggests that the C II is probably tracing ionized gas. The slight offset of the highest velocity portions of the C II absorption relative to the H I is consistent with an ionized boundary around the Stream. This finding also agrees well with higher resolution STIS data. Sembach (2002) presents a preliminary analysis of the high velocity gas along the NGC 1705 sight line and finds that the high velocity O VI absorption is offset slightly from the lower ionization gas. Furthermore, the O VI toward NGC 1705 has a somewhat smoother velocity structure and does not have the distinct component structure seen in the lower ionization lines with STIS.

## 6.4. The Outer Spiral Arm

Three low latitude sight lines in our sample lie in the general direction of the Outer Arm seen in H I 21 cm emission in the general direction  $49^{\circ} \leq l \leq 161^{\circ}, 4^{\circ} \leq b \leq 31^{\circ}$  at a Galactocentric distance of about 15.5 kpc (Kepner 1970; Haud 1992). HS 0624+6907 ( $l=145.7^{\circ}, b=+23.4^{\circ}$ ) exhibits Outer Arm H I emission but has no associated O VI feature. H 1821+643 ( $l=94.0^{\circ}, b=+27.4^{\circ}$ ) and 3C 282 ( $l=61.3^{\circ}, b=+17.5^{\circ}$ ) exhibit O VI absorption with  $\bar{v}_{LSR} \sim -119 \text{ km s}^{-1}$  and  $\bar{v}_{LSR} \sim -90 \text{ km s}^{-1}$ , respectively. These velocities are in excellent agreement with both the observed and expected H I velocities in the Outer Arm (-115 km s<sup>-1</sup> toward H 1821+643 and -85 km s<sup>-1</sup> toward 3C 282) (Hulsbosch & Wakker 1998; Haud 1992). These velocities are similar to those of some of the higher latitude Complex C sight lines at nearby longitudes, but it is unlikely

that the two complexes of gas are related.

#### 6.5. Extragalactic Clouds

Several high velocity clouds in our sample other than Complex C and the Magellanic Stream are excellent candidates for being located outside the Milky Way. We discuss below a few of those clouds that have been studied by previous investigators at other wavelengths.

## 6.5.1. The C IV HVCs Toward Mrk 509 and PKS 2155-304

The Mrk 509 sight line ( $l=35.97^{\circ}, b=-29.86^{\circ}$ ) passes through two highly ionized HVCs detected in C IV absorption that have ionization properties consistent with clouds irradiated by local extragalactic background radiation (Sembach et al. 1999). The C IV absorption components are centered at -283 km s<sup>-1</sup> and -228 km s<sup>-1</sup>. These clouds have little associated low ionization absorption. There is no detectable H I 21 cm emission directly along the sight line [log  $N({\rm H~I}) < 17.5$  ( $3\sigma$ )], although H I emission near the velocities of the C IV HVCs is present within a few degrees of the sight line (Sembach et al. 1995b).

Sembach et al. (2000) first detected O VI absorption between -345 and -100 km s<sup>-1</sup> toward Mrk 509 (see also Figure 2). The O VI absorption is prominent at -247 and -147 km s<sup>-1</sup>, with the lower velocity component shifted slightly redward of the high velocity C IV absorption. The detection of O VI at these velocities is somewhat unexpected, since photoionization by the extragalactic background is not expected to produce the observed quantities of O VI unless the path lengths are very long and the cloud sizes very large (see §9). At these velocities we find  $\log N({\rm O~VI}) \sim 14.36$ , which is a factor of  $\sim 10$  higher than predicted by the photoionization model that best fits the data for C IV and lower ionization stages (see Sembach et al. 1999). We conclude that additional ionizing sources are responsible for increasing the O VI column density above that expected for the pure photoionization case.

A similar result holds for the two highly ionized HVCs toward PKS 2155-304. These clouds are also likely ionized by the extragalactic background (Sembach et al. 1999), but they contain O VI in quantities much greater than those expected for a simple photoionization scenario. One possible explanation for the high velocity O VI features observed along both the Mrk 509 and PKS 2155-304 sight lines is that these are photoionized extragalactic clouds that have begun to interact with the hot Galactic corona or other low density medium (see §11).

## 6.5.2. The Isolated Compact HVCs Toward Ton S210 and Mrk 205

The class of high velocity H I clouds classified as "compact and isolated" based on their morphological properties is a difficult group of clouds to study in absorption at ultraviolet wavelengths since their sky covering factor is low ( $\lesssim 1\%$  for those cataloged by Putman et al. 2002). Various authors have suggested that the compact H I HVCs may be distant (greater than a few hundred kpc) analogs of nearer H I HVCs (e.g., Braun & Burton 2000; Burton, Braun, & Chengalur 2001), but this hypothesis is not yet widely accepted. The two metallicity measurements available for these clouds suggests that the gas has (O/H) < 0.5 solar (Sembach et al. 2002), which is consistent with either a low-metallicity extragalactic origin or a Magellanic origin.

Two sight lines in our sample pass through or very near to isolated compact HVCs. Ton S210  $(l=224.97^{\circ},b=-83.16^{\circ})$  lies behind the outer regions of CHVC 224.0–83.4–197. The properties of this cloud are considered by Sembach et al. (2000, 2002), who find O VI absorption near the velocity of the H I 21 cm emission  $(v_{LSR} \approx -200 \text{ km s}^{-1})$ . They base their upper limit of (O/H) < 0.5 solar (3 $\sigma$  confidence) on the non-detection of the O I  $\lambda$ 1039.230 line in the FUSE spectrum of this object. The H I column derived from the Lyman-series H I absorption is consistent with the H I column from the 21 cm measurements. Sembach et al. (2002) also find that the high velocity gas in this direction contains as much hot H<sup>+</sup>, as inferred from the O VI absorption, as H I, suggesting that the cloud has a substantial ionized outer boundary. We discuss the production and significance of such a boundary in §11.

The  $-200~{\rm km\,s^{-1}}$  velocity of the CHVC 224.0–83.4–197 O VI absorption in the Ton S210 spectrum stands out in our sample since it is the only feature that has a negative LSR velocity at Galactic longitudes  $l > 180^{\circ}$  (see §5.4 and Figure 8). It also has the most extreme negative velocity in the GSR reference frame of any feature in the sample (Figure 9). The peculiar velocity of the cloud is substantially different from that of the bulk of the Magellanic Stream in this direction  $(v_{LSR} \sim -100~{\rm km\,s^{-1}})$ , but it is not yet possible to exclude the possibility that it could be a fragment of the tidal interaction between the Magellanic Clouds and the Galaxy (see Sembach et al. 2002).

The Mrk 205 sight line ( $l=125.45^{\circ}, b=+41.67^{\circ}$ ) passes through CHVC 125+41–207, which is detected in H I 21 cm emission (Braun & Burton 1999) and in Mg II absorption (Bowen & Blades 1993; Bowen, Blades, & Pettini 1995). This cloud probably also has a sub-solar metallicity, (Mg/H) < 0.2 solar (see Gibson et al. 2001b; Wakker 2001), but additional measurements are needed to confirm the low Mg abundance. As noted previously, the data for Mrk 205 are not optimal, and our limit of log  $N({\rm O~VI}) < 13.79~(3\sigma)$  is not terribly strict. Still, it appears that there is less O VI associated with the compact HVC along this sight line than there is with the compact HVC along the Ton S210 sight line.

#### 6.5.3. Local Group Galaxies

Several Local Group galaxies exhibit O VI absorption occurring at high velocities with respect to the LSR. While not necessarily "high velocity" in the rest frame of the galaxies, we mention them briefly here for completeness. Basic results for the Magellanic Clouds have been described elsewhere (Hoopes et al. 2002; Howk et al. 2002b) and are not considered further here other than to note that the data for both galaxies are consistent with the idea that each is surrounded by a substantial halo of O VI. The SMC also exhibits O VI enhancements caused by local structures (e.g., supernova remnants, superbubbles, etc.). The O VI column densities in the Magellanic Cloud halos are comparable to those found for the halo of the Milky Way, despite the lower metallicities and lower masses of the Clouds.

A search for O VI in the halos of M 31 and M 33 in the directions of several objects yields mixed results. Wannier& Andersson (2002) detect O VI absorption toward QSO 0045+3926 (a.k.a. RXJ0048.3+3941 or IO And) at an LSR velocity of  $-296~{\rm km\,s^{-1}}$ . QSO 0045+3926 is located at  $5.3 \times R_{25}$  from the center of M 31. The measured velocity is within  $\sim 10~{\rm km\,s^{-1}}$  of that expected from an extension of a flat rotation curve for M 31 at the location of the QSO. A high negative velocity O VI component is seen in many directions in this region of the sky ( $l \sim 120^{\circ}, b \sim -25^{\circ}$ ), so it is difficult to know for certain whether the O VI feature toward QSO 0045+3926 is unique to M 31 (see Wakker et al. 2002). High negative velocity absorption is also seen in the direction of several H II regions in M 33 (e.g., NGC 595 and probably NGC 588). However, Wakker et al. (2002) find no convincing evidence for an extended, corotating O VI halo around M 33 at a level of log  $N({\rm O~VI}) > 14$  based on the non-detection of positive velocity gas at M 33 velocities along several sight lines that pass near to M 33. Additional high quality FUSE observations of other sight lines in the directions of M 31 and M 33 would be useful.

Several sight lines in our sample pass within modest impact parameters (< 15 kpc) of smaller Local Group galaxies (e.g., Draco, Leo I, Ursa Minor, Carina, Sculptor). None of these show unambiguous evidence of O VI absorption (see Wakker et al. 2002 for details).

## 7. HIGH VELOCITY H I 21 CM EMISSION WITH NO CORRESPONDING O VI ABSORPTION

In general, O VI absorption is seen at velocities at which high velocity H I 21 cm emission is detected. However, there are a few notable exceptions to this rule. We list the H I column densities and the O VI limits for these 6 cases in Table 9. Most of the O VI non-detections occur for sight lines with low FUSE data quality (Q = 1 - 2 in 5/6 cases). However, in all cases, the non-detection is significant. One additional case not listed in Table 9 is the Complex A H I emission at -145 km s<sup>-1</sup> toward PG 0832+675; since this star lies in front of Complex A, no O VI absorption is expected.

The absence of O VI along the sight lines listed in Table 9 may be due to small-scale structure within the high velocity gas sampled by the larger H I beams. With the exception of ESO 265-G23, the absorption traced by C II  $\lambda 1036.337$  at the H I velocities noted is relatively weak, which supports the idea that these sight lines pass through low density regions of the high velocity gas encompassed within the field of view of the H I 21 cm observations. Furthermore, in three cases (Complex A, Complex C, and the Outer Arm), other sight lines in the sample show both H I 21 cm emission and O VI absorption even though the sight lines in Table 9 do not.

The Complex M sight line toward Ton 1187 does not exhibit high velocity O VI, which may be due to either lower ionization or small-scale structure. Complex M has been detected in H $\alpha$  emission by Tufte et al. (1998), which indicates that ionized gas is clearly present in some regions of the cloud. Complex M may contain some small-scale structure since high velocity absorption in lower ionization lines is present toward BD+382182 ( $d\sim4.0$  kpc) but not toward HD 93521 ( $d\sim1.9$  kpc), which is less than 30' away (see Danly, Albert, & Kuntz 1993; Wakker 2001). The smaller distance of HD 93521 may also explain the absence of Complex M absorption in this direction if Complex M lies beyond z  $\sim1.5$  kpc.

Either small-scale structure or ionization may be viable explanations for the absence of O VI in the remaining H I HVCs in Table 9 (WD, WW478, WW84). A possible alternative explanation may be that the gas has a very low metallicity, which would be very interesting since it would imply that the clouds are located at large distances. (Initial estimates indicate that clouds WD and WW84 have metallicities  $Z\sim0.1$ .) This hypothesis could be tested and the metallicities refined by obtaining high angular resolution H I data in conjunction with suitable STIS observations of the three sight lines.

## 8. NEW HIGH VELOCITY CLOUDS IDENTIFIED IN O VI

We observe high velocity O VI along many sight lines for which there are no previous detections of high velocity H I 21 cm emission. This suggests that much of the high velocity gas in these directions is highly ionized. We discuss some of these features in this section.

## 8.1. High Positive Velocity O VI "Wings"

Many of the sight lines in our sample exhibit broad, weak O VI absorption features that extend asymmetrically from the Galactic thick disk/halo absorption velocities out to high positive velocities. Examples are shown in Figure 16, where we have plotted the continuum-normalized O VI  $\lambda 1031.926$  absorption profiles for 22 sight lines as a function of LSR velocity. In a few cases, the extensions (or wings) comprise a significant fraction of the total O VI absorption along the sight line, but in most cases the positive velocity wings extending beyond  $v_{LSR} \approx +100 \,\mathrm{km\,s^{-1}}$  are much weaker than the thick disk/halo absorption along the same sight lines. Two general groupings of

clouds listed in Table 1 other than the Magellanic Stream display high positive velocities. These are the extreme positive velocity clouds in the north Galactic octant between  $180^{\circ} < l < 360^{\circ}$  (designated EPn in Table 1), which have properties similar to those of identified H I HVCs in the same general location (but not necessarily along the same sight lines), and the group of clouds designated 0th that lie predominantly in the northern octant containing Complex C and that have no identifiable counterpart in H I 21 cm emission.

All of the wing features carry a primary designation of EPn (11/22 sight lines), 0th (10/22 sight lines) or MS (1/22) in Table 1. These features are denoted with a dagger (†) mark attached to their HVC identification. It is important to note that not all EPn or 0th features in Table 1 are broad absorption wings. Eighteen of the 22 sight lines with high positive velocity wings are located in the northern Galactic sky. The four sight lines in the southern sky (e.g., Mrk 509, NGC 1705, PKS 2005-489, PKS0405-12) are widely scattered in longitude and do not appear to be associated in any obvious way with the 18 northern sight lines. The absorption wings can be seen quite clearly in the positive velocity channel maps shown by Wakker et al. (2002). We present a summary of the sky positions in Figure 17, where we indicate column density of the wing features in the same manner as in the top panel of Figure 6.

The similarities in the general locations of the northern sight lines exhibiting absorption wings and in their velocities suggest that many of the O VI wing features could have a common origin. One possibility is that the wings trace hot gas expelled from the Galactic disk. Sembach et al. (2001b) examined the absorption toward 3C 273 and found that the high positive velocity O VI in that direction has no detectable counterpart in other species, including C IV. They interpreted the high velocity O VI absorption as an indicator of hot gas flowing out of the Galactic disk. The 3C 273 sight line passes through Radio Loops I and IV (Berkhuijsen, Haslam, & Salter 1971) and through a region of enhanced soft X-ray emission associated with the North Polar Spur (Snowden et al. 1995). The radio loops are filled with X-ray emission and were probably created by supernovae in the Galactic disk (Iwan 1980; Snowden et al. 1995). The absence of lower ionization absorption and the presence of 0.25 keV emission suggests that the O VI-bearing gas is hot  $(T \sim 10^6 \text{ K})$ . Not all of the northern sight lines with high positive velocity wings lie in the direction of Loop I or the North Polar Spur, so it is not possible to associate all of these wings with these two large Galactic structures. However, similar physical processes may be at work along many of these sight lines, and the wider-spread existence of the wings beyond the confines of Loop I may signal a larger scale production and acceleration of hot gas in the northern Galactic sky than in the south.

An additional argument in favor of the idea that some of the positive velocity wings trace gas expelled from the Galactic disk is that hot gas expelled from the Galactic disk, perhaps as part of a "Galactic fountain" (Shapiro & Field 1976; Bregman 1980; Norman & Ikeuchi 1989), would likely contain O VI. Although most Galactic fountain models start with the assumption of a much hotter flow ( $T \sim 10^6 \, \mathrm{K}$ ), entrainment of cold gas in the flow or a lower temperature fountain would result in lower temperatures compatible with the production of O VI. Lower temperature fountain models can explain the kinematics of some of the intermediate velocity clouds (Houck & Bregman 1990).

The thick disk and low halo of the Milky Way contain a substantial amount of O VI; the typical O VI column density for a sight line perpendicular to the Galactic plane is  $\log N \sim 14.12$ , with a  $\sim 0.25$  dex enhancement above this value in the northern Galactic hemisphere (Savage et al. 2002b). The enhancement of the thick disk O VI in the north may indicate a generally elevated level of hot gas production these latitudes. For a few sight lines, like ESO 572-G34, Mrk 734, PG 1001+291, or IRAS F1143-1810, the distinction between displaced thick disk/halo absorption and high velocity absorption is particularly nebulous.

Alternatively, some of the broad O VI absorption wings may be entirely unrelated to the thick disk of the Milky Way. Some of the gas could be tidal debris remaining from encounters of the Milky Way and the Magellanic Clouds or other small galaxies. Most of the wing sight lines lie near the orbit of the Magellanic system. Another possibility might be that the wings are the positive velocity counterparts of the negative velocity LG features in the southern Galactic sky. The primary drawback to both of these hypotheses is that absorption wings are not discrete features like those associated with the Magellanic Stream (MS, MSe) or Local Group (LG) features in the south, and at least qualitatively, they appear to be a continuation of the thick disk/halo velocity distribution. Additional observations of other species at these velocities, especially if abundances could be derived, would be particularly valuable in discriminating between the possible origins of the wings.

Finally, we call attention to the Mrk 509 sight line, which is one of the southern directions in the sample with a positive velocity wing. Unlike the 3C 273 sight line, this wing is detected in other species, including Si II, Si IV, C IV, and N V (see Sembach et al. 1999). In this case, the positive velocity wing is likely related to gas in the low halo of the Galaxy. The sight line passes within 5 kpc of the Galactic center, and several other sight lines to halo stars near the Galactic center show similar features in C IV and Si IV (e.g., Savage, Massa, & Sembach 1990; Sembach, Savage, & Massa 1991; Sembach, Savage, & Lu 1995).

#### 8.2. High Velocity O VI in the Local Group?

A subset of features listed in Table 1 have a category of LG (Local Group) assigned to them. This label is suggestive of an origin and location outside the Milky Way and was chosen because the absorption has some unusual properties. For most of these features, there is no obvious H I 21 cm emission at similar velocities directly along the sight lines. The most extensively studied examples include the cloud toward Ton S210 (see §6.5.2) and the high negative velocity clouds toward Mrk 509, which have ionization properties more indicative of clouds bathed in the extragalactic ionizing background field than of clouds in the halo of the Galaxy (see §6.5.1). All of the LG clouds are located in the southern Galactic hemisphere, mostly in the  $35^{\circ} < l < 140^{\circ}$  longitude range. This is also the same general area of sky containing many of the MSe sight lines.

Various authors have considered the possibility that some of the clouds in this general region

of the sky (Local Group barycenter) and in the opposite direction (Local Group anti-barycenter) belong to a similar population of clouds located outside the Milky Way (e.g., Blitz et al. 1999). If we consider various standards of rest for the subsample of objects having LG, MSe, or EPn classifications in Table 1, we find the average velocities and dispersions listed in Table 10. The dispersion about the mean centroid velocity,  $\sigma_{\langle \bar{v} \rangle}$ , is a factor of two smaller in the LGSR reference frame than in the GSR reference frame, and a factor of 4 smaller than in the LSR reference frame. A similar result can be seen in Figure 7 for the entire ensemble of high velocity features in our sample, but restricting the sample to exclude points associated with known nearby features (e.g., Complexes A and C, the Outer Arm, the Magellanic Stream) results in a clearer difference between the rest frames.

While such a reduction is a necessary consequence for a distributed population of Local Group clouds, it is not a sufficient requirement. The reduction indicates that the clouds are not located nearby (i.e., d < 1 kpc), but it cannot be used as the sole justification for a Local Group location for several reasons. A sample of clouds located within  $\sim 100$  kpc of the Milky Way may have a significantly smaller dispersion in the GSR than in the LSR, but the difference between the GSR and LGSR frames would be difficult to ascertain without a very large sample because of selection biases in the directions chosen for study. An equally important bias is the strong selection against clouds with  $|v_{LSR}| \lesssim 100$  km s<sup>-1</sup> in our sample, and thus the omission of clouds with both large and small values of  $|v_{GSR}|$  and  $|v_{LGSR}|$ . For example, a cloud with  $v_{LSR} = 50$  km s<sup>-1</sup> in the direction  $b = 45^{\circ}$ ,  $l = (0^{\circ}, 30^{\circ}, 60^{\circ}, 90^{\circ}, 120^{\circ}, 150^{\circ}, 180^{\circ})$  has  $v_{GSR} = (50, 128, 185, 206, 185, 128, 50)$  km s<sup>-1</sup> and  $v_{LGSR} = (-19, 79, 163, 209, 206, 155, 69)$  km s<sup>-1</sup>. Therefore, this sampling bias can cause the derived GSR and LGSR velocity distributions to be narrower (or perhaps even broader) than the actual distributions, depending on the velocities of the positions of the clouds omitted in the LSR velocity range  $|v_{LSR}| \lesssim 100$  km s<sup>-1</sup>.

## 9. PRODUCTION OF O VI

Conversion of O V into O VI requires an energy of 114 eV, which in principle can be supplied by either absorption of photons or by collisions with other species (primarily electrons). We favor collisional ionization as the primary production mechanism for most of the high velocity O VI observed. We discuss the reasons for this preference after considering the collisional ionization and photoionization scenarios described below.

#### 9.1. Collisional Ionization in Hot Gas

#### 9.1.1. General Considerations and Possible Relationship to X-ray Absorption Lines

In collisional ionization equilibrium, the ionization fractions for each element depend on the abundances and temperature of the gas. For a plasma with solar abundances, O VI has a peak ionization fraction  $f_{\rm O\,VI}=({\rm O\,VI/O})\sim 0.22$  at  $T\sim 2.8\times 10^5$  K (Sutherland & Dopita 1993). Although this is often the canonical temperature quoted when referring to collisionally ionized O VI, the abundance of O VI remains high ( $f_{\rm O\,VI}>0.05$ ) at temperatures of  $(2-4)\times 10^5$  K. In non-equilibrium, time-dependent cooling situations, the temperature of peak O VI ionization fraction does not change significantly, but at lower temperatures the ionization fractions are larger than in the equilibrium case (see Shapiro & Moore 1976; Sutherland & Dopita 1993). For example, Shapiro & Moore (1976) find that  $f_{\rm O\,VI}>0.03$  down to  $T\sim 2\times 10^4$  K for a gas cooling isochorically from an initial temperature of  $10^6$  K. The peak ionization fraction diminishes to account for this increase in  $f_{\rm O\,VI}$  at lower temperatures, but  $f_{\rm O\,VI}$  at  $T>T_{\rm peak}$  remains similar to its value under conditions of collisional ionization equilibrium.

We compare the observed column densities of O VI and other well-observed high ions to the column density predictions of various collisional ionization models in the next section. Here, we note that recent X-ray absorption-line observations with the Chandra X-ray Observatory suggest that the zero-redshift column densities of higher ionization species, such as O VII (and perhaps O VIII), may be very large:  $\log N(\text{O VII}) \gtrsim 16$  (Fang & Sembach 2002; Nicastro et al. 2002). In collisional ionization equilibrium at  $\log T(K) = (6.0, 6.2, 6.4), N(O VII)/N(O VI) = (255, 233, 194),$ respectively (Sutherland & Dopita 1993). For  $\log N({\rm O~VII}) = 16$ , this implies  $\log N({\rm O~VI}) \sim$ 13.6-13.7 if the gas has  $T\sim 10^6$  K. Thus, the amount of O VI contained in the hot gas traced by the X-ray absorption could be roughly comparable to the amounts of O VI found for the typical thick disk/halo absorption or the high velocity gas. Even if the gas is much hotter, say  $\sim 10^7$  K, the amount of O VI predicted for such a large O VII column density  $[\log N(\text{O VI}) \sim 13.3]$  would still be detectable with FUSE. However, it is highly unlikely that all of the observed O VI in either the Galactic disk/halo or the high velocity gas is related exclusively to the hotter X-ray gas since lower ionization species (e.g., HI, CII, CIV) are seen at similar velocities and have miniscule ionization fractions in gas at temperatures exceeding 10<sup>6</sup> K. It remains to be seen whether the velocity structure of the higher temperature (O VII) gas is more consistent with disk/halo absorption or high velocity cloud absorption since the velocity resolution of the X-ray data is currently too poor to discriminate between local Milky Way features and a more pervasive Local Group medium. Comparisons of X-ray emission and absorption-line strengths along individual sight lines may help to discriminate between these possibilities.

## 9.1.2. Insights from Lower Ionization Stages

Additional information about absorption by high ionization species is available for several of the sight lines in our sample. We list the values of  $N({\rm O~VI})/N({\rm C~IV})$  and  $N({\rm O~VI})/N({\rm N~V})$  for several of the high velocity O VI features in Table 11, including the Magellanic Stream, Complex C, and several Local Group clouds. The ratios are integrations over the velocity ranges covered by the high velocity O VI features and thus are averages for the cases considered. We also list the ratios predicted by several by collisional ionization models and the photoionization model discussed below. The observed ratios of O VI/C IV and O VI/N V are typically greater than unity, with the possible exception of the highly ionized clouds toward Mrk 509.

The collisional ionization models considered in Table 11 include radiative cooling of  $10^6$  K gas (as in a Galactic fountain flow), thermal conduction in the presence of magnetic fields, turbulent mixing of hot  $(T \sim 10^6 \, \text{K})$  and warm  $(T \sim 10^4 \, \text{K})$  gases, and time-averaged cooling of shock-heated gas in evolved supernova remnants. The references and key assumptions for each of the models are provided in the notes at the end of the table. Spitzer (1996) summarizes these models and provides a brief discussion of the ratios for the Galactic disk and halo. Comparisons based on more extensive information for the Galactic halo have been given elsewhere (Sembach, Savage, & Tripp. 1997; Savage, Sembach, & Lu 1997, Savage et al. 2002b). In addition to the specific models listed in Table 11, we have also tabulated the predicted ratios if the gas is in collisional ionization equilibrium using the ionization fractions calculated by Sutherland & Dopita (1993) and the solar abundances recommended by Holweger (2001); the detailed dependences of the high ion ratios on temperature are shown in Figure 18. Incorporation of C, N, and O into dust should not affect these ratios significantly since all three elements are found predominantly in the gas phase, but the ratios may be affected if there is a non-solar relative abundance pattern (e.g., if N/O is sub-solar, as may be the case for Complex C; Richter et al. 2001).

#### 9.2. Photoionization

#### 9.2.1. Extragalactic Radiation

There is a considerable amount of information in the literature describing the conditions under which photoionization is relevant for highly ionized species such as O VI. Here, we consider the simple case of a plane-parallel slab of gas bathed in the extragalactic background produced by the integrated light of QSOs and AGNs. Since all of the absorption features studied here occur within a few hundred km s<sup>-1</sup> of the systemic velocity of the Milky Way, we consider only the ionization of gas at zero redshift. We used the ionization code CLOUDY (v94.00; Ferland 1996) to compute the ionization fraction of O VI ( $f_{O VI}$ ) in cases where the gas is optically thin to ionizing radiation ( $\tau_{HI} < 1$ ; log  $N({\rm H~I}) < 17.2$ ). We assumed the QSO spectral energy distribution given by Madau (1992) normalized to a mean intensity at the Lyman limit  $J_{\nu_0} = 1 \times 10^{-23}$  erg cm<sup>-2</sup> s<sup>-1</sup> Hz<sup>-1</sup> sr<sup>-1</sup>

(Donahue, Aldering, & Stocke 1995; Haardt & Madau 1996; Shull et al. 1999). This procedure followed that outlined by Sembach et al. (1999)

We summarize the results of these calculations in Figures 19 and 20, where we plot  $f_{\rm O\,VI}$  and  $N({\rm O\,\,VI})$  as functions of ionization parameter [  $U=(n_\gamma/n_H)\propto (J_\nu/n_H)$  ] for a metallicity  $\log Z=-0.5$  and neutral hydrogen column densities  $\log N({\rm H\,\,I})=14$  to 17. The values of  $f_{\rm O\,VI}$  do not depend strongly on the metallicity – the curves shown are similar to those for  $\log Z=-2$  to 0. These calculations show that  $f_{\rm O\,VI}<0.25$  at most values of U, with the highest values occurring for values of  $\log U>-1.5$ . For  $\log U\lesssim -2$  (i.e.,  $n_H>3\times 10^{-5}~{\rm cm}^{-2}$ ),  $f_{\rm O\,VI}\lesssim 0.01$ . The values of  $f_{\rm O\,VI}$  do not depend strongly on  $N({\rm H\,I})$  for  $N({\rm H\,I})<10^{17}~{\rm cm}^{-2}$ .

In addition to the flux from AGNs and QSOs, the local extragalactic ionizing radiation field includes contributions from the integrated light of starburst galaxies and nearby galaxies (see Shull et al. 1999). If the high velocity clouds are located within  $\sim 100$  kiloparsecs of the Milky Way, the detailed ionization properties of the clouds should depend primarily upon the escape of ionizing photons from the Milky Way and LMC (Bland-Hawthorn & Maloney 1999). However, starlight should not affect  $f_{\rm OVI}$  or the observed O VI column densities. Inclusion of an additional stellar spectrum in our photoionization models, like that produced by early-type OB stars, does not appreciably alter the predicted ionization fraction of O VI. Furthermore, despite intensive searches for stars associated with HVCs and the Magellanic Stream, none have yet been found (see Irwin, Demers, & Kunkel 1990; Simon & Blitz 2002), which indicates that there are few, if any, in situ stellar sources of ionizing photons. The Magellanic Bridge, a much younger portion of the Magellanic system than the Stream, contains hot stars (Irwin et al. 1990) but is generally considered to be more closely associated with the Magellanic Clouds than with the high velocity cloud system surrounding the Milky Way. None of the sight lines in this O VI survey pass through the Magellanic Bridge (but see Lehner 2002 for an example).

In the models shown in Figure 20, N(O VI) increases with increasing hydrogen column density and scales approximately linearly with metallicity. The cloud size also scales roughly linearly with the total H I column density and metallicity over the column density ranges considered. A few simple scaling laws apply for fixed values of U:

$$N({\rm O~VI}) \propto Z \times N({\rm H~I})$$
  
 $n_{HI} \propto n_H \times (n_H/J_{\nu})$   
 $D = n_{HI}^{-1} \times N({\rm H~I})$ 

At a given ionization parameter, smaller sizes occur for clouds with lower H I column densities or higher metallicities. To produce an O VI column density of  $10^{13}$  cm<sup>-2</sup> requires a cloud size  $D \gtrsim 40$  kpc for  $n_H \geq 10^{-5}$  cm<sup>-3</sup>,  $\log N({\rm H~I}) > 14$ , and  $\log Z = -0.5$ . To produce an O VI column density of  $10^{14}$  cm<sup>-2</sup> requires cloud sizes in excess of several hundred kiloparsecs, even if the metallicity is as high as solar. The assumption of a uniform, constant density cloud may break down as the cloud size increases beyond these sizes. Cloud sizes as large as these may be possible for pervasive media

outside galaxies (e.g., a Local Group medium) but are clearly too large to be contained within the Milky Way).

We show the detailed behavior of the O VI/C IV and O VI/N V ratios expected for the photoionization model in Figure 21, assuming relative abundances of C, N, and O equivalent to their solar proportions. The ratios depend on the ionization parameter (or gas density for a fixed ionizing spectrum) and the H I column density, so we show ratios for values of  $\log N({\rm H~I})=14$  and 17. The ratios are not sensitive to metallicity in the range Z=0.01-1.0; the metallicity dependence is weaker than the H I dependence. The expected column density of O VI is greater than that of C IV only for  $U\gtrsim -1.5$ , which corresponds to a density of  $\lesssim 10^{-5}~{\rm cm}^{-3}$ . In Table 11 we list the high ion ratios for densities of  $10^{-5}~{\rm cm}^{-3}$  and  $10^{-4}~{\rm cm}^{-3}$ . In a few cases (e.g., Mrk 509, PKS 2155-304), the photoionization models can reproduce the observed ratios of O VI/C IV and O VI/N V if the H I column density is very low  $[N({\rm H~I})\sim 10^{14}~{\rm cm}^{-2}]$  and the gas density is low  $(n_H\lesssim 10^{-4}~{\rm cm}^{-3})$ . However, the total observed value of  $N({\rm O~VI})$  is difficult to reproduce unless the clouds are very large.

#### 9.2.2. Galactic Radiation

Much of the discussion about photoionization in the preceding section is relevant for discussions of photoionization by Galactic sources. In both the extragalactic and Galactic cases, the ionization parameter must be high for a substantial amount of O VI to be produced. The production of O VI by ionizing Galactic sources is restricted to special situations in which the interstellar gas has a very low density or lies in close proximity to the ionizing source. The dilute ultraviolet radiation that leaks out of H II regions and maintains the ionization of the warm ionized interstellar medium (WIM:  $n_e \sim 0.08 \text{ cm}^{-3}$ ,  $h_z(\text{WIM}) \sim 1 \text{ kpc}$ ; see Miller & Cox 1993 and Reynolds 1993) is insufficient to ionize O VI since the OB stars responsible for the WIM have strong He II absorption edges at 54 eV.

Several authors have considered the production of highly ionized atoms by radiation from hot degenerate objects, such as He-poor white dwarf stars. Dupree & Raymond (1983) calculated the O VI column densities expected in the Strömgren spheres surrounding pure hydrogen white dwarfs with surface temperatures  $T \sim 60,000\,\mathrm{K}$ . They found that the column density of O VI depends upon both the size of the O VI Strömgren region and the ambient ISM density; for ambient densities of 0.01 and 0.1 cm<sup>-2</sup>, the radii of the transition regions where the H I fraction is 10% are 6.8 and 2.1 pc, and the O VI columns are  $1.4 \times 10^{12}$  and  $5.6 \times 10^{12}$ , respectively. (The O VI Strömgren spheres are much smaller than the traditional H II Strömgren spheres.) Thus, the O VI produced in such a region is both confined and weak compared to the observed O VI in the high velocity gas. Over a typical 1 kpc path through a 0.01 cm<sup>-3</sup> ISM, Dupree & Raymond (1983) predict a total O VI column density of  $(0.5-1.4)\times 10^{13}$  cm<sup>-2</sup> might be intercepted by a sight line given the (uncertain) space density of He-poor white dwarf stars. This O VI column density is lower than observed for all features in Table 1, often by an order of magnitude or more. Increasing the path

length beyond  $\sim 1$  kpc through the Galactic halo does not increase this prediction significantly since the space density of white dwarf stars is presumably highest near the Galactic plane.

Bregman & Harrington (1986) have also considered the production of O VI in the Galactic halo, with a radiation field that includes both Galactic sources of radiation (hot stars, planetary nebulae, the Galactic soft X-ray background) and a contribution from the extragalactic background. They find that a path length of  $\sim 10$  kpc through a medium with  $n_H = 0.001$  cm<sup>-3</sup> is needed to produce an O VI column density of  $\sim 1 \times 10^{13}$  cm<sup>-2</sup>. In this regime, the conditions required for the production of O VI essentially revert to the situation considered in §9.2.1, only the problem of moving such extensive regions of the Galactic halo at high enough velocities to explain the observed O VI absorption features becomes untenable, even if the entire halo decouples from the underlying disk (see §10.2).

### 9.3. The Line Width - Column Density Relation

There is an interesting correlation in the column densities and velocity widths of O VI absorbers found in different astrophysical environments. This trend was first noticed by Heckman et al. (2002) for starburst systems and some of the Galactic and HVC absorption systems. In Figure 22 we plot O VI column density versus line width for O VI features in various environments, including the Galactic disk and halo, high velocity gas, and the Magellanic Clouds. The Galactic disk points are from the Copernicus O VI survey (Jenkins 1978a, 1978b), which sampled gas within  $\sim 1$  kpc of the Sun; only data points having O VI  $\lambda 1031.926$  values of  $b = \sqrt{2\langle (v - \bar{v})^2 \rangle}$  without substantial uncertainties due to HD contamination are illustrated. The remaining data points are based on  $\lambda 1031.926$  measurements from FUSE. References to the sources for the data points can be found in the figure caption.

Production of O VI by photoionization should not produce the trend observed in Figure 22. Under conditions appropriate for photoionization, the line width should be dominated primarily by the temperature of the gas and the velocity separations of the different components. Thus, one could expect to observe either very low or very high column densities at widths appropriate for photoionized gas (typically,  $T \sim 10^4 - 10^5 \,\mathrm{K}$ , or b  $\sim 2 - 10 \,\mathrm{km}\,\mathrm{s}^{-1}$ ). There is no reason to expect that all such components should have a similar column density, and therefore the distribution of data points would be more scattered than observed.

Collisional processes should produce a good correlation between N and b since the column density scales linearly with gas flow velocities in most collisional ionization situations. Heckman et al. (2002) have described these relationships and extend the result seen in Figure 22 to higher column density absorbers seen in starburst galaxies. They also argue that the O VI absorbers detected in the low-redshift IGM are collisionally ionized, with the exception of a few discrepant systems. Since most of the O VI IGM absorbers and the high velocity O VI features occupy similar portions of Figure 22, understanding the ionization of one type of system in more detail may lead

to a better understanding of the other.

The data points for the high velocity O VI features follow the trend defined by the Galactic disk and halo points in Figure 22. The formal slope of the high velocity O VI data points  $(\Delta \log N/\Delta \log b)$  is 1.3, which is intermediate to the values of 0.8 for the thick disk/halo and 1.7 for the nearby disk. There is some indication that the data points for the high velocity O VI features are slightly more scattered about the best fit line than the disk or halo points:  $\sigma_{HV} \sim 0.36$  dex compared to  $\sigma_{disk} \sim 0.29$  dex and  $\sigma_{halo} \sim 0.15$  dex. This may result from additional bulk motions, flows, and turbulence within these clouds compared to clouds in the ISM of the Galaxy.

# 9.4. Ionization Synopsis

Given the above considerations, we consider it very likely that most of the high velocity O VI we observe is created primarily by non-equilibrium collisional ionization processes. This conclusion is supported by several findings. The amount of O VI produced by photoionization is smaller than the typical column densities observed unless the gas has a very low density and the clouds are extremely large – so large in fact that the sizes are incompatible with the distances to some HVCs (e.g., the Magellanic Stream and Complex C). Second, although the observed ionic ratios for some high velocity clouds can occur through photoionization under special circumstances, the inferred cloud sizes required are again too large to allow a cloud location within the Milky Way -Magellanic Cloud system. In other cases, the ionic ratios are more reflective of collisional processes and are similar to those found for Milky Way halo gas, which is even harder to photoionize than extragalactic clouds since the ionization sources (primarily OB stars) produce a softer radiation field than the extragalactic ultraviolet background. In the direction of Mrk 509, the ratios indicate that both photoionization and collisional ionization processes may contribute since the amount of C IV relative to O VI is higher than the standard collisional ionization models predict. The turbulent mixing layer models can reproduce the observed N(O VI)/N(C IV) ratio toward Mrk 509, but cannot simultaneously satisfy the constraints of the N(O VI)/N(N V) ratio. Finally, the high velocity O VI features show a significant correlation between O VI line width and column density, which is also observed for other O VI systems that are predominantly collisionally ionized (e.g., the Milky Way disk and halo, starburst outflows).

### 10. KINEMATICS OF THE HIGH VELOCITY GAS

# 10.1. Expectations for a Corotating Halo

By definition, the high velocity O VI absorption features considered in this study generally have  $|v_{LSR}| \gtrsim 100 \text{ km s}^{-1}$  with a few exceptions. This velocity cutoff provides isolation of the high velocity absorption from the absorption produced by the thick disk/halo of the Galaxy. The thick

disk/halo O VI absorption is roughly characterized by a patchy plane-parallel slab of hot gas with an exponential scale height of 2.3 kiloparsecs in the direction perpendicular to the Galactic plane (see Savage et al. 2002b). This scale height is comparable to the scale heights derived for other highly ionized species (e.g., C IV, N V) using more limited datasets available with the *HST* (Savage et al. 1997). The thick disk high ions profiles can be modeled reasonably well assuming that the thick disk/halo gas follows essentially the same pattern of rotation around the Galactic center as the underlying disk gas for regions within 1–2 kiloparsecs of the Galactic plane (Lu, Savage, & Sembach 1994; Savage et al. 1997). In some directions toward the Galactic center, this coupling may break down at higher altitudes (Sembach et al. 1991, 1995a). It is therefore useful to quantify the magnitude of the deviations from corotation and to consider whether the high velocity O VI features can be described within the context of various rotation models for the gaseous Galactic halo.

To test whether the high velocity O VI we observe can be modeled as a simple extension of the thick disk/halo distribution, we have calculated the O VI column density profiles expected for each sight line in the sample assuming that the O VI has a vertical scale height of 2.3 kpc, a typical velocity dispersion  $\sigma = 42.5 \text{ km s}^{-1}$  (b = 60 km s<sup>-1</sup>; Savage et al. 2002b), a mid-plane density  $n_0(O \text{ VI}) = 1.7 \times 10^{-8} \text{ cm}^{-3}$  (Jenkins, Bowen, & Sembach 2002), and a halo rotation speed identical to the rotation speed of the Galactic disk at the same Galactocentric radii. In this calculation we have used the Galactic rotation curve derived by Clemens (1985) with a solar orbital speed of 220 km s<sup>-1</sup> around the Galactic center. We terminated the calculation for each sight line at a distance of 10 kpc from the Galactic plane ( $\approx 4$  scale heights). (See Savage et al. (1990) for specific details about the computation of the line profiles.) After converting each column density profile into a synthetic absorption profile, we identified the extreme positive and negative velocities  $(v_{pos}, v_{neg})$ at which each model absorption profile recovered to within 5% of the continuum. We chose the velocity interval between these cutoffs as a reasonable velocity range over which one would expect to detect weak high velocity features that are extensions of the simple thick disk/halo distribution, considering the quality of the FUSE data. Broadening this interval to accommodate slightly more sensitive measures of the absorption does not change our conclusions below appreciably. Narrowing it strengthens them.

The sight lines with the most negative predicted velocities are ESO 141-G55 ( $l=338.2^{\circ}, b=-26.7^{\circ}, v_{neg}=-169~{\rm km\,s^{-1}}$ ), PKS 2005-489 ( $l=350.4^{\circ}, b=-32.6^{\circ}, v_{neg}=-164~{\rm km\,s^{-1}}$ ), and 3C 382.0 ( $l=61.3^{\circ}, b=17.4^{\circ}, v_{neg}=-163~{\rm km\,s^{-1}}$ ). The sight lines with the most positive predicted velocities are ESO 265-G23 ( $l=285.9^{\circ}, b=16.6^{\circ}, v_{pos}=187~{\rm km\,s^{-1}}$ ), Mrk 509 ( $l=36.0^{\circ}, b=-29.9^{\circ}, v_{pos}=153~{\rm km\,s^{-1}}$ ), and PKS 0558-504 ( $l=258.0^{\circ}, b=-28.6^{\circ}, v_{pos}=150~{\rm km\,s^{-1}}$ ),

We show the results of these calculations in Figure 23, where we plot the difference between the predicted cutoffs and the observed O VI velocity centroids as functions of Galactic longitude and latitude. The figure is similar to Figure 8, where we plot  $v_{LSR}$  versus l and b, except that the deviation velocity,  $\Delta v = \bar{v} - v_{pred}$ , is a measure of how far beyond the expected cutoffs each O VI

feature lies. Here,  $v_{pred}$  is equal to  $v_{neg}$  or  $v_{pos}$ , depending upon sign of the observed velocity  $\bar{v}$ . The vertical bar on each point represents the width ( $\pm$ b in km s<sup>-1</sup>) of the high velocity feature (see Table 1) to give a sense of the velocity extent of the absorption. The symbols are coded according to the classifications in Table 3 and are the same as in Figure 3 to make comparisons of the figures easier. We plot horizontal dashed lines at  $\Delta v = \pm 30 \text{ km s}^{-1}$  to illustrate that most of the observed velocities lie well outside those expected for corotation even after accounting for a substantial amount of additional randomness to the velocity distribution of the smooth distribution of components assumed in the model.

There are several important things to note in Figure 23. First, in the Galactic longitude plot, there is a distinct trend in the distribution of data points with longitude. At  $l < 180^{\circ}$ , the values of  $\Delta v$  are predominantly negative, whereas at  $l > 180^{\circ}$  the values are predominantly positive. Second, most of the data points deviate by at least 30 km s<sup>-1</sup> from the predicted extrema; only 13 of the 85 points have  $|\Delta v| \leq 30$  km s<sup>-1</sup>. This clearly indicates that the deviation velocities are not described well by a corotating gas layer. (This is expected since the high velocity sample was selected in large part to avoid velocities associated with the Galactic thick disk and low halo.) Third, in the Galactic latitude plot, the deviations in the south  $(\sigma_{\Delta v} \sim 113 \text{ km s}^{-1})$  are on average a factor of  $\sim 1.4$  times larger than those in the north  $(\sigma_{\Delta v} \sim 83 \text{ km s}^{-1})$ . A summary of the means and dispersions in  $\Delta v$  for different Galactic quadrants is given in Table 12.

#### 10.2. Expectations for a Non-Corotating Halo

To see if the distribution of O VI velocities could be due to deviations from corotation in the halo gas layer, we have also calculated model O VI profiles assuming that the halo gas decouples from the disk gas. In these models, the halo decoupling begins at an altitude  $z_i$  and is complete at  $z_f$ ; the functional form of the decoupling is a linear decrease in rotation speed between  $z_i$  and  $z_f$ . We display the results for the model with  $z_i = 1$  kpc and  $z_f = 3$  kpc in Figure 24. This is equivalent to having a static, non-rotating halo above z = 3 kpc, with the predicted velocities beyond this distance simply being the projection of the Sun's motion in each direction.

There are several key differences in the velocities predicted by this model compared to the corotation model. The trend in  $\Delta v$  with Galactic longitude seen in Figure 23 has largely disappeared, and the differences between north and south have decreased substantially compared to the corotation model. The slight trend for negative values of  $\Delta v$  in the south and positive values of  $\Delta v$  in the north is weaker than before but still present. Inspection of Table 12 shows that the overall dispersion of  $\Delta v$  for this model is 84 km s<sup>-1</sup> compared to 115 km s<sup>-1</sup> for the corotation model.

Twenty-three data points in the non-corotation model have  $|\Delta v| \leq 30 \, \text{km s}^{-1}$ , considerably more than for the corotation case. Still, this is only 23 out of the 85 cataloged high velocity features, implying that even this model does not account for most of the velocities. Of these 23 features with  $|\Delta v| \leq 30 \, \text{km s}^{-1}$ , 9 are classified as 0th. The remainder are divided roughly equally between

the LG, EPn, and MSe categories. There is still a deviation well above and beyond that expected, regardless of whether or not the halo corotates (i.e., the O VI velocities do not obey any simple relation with the thick disk velocities.).

The smaller dispersion in the O VI deviation velocities in the non-corotating model suggests that much of the high velocity O VI does not know about the rotation of the Galaxy, but it does not imply that the Galaxy has a static halo of smoothly distributed O VI. The model assumes a smooth gas distribution, but the O VI in the thick disk/halo is known to be quite patchy in nature, even on small angular scales (Howk et al. 2002a). If there were a smooth gas distribution and the halo were not rotating, we would expect to see absorption profiles that had secondary absorption minima due to velocity crowding at the terminal velocities for some sight lines. We do not see such features.

### 10.3. Searching for Outflows or a Hot Galactic Wind

There is considerable interest in understanding whether galaxies have large-scale winds that are capable of altering the structure of the ISM and expelling heavy elements into the IGM. In all cases, the outflowing winds are expected to be hot, since it is typically supernovae and star-formation processes that power them. As a result, the best evidence for galactic winds often comes from X-ray observations and from ultraviolet measurements of highly ionized species such as C IV, N V, and O VI (see, e.g., Heckman 2002 and Martin 2002 for current discussions of this topic and additional references). An O VI outflow in the starburst galaxy NGC 1705 has been observed by FUSE (Heckman et al. 2001), and lower velocity hot gas flows may also be present in the LMC (Howk et al. 2002b).

In the Milky Way, there is evidence that a wind emanating from the Galactic center has resulted in the expulsion (or ionization) of much of the neutral ISM above  $z \sim 1$  kpc in the inner 3 kpc of the Galaxy (Lockman 1984). The possibility of a strong Galactic wind has been considered by Hirashita, Kamaya, & Mineshige (1997), while a review of more quiescent wind activity and Galactic "fountains" is given by Breitschwerdt & Komossa (2000). The detailed nature of a Galactic wind depends upon many factors, including the energy input at the base of the wind, the structure and density of the ISM, the gravitational potential of the Galaxy at the site of the wind flow, magnetic fields and cosmic ray support of material, and the efficiency of the entrainment of cooler material in the flow. Few of these variables are known in detail, but models of winds in rotating galaxies like our own indicate that a Galactic wind could be driven by cosmic rays and heated in part by Alfven waves, with the gas corotating with the underlying Galactic disk up to altitudes of several kiloparsecs (Zirakashvili et al. 1996).

Consider the case of a spherically-symmetric unbound wind that flows completely out of the Galaxy. The simplest directions to look for signs of an outflow would be directly toward or directly away from the Galactic center, since the effects of Galactic rotation would be minimized. Toward

 $l \sim 180^\circ$ , we see high positive velocity O VI, as expected. Toward  $l \sim 0^\circ$  we see both positive and negative velocity features. However, the number of sight lines in both directions is very limited. At high latitudes ( $|b| \gtrsim 60^\circ$ ), positive wind velocities should dominate, which is qualitatively consistent with the O VI velocities in Figure 8. At lower latitudes, the expected wind velocity depends on Galactic longitude and the distance of the wind particles from the Sun. In the range  $180^\circ < l < 270^\circ$ , positive velocities are expected since the gas lies outside the solar circle. Between  $l = 270^\circ$  and  $l = 360^\circ$ , positive velocities are expected for the wind beyond the Galactic center, while predominantly negative velocities are expected for gas within the solar circle on the near side of the Galactic center.

The altitude at which a sight line intercepts the wind influences the observed wind velocity; the projected velocity for higher-z sight lines would be lower than for sight lines passing nearer the disk of the Galaxy. Furthermore, if the source of the wind was not a localized phenomenon but was instead spread over the disk of the Galaxy (say, in spiral arm locations), then the gas motions may be dominated by regional activity. Indeed, evidence of localized outflow from the Scutum Supershell exists for several ionization stages, including O VI (Sterling et al. 2002). Some of O VI features we observe in our survey (e.g., the positive velocity absorption wings) are consistent with the presence of localized outflow from the Galactic disk. We conclude that the complexity of the high velocity O VI sky, selection effects, and the unknown extent of a Galactic wind make it difficult to find conclusive evidence for a large-scale Galactic O VI outflow, nor can we rule out its presence without additional information. Future observations targeted at addressing this issue in specific directions in both the Milky Way and the Magellanic Clouds are needed.

## 10.4. Expectations for O VI in the Local Group

Several authors have argued convincingly against a distributed Local Group location for many of the H I HVCs using statistical studies of the neutral gas in other galaxy groups (e.g., Charlton, Churchill, & Rigby 2000; Zwaan & Briggs 2000). One way to escape this argument is to require that the clouds be located close to the large galaxies within the groups ( $d \lesssim 100-200$  kpc). For clouds in the Local Group, this makes it difficult to distinguish between a cloud population related to the Milky Way and a truly Local Group population based on kinematical information alone (i.e., the dispersions in the cloud velocities in the GSR and LGSR reference frames are similar, and strong observational selection effects apply - see §8.2). As a result, additional information is needed to determine if the clouds are located in the Local Group.

For the subsample of high velocity LG, EPn, and MSe features considered in Table 10, the dispersions of the velocity distributions in the GSR and LGSR reference frames are smaller than the dispersion in the LSR reference frame. Furthermore, in the GSR and LGSR reference frames, the dispersions for this subsample are smaller than the dispersions listed in Table 6 for the entire high velocity O VI sample (Table 6). The shaded regions of Figure 7 highlight the velocity distributions of these 50 features. Several of the sight lines classified as LG have ionization or abundance information

that support an extragalactic location (§6.5). The MSe sight lines are included in this subsample, even though their velocities are similar to those of the Magellanic Stream, since their positions on the sky do not correspond to the locations of the bulk of the H I 21 cm emission from the Stream. Objects classified as LG, EPn, or MSe in Table 1 would be excellent candidates for concerted efforts to determine the ionized gas content, gas-phase conditions, elemental abundances, and distances of the high velocity gas.

Increasing the number of O VI absorption-line measurements along other sight lines in the regions of the sky where the LG, EPn, and MSe features are found is highly desirable. Unfortunately, with current instrumentation, the number of additional background sources bright enough to observe in reasonable integration times is limited. An alternate approach, that of imaging the O VI in emission at very faint levels over large fields of view, may soon be possible with the NASA's Small Explorer mission for Spectroscopy and Photometry of the Intergalactic Medium's Diffuse Radiation (SPIDR). Such measurements would help to set the context for the absorption-line measurements in this study and perhaps reveal the association (if any) of these features with other high velocity gas.

#### 11. DISCUSSION

High velocity O VI is both widespread and common along complete paths through the Galactic halo. The high velocity O VI traces numerous phenomena, including tidal interactions with the Magellanic Clouds (via the Magellanic Stream), accretion of low metallicity gas (e.g., Complex C), highly ionized clouds (e.g., the Mrk 509 HVCs), and the outflow of hot gas from the Galactic disk (e.g., the broad positive velocity absorption features). Distinguishing between all of the possible phenomena occurring at large distances from the Galactic plane is not easy, and clearly any attempt to treat all detections of the high velocity O VI as a single population of clouds would be a serious mistake. That being said, considerations of subsets of the high velocity O VI features suggest some intriguing possibilities.

Much of the high velocity O VI probably occurs at large distances from the Galactic plane. There have not yet been any detections of high velocity O VI at high latitudes toward halo stars out to distances of several kiloparsecs. The two stars in our sample are the most distant halo stars examined for high velocity O VI absorption ( $d \sim 8-10~\rm kpc$ ). In a study of approximately two dozen halo star sight lines, Zsargo et al. (2002) find low velocity O VI absorption associated with the Galactic thick disk/halo but no high velocity O VI absorption at  $|v_{LSR}| > 100~\rm km\,s^{-1}$ . Despite the difficulties encountered in estimating the stellar continua, this result is fairly robust, especially the absence of discrete high velocity features with modest optical depths. Broad absorption wings, like those discussed in §8.1, would be much more difficult to detect against stellar continua with substantial curvature than against the relatively smooth spectra of QSOs and AGNs. The number of halo sight lines toward hot stars examined for high velocity O VI absorption is small, so the absence of high velocity O VI in halo regions within a few kiloparsecs of the Galactic disk is by no

means ruled out. Some high velocity O VI is observed toward the Magellanic Clouds at velocities intermediate to those expected for the Galactic thick disk/halo and the Magellanic Clouds (Hoopes et al. 2002; Howk et al. 2002b). The distance of the high velocity O VI in this direction is unknown, but is likely to be more than a few kiloparsecs from the Galactic plane.

One possible explanation for much of the high velocity O VI is that it arises at the boundaries between cool/warm clouds of gas and a very hot  $(T > 10^6 \,\mathrm{K})$  Galactic corona or Local Group medium. A hot, highly extended corona much larger than the thick disk/halo region might be left over from the formation of the Milky Way or Local Group, or may be the by-product of continuous accretion of smaller galaxies over time. Interactions of this type have been proposed to explain the observed H $\alpha$  emission from the Magellanic Stream (Weiner & Williams 1996), the shape and confinement of some Stream concentrations (Stanimirovic et al. 2002), and the shapes of supergiant shells along the outer edge of the LMC (de Boer et al. 1998). N-body simulations of the tidal evolution and structure of the Magellanic Stream favor a low-density medium for imparting weak drag forces to deflect some of the Stream gas and providing a possible explanation for the absence of stars in the Stream (Gardiner & Noguchi 1996; Gardiner 1999). Moore & Davis (1994) also postulated a hot, low-density corona to provide ram pressure stripping of some of the Magellanic Cloud gas and to explain the absence of gas in globular clusters and nearby dwarf spheroidal companions to the Milky Way (see also Blitz & Robishaw 2000). Constraints on the density of the Galactic corona from considerations of the survivability of the Magellanic Stream range from  $n \lesssim 10^{-4} \; \mathrm{cm}^{-3}$  based on dynamical arguments [e.g., drag (Moore & Davis 1994)] to  $n \lesssim 10^{-5} \; \mathrm{cm}^{-3}$ based on thermal considerations [e.g., heating and evaporation (Murali 2001)]. In either case, there would be little X-ray emission from the extended corona or Local Group medium at these densities, and no observational constraints on the extragalactic X-ray background observed by ROSAT are violated by the presence of such a medium (see Rasmussen & Pedersen 2001).

In such a scenario, one would expect the O VI to occur at the boundaries between neutral or weakly ionized gas clouds and the hotter ( $T\gtrsim 10^6$  K) medium. The data for sight lines that pass through Complex C are consistent with the idea that the Complex C is falling into and interacting with a highly extended corona. The similarity in the general velocity structure of the H I and O VI indicates that the spatial relationship is probably also close (see Figure 14 and Table 8). The boundary between the H I and the hot corona is probably thin enough that the negative velocity extension of the O VI is essentially determined by the kinematics at the boundary (i.e., by the motion of the H I) rather than by larger scale thermal motions in hot gas or boundary layer. The distance of Complex C (d > 5 kpc, z > 3.5 kpc) is sufficiently large that any interactions must be occurring well above the Galactic plane, either with the Galactic corona or with the outer regions of the thick disk/halo.

Hydrodynamical simulations of clouds moving through a hot, low-density medium show that weak bow shocks develop on the leading edges of the clouds as the gas is compressed and heated (Quilis & Moore 2001). Although the simulations were motivated in an attempt to explain the "head-tail" structures seen for some HVCs as they pass through the lower halo (Brüns, et al. 2000;

Brüns, Kerp, & Pagels 2001), they also provide some guidance for lower density situations. The exact nature of the interaction depends on the relative speeds and densities of the two gases. The high velocity O VI features generally have velocities comparable to the adiabatic sound speed in a medium of the type described above, and both projection effects and motion of the medium itself (e.g., a Galactic wind) would serve to increase the Mach number of the O VI clouds. However, even if the clouds are not moving at supersonic speeds relative to the ambient medium, some viscous or turbulent stripping of the cooler gas occurs (see Quilis & Moore 2001). This type of turbulent mixing of hot and warm gases has been described in detail by Slavin, Shull, & Begelman (1993). Thermal conduction may also be efficient, depending upon the orientation of the magnetic field relative to the conduction front (Borkowski, Balbus, & Fristrom 1990). Fast ionization of cold gas may also occur through the "critical velocity effect" if the coronal plasma itself is magnetized (see Konz et al. 2001). Thus, the exact details of the mixing and heating of the gas depend on the geometry of the clouds, the entrainment velocity of the gas, the presence of magnetic fields, and several other physical quantities.

The presence or absence of neutral gas associated with the high velocity O VI in the interacting corona scenario would depend on several factors, most notably the mass of the cool/warm gas cloud passing through the corona and the heating efficiency. The good correspondence of the O VI absorption velocities and the H I 21 cm emission velocities in the directions of substantial H I concentrations (e.g., Complex C, the Magellanic Stream - see Figures 14 and 15 and Table 8) argue that the interface region between the corona and the cooler material must be relatively compact compared to the overall size of the cloud. The larger line widths seen for O VI are consistent with additional sources of turbulence expected for mixing zones in the interface region. Photoionization of O VI is very unlikely in such a region since low gas density and large path lengths are required if the photoionization is due to the extragalactic background.

Most conductive interface models and the turbulent mixing layer models predict O VI column densities of  $\sim 10^{13}~\rm cm^{-2}$  per conduction front and even less for mixing layers (if the mixing is slow - i.e., no shocks). Magnetic fields parallel to conduction fronts inhibit conduction and result in lower O VI column densities. These single-interface column densities are approximately an order of magnitude less than those observed (see Table 1). There are several possible explanations for this. First, there may be small scale macro-structure (clumps) within the clouds that have similar enough velocities that the absorption features from the fragments blend together and cannot be distinguished. The boundary of each fragment would contribute to the total column density, and multiple ( $\gtrsim 10$ ) boundaries would be required to explain the observed values of  $N(O~\rm VI)$ . The O VI profiles are generally quite broad and are consistent with the presence of multiple, blended components. Second, turbulent mixing in eddy layers in the conduction zone increases the likelihood of more efficient mixing and greater O VI columns. The hydrodynamical simulations show that the transition-temperature gas layers where O VI should exist are turbulent in nature (see, e.g., Figure 2 in Quilis & Moore 2001). Third, there may be an external source of heat that increases the depth of the mixing layer. The column densities in mixing layers depend on the temperature of

the post-mixed gas and on the product of the velocity of the hot gas that enters the mixing layers and the fraction of mass deposited by the hot gas in the turbulent flow (Slavin et al. 1993). In the case of a cloud moving through a low density medium, the source of heat could be weak shocks or the ram pressure heating itself.

There are numerous examples of stellar tidal streams in the Galactic halo (see Majewski, Hawley, & Munn 1996; Martínez-Delgado et al. 2001; Newberg et al. 2002). Sources of the high velocity material entering the Galactic corona might include infalling or tidally disturbed galaxies, such as the Sagittarius dwarf (Ibata et al. 2001). Tidal interactions of the fragments and galaxies in the Local Group could drive dynamical instabilities in some of the smaller galaxies and strip interstellar material from gas-rich irregular galaxies (Mayer et al. 2001). Since viscous processes affect the gas but not the stars in interacting systems, tracing the original source of the high velocity gas may prove impossible. However, the fact that no pristine (zero-metallicity) HVCs have yet been identified indicates that some previous metal enrichment inside galaxies has probably occurred (see §7 and Table 9 for some potentially low metallicity clouds that require further study). In the case of Complex C, the low metallicity ( $Z \sim 0.1-0.2$ ) indicates a history different from that of the interstellar material in the Galactic disk.

The column density of O VI within the hot  $(T>10^6\,\mathrm{K})$  gas of the corona or Local Group gas itself is given by  $N(\mathrm{O~VI}) = (\mathrm{O/H})_{\odot}~Z~f_{\mathrm{OVI}}~nL$ , where L is the path length through the absorbing gas. At  $T \geq 10^6\,\mathrm{K}$ ,  $f_{\mathrm{O\,VI}} \leq 3.8 \times 10^{-3}$  (Sutherland & Dopita 1993). For  $n=10^{-5}\,\mathrm{cm}^{-3}$ ,  $N(\mathrm{O~VI})\,[\mathrm{cm}^{-2}] \leq 6.4 \times 10^{10}\,Z~L\,[\mathrm{kpc}]$ . A hot corona with an extent of 1 Mpc and a metallicity Z=0.1 would produce an O VI column density of less than  $10^{13}\,\mathrm{cm}^{-2}$ . Thus, the corona would have an O VI column density significantly less than that of the Milky Way thick disk/halo and would be difficult to detect directly through its O VI absorption. However, if the gas had a higher metallicity (e.g., Z=0.3), and a higher density (e.g.,  $n=10^{-4}\,\mathrm{cm}^{-3}$ ), then the amount of O VI expected would be substantial  $[N(\mathrm{O~VI}) > 3 \times 10^{13}\,\mathrm{cm}^{-2}]$  even if the corona extended only  $\sim 100\,\mathrm{kpc}$ . Such a corona should show X-ray O VII absorption features that may also be detectable (see §9.1). A possible manifestation of the coronal gas might be very broad, shallow absorption wings like those discussed in §8.1. Indeed, preliminary results from several authors (Fang & Sembach 2002; Nicastro et al. 2002) demonstrate that O VII absorption is present near zero velocity along at least two high latitude sight lines, which is consistent with the presence of a large, nearby reservoir of hot gas.

Assuming spherical geometry, a radius  $R \geq 70$  kpc, and density  $n_{\rm H} \sim 10^{-5}$ , the mass of the hot tenuous gas in the corona is  $M \gtrsim 4 \times 10^8 M_{\odot}$ . If the hot corona is a prolate spheroid with an axial ratio a/b = 2:1 and a semi-minor axis of  $b \geq 70$  kpc, then  $M \gtrsim 10^9 M_{\odot}$ . If the hot medium fills the Local Group, the mass would exceed  $10^{11} M_{\odot}$ .

An alternative source for the high velocity O VI may be that the clouds and any associated H I fragments are simply condensations within large remnant Local Group gas structures falling in on the Galaxy (Oort 1970). Cosmological structure formation models predict large numbers of

cooling fragments embedded in dark matter, and some of these structures should be observable in X-ray absorption (e.g., Fang et al. 2002) or in O VI absorption as the gas cools through the  $T=10^5-10^6$  K temperature regime. Estimates of the number density of these structures are consistent with the observed IGM O VI detection rate (Fang & Bryan 2001). This situation is in many ways analogous to the coronal model developed above because only about 30% of the hot gas is detectable in O VI absorption, while the remaining  $\sim 70\%$  is too hot to observe (Davé et al. 2001). However, unlike the coronal model in which the cooler gas may be tidal fragments interacting with a Galactic corona or Local Group medium, in this scenario the O VI-bearing gas and hotter gas share a common evolution within isolated evolving structures with no external baryonic medium required (though dark matter confinement would likely be necessary – see, e.g., Kepner et al. 1999).

Distinguishing between these two models will be difficult, but there are several tests that may yield some additional insight. Metallicity determinations for a substantial number of the high velocity H I and O VI features would help to distinguish between Magellanic debris and lower metallicity ( $Z \lesssim 0.1$ ) gas expected for a cooling gas structure or debris from smaller Local Group galaxies. High-resolution imaging of the  $H\alpha$  emission from the high velocity O VI absorbers would constrain their relationship with the H I and perhaps reveal additional signatures of interactions with an extended Galactic corona (e.g., bow shock structures or turbulently mixed layers of ionized gas between the H I and hot corona). Some high velocity clouds have already been detected in  $H\alpha$  emission at modest spatial resolution: the Magellanic Stream (Weiner & Williams 1996), Complexes A, C, and M (Tufte et al. 1998), and several compact H I HVCs in the  $100^{\circ} < l < 160^{\circ}$ ,  $-60^{\circ} < b < -30^{\circ}$  region of the sky (Tufte et al. 2002). While it is often assumed that all of the H $\alpha$ emission is caused by photoionization, the results of our study indicate that collisional ionization processes should not be ignored. HST observations of C IV and N V associated with the high velocity O VI would help to constrain the ionization properties of the clouds. Finally, imaging of the high velocity gas in O VI and X-ray transitions at sufficient spectral resolution to isolate individual spectral lines would provide much needed insight into the structure of the hot gas and its relationship with cooler material. This is currently difficult with existing instrumentation but should be possible with proposed ultraviolet and X-ray observatories (e.g., SPIDR and Constellation - X).

#### 12. CONCLUSIONS

In this paper we report the results of an extensive FUSE study of high velocity O VI absorption along complete sight lines through the Galactic halo in the directions toward 100 AGNs/QSOs and two distant halo stars. Companion studies describe the observations and data (Wakker et al. 2002) and the results for O VI absorption produced by the thick disk and halo of the Milky Way (Savage et al. 2002b). In this study, the cutoff between high velocity gas and Galactic thick disk/halo absorption was generally near  $|v_{LSR}| \sim 100~{\rm km\,s^{-1}}$ . Our main conclusions regarding the high velocity gas are as follows:

1) We identify 85 individual high velocity O VI features along the 102 sight lines in our sample. A

critical part of this identification process involved detailed consideration of the absorption produced by O VI and other species (primarily  $H_2$ ) in the thick disk and halo of the Galaxy, as well as the absorption produced by low-redshift intergalactic absorption lines of H I and ionized metal species.

- 2) We searched for absorption in a velocity range of  $-1200 < v_{LSR} < +1200 \text{ km s}^{-1}$  around the O VI  $\lambda 1031.926$  line. With few exceptions, the high velocity O VI absorption is confined to  $|v_{LSR}| < 400 \text{ km s}^{-1}$ , indicating that the O VI features observed are either associated with the Milky Way or nearby clouds within the Local Group. The 85 high velocity O VI features have velocity centroids ranging from  $-372 \lesssim \bar{v}_{LSR} \lesssim -90 \text{ km s}^{-1}$  to  $+93 \lesssim \bar{v}_{LSR} \lesssim +385 \text{ km s}^{-1}$ . There are an additional 6 confirmed or very likely (> 90% confidence) detections and 2 tentative detections of O VI between  $v_{LSR} = +500$  and  $+1200 \text{ km s}^{-1}$ ; these very high velocity features probably trace intergalactic gas beyond the Local Group.
- 3) The 85 high velocity O VI features have logarithmic column densities of 13.06 to 14.59, with an average of  $\langle \log N \rangle = 13.95 \pm 0.34$  and a median of 13.97. The average O VI column density is a factor of 2.7 times lower than the typical column density for a sight line through the O VI layer in the thick disk/halo of the Galaxy.
- 4) The line widths of the 85 high velocity O VI features range from  $\sim 16~\rm km\,s^{-1}$  to  $81~\rm km\,s^{-1}$ , with an average of  $\langle b \rangle = 40 \pm 14~\rm km\,s^{-1}$ . The lowest values of b are close to the thermal width expected for O VI at  $T \sim 3 \times 10^5~\rm K$ , while the higher values of b indicate that additional non-thermal broadening mechanisms are common.
- 5) We detect high velocity O VI  $\lambda 1031.926$  absorption with integrated (total) values of  $W_{\lambda} \gtrsim 30$  mÅ at  $\geq 3\sigma$  confidence along 59 of the 102 sight lines surveyed. For the highest quality sub-sample of the dataset, the high velocity detection frequency increases to 22 of 26 sight lines. Forty of the 59 sight lines have high velocity O VI  $\lambda 1031.926$  absorption with  $W_{\lambda} > 100$  mÅ, and 27 have  $W_{\lambda} > 150$  mÅ. Converting these O VI detections into estimates of  $N(\mathrm{H}^+)$  in the hot gas indicates that  $\sim 60\%$  of the sky (and perhaps as much as  $\sim 85\%$ ) is covered by hot ionized hydrogen at a level of  $N(\mathrm{H}^+) \gtrsim 4 \times 10^{16}$  cm<sup>-2</sup> if the high velocity gas has a metallicity similar to that of the Magellanic Stream ( $Z \sim 0.2-0.3$ ), and  $\sim 30\%$  of the sky is covered at a level of  $N(\mathrm{H}^+) \gtrsim 4 \times 10^{17}$  cm<sup>-2</sup>. The covering factor of the hot, high velocity H<sup>+</sup> associated with the O VI is similar to that found for high velocity H I 21 cm emission of warm neutral gas at a comparable column density level.
- 6) High velocity O VI absorption is observed in almost all cases where high velocity H I 21 cm emission is observed. The 6 sight lines for which this is not true may contain small-scale structure within the field of view of the 21 cm observations that is not traced by the O VI absorption measures. In a few cases, ionization effects may also explain the absence of O VI. Three of the six cases are good candidates for follow-up STIS observations to determine if low metallicity may be the reason for the absence of O VI absorption.
- 7) Some of the high velocity O VI is associated with well-known high velocity structures. These include the Magellanic Stream, Complex A, Complex C, the Outer Arm, and several discrete H I

## HVCs.

- 8) Some of the high velocity O VI features have no counterpart in H I 21 cm emission. These include discrete high velocity features as well as broad positive velocity O VI absorption wings that blend with lower velocity absorption features produced by the Galactic thick disk/halo. The discrete features may typify clouds located in the Local Group.
- 9) The broad, high velocity O VI absorption wings are concentrated mainly in the northern Galactic hemisphere (18/22 sight lines) and may trace either tidal debris or thick disk/halo gas that has been accelerated to high velocities by star-formation activity in the Galactic disk. If the latter interpretation is correct, the gas may be related to the northern hemisphere thick disk/halo O VI enhancement observed by Savage et al. (2002b).
- 10) Most of the high velocity O VI features have velocities incompatible with those of Galactic rotation (by definition). The kinematics of the high velocity O VI are not described adequately by models in which the Galactic halo decouples from the underlying disk. There is also no obvious signature of a hot Galactic wind emanating from the Galactic center, but selection effects preclude a definitive statement about its existence.
- 11) The dispersion about the mean of the high velocity O VI centroids decreases when the velocities are converted from the LSR to the GSR and LGSR reference frames. While this reduction is expected if the O VI is associated with gas in a highly extended Galactic corona or in the Local Group, it does not stand alone as sufficient proof of an extragalactic location. The clear separation of the various phenomena producing high velocity O VI in and near the Galaxy will require continuing studies of the distances, kinematics, elemental abundances, and physical states of the different types of O VI HVCs.
- 12) We find it unlikely that many of the observed O VI features are produced by photoionization, even if the gas is irradiated by extragalactic ultraviolet background radiation. Rather, several observational constraints indicate that collisional ionization in hot  $(T \sim 10^5 10^6 \,\mathrm{K})$  gas is likely the dominant ionization process for most of the O VI. The constraints include the amount of O VI observed, the ratios of O VI column densities to those of other highly ionized species (C IV, N V), and the strong correlation between  $N(\mathrm{O~VI})$  and O VI line width.
- 13) Consideration of the possible sources of collisional ionization favors production of some of the high velocity O VI at the turbulent boundaries between cool/warm clouds of gas and a highly-extended, hot  $(T>10^6\,\mathrm{K})$  Galactic corona or Local Group. The corona must have a low density  $(n\lesssim 10^{-4}-10^{-5}~\mathrm{cm}^{-3})$  and be very large  $(R\gtrsim 70~\mathrm{kpc})$  to explain the O VI observed in the Magellanic Stream and other putative Local Group clouds. This corona is much more extensive than the Galactic thick disk/halo region considered in previous hot gas investigations.
- 14) The existence of a hot, highly extended Galactic corona or Local Group medium and the prevalence of high velocity O VI are consistent with predictions that there should be a considerable amount of hot gas left over from the formation of the Local Group. Descriptions of galaxy evolution

will need to account for highly ionized gas of the type observed in this study, and future X-ray studies of hot gas in the Local Group will need to consider carefully the relationship of the X-ray absorption/emission to the complex high velocity absorption observed in O VI.

This work is based on data obtained for the Guaranteed Time Team by the NASA-CNES-CSA FUSE mission operated by the Johns Hopkins University. We thank Chris Howk for assistance with implementation of the CLOUDY ionization code, and members of the FUSE O VI working group for encouragement and helpful discussions. This research has made use of the NASA/IPAC Extragalactic Database (NED), which is operated by the Jet Propulsion Laboratory, California Institute of Technology, under contract with the National Aeronautics and Space Administration. KRS acknowledges financial support through NASA contract NAS5-32985 and Long Term Space Astrophysics grant NAG5-3485. BPW acknowledges financial support through NASA grants NAG5-8967, NAG5-9024, and NAG5-9179.

### REFERENCES

Anders, E., & Grevesse, N. 1989, Geochim. Cosmochim. Acta., 53, 197

Arnal, E.M., Bajaja, E., Larrarte, J.J., Morras, R., & Poppel, W.G.L. 2000, A&AS, 142, 35

Berkhuijsen, E., Haslam, C.G.T., & Salter, C.J. 1971, A&A, 14, 252

Bland-Hawthorn, J., & Maloney, P.R. 1999, ApJ, 510, L33 [Erratum: 2001, ApJ, 550, L231]

Blitz, L., & Robishaw, T. 2000, ApJ, 541, 675

Blitz, L., Spergel, D.N., Teuben, P., Hartmann, D., & Burton, W.B. 1999, ApJ, 514, 818

Borkowski, K.J., Balbus, S.A., & Fristrom, C.C. 1990, ApJ, 355, 501

Bowen, D.V., & Blades, J.C. 1993, ApJ, 403, L55

Bowen, D.V., Blades, J.C., & Pettini, M. 1995, ApJ, 448, 662

Bregman, J.N. 1980, ApJ, 236, 577

Bregman, J.N., & Harrington, J.P. 1986, ApJ, 309, 833

Braun, R., & Burton, W.B. 1999, A&A, 341, 437

Braun, R., & Burton, W.B. 2000, A&A, 354, 853

Breitschwerdt, D., & Komossa, S. 2000, Ap&SS, 272, 3

Brüns, C., Kerp, J., Kalberla, P.M.W., & Mebold, U. 2000, A&A, 357, 120

Brüns, C., Kerp, J. & Pagels, A. 2001, ApJ, 370, L26

Burton, W.B., Braun, R., & Chengalur, J.N. 2001, A&A, 369, 616

Cardelli, J.A., Clayton, G.C., & Mathis, J.S. 1989, ApJ, 345, 245

Cen, R., & Ostriker, J.P. 1999, ApJ, 514, 1

Charlton, J.C., Churchill, C.W., & Rigby, J.R. 2000, ApJ, 544, 702

Clemens, D.P. 1985, ApJ, 295, 422

Danforth, C.W., Howk, J.C., Fullerton, A.W., Blair, W.P., & Sembach, K.R. 2002, ApJS, 139, 81

Danly, L., Albert, C.E., & Kuntz, K.D. 1993, ApJ, 416, L29

Davé, R., Cen, R., Ostriker, J.P., Bryan, G.L., Hernquist, L., Katz, N., Weinberg, D.H., Norman, M.L., & O'Shea, B. 2001, ApJ, 552, 473

Davé, R., Hernquist, L., Katz, N., & Weinberg, D.H. 1999, ApJ, 511, 521

de Boer, K.S., Braun, J.M., Vallenari, A., & Mebold, U. 1998, A&A, 329, L49

Donahue, M., Aldering, G., & Stocke, J.T. 1995, ApJ, 450, L45

Dupree, A.K., & Raymond, J.C. 1983, ApJ, 275, L71

Edgar, R.J., & Chevalier, R.A. 1986, ApJ, 310, L27

Fang, T.T., & Bryan, G.L. 2001, ApJ, 561, L31

- Fang, T.T., Marshall, H.L., Lee, J.C., Davis, D.S., & Canizares, C.R. 2002, ApJ, 572, L127
- Fang, T.T., & Sembach, K.R. 2002, in preparation
- Federman, S.R., Sheffer, Y., Lambert, D.L., & Gilliland, R.L. 1993, ApJ, 413, L51
- Ferland, G.J. 1996, Hazy, a Brief Introduction to CLOUDY 90, University of Kentucky Physics Department Internal Report
- Fox, A.J., et al. 2002, in preparation
- Friedman, S.D., et al. 2000, ApJ, 538, L39
- Gardiner, L.T., 1999, in "The Stromlo Workshop on High Velocity Clouds", ASP Conference Series 166, eds. B.K. Gibson & M.E. Putman, (San Francisco: ASP), 292
- Gardiner, L.T., & Noguchi, M. 1996, MNRAS, 278, 191
- Gibson, B.K., Giroux, M.L., Penton, S.V., Putman, M.E., Stocke, J.T., & Shull, J.M. 2000, AJ, 120, 1830
- Gibson, B.K., Giroux, M.L., Penton, S.V., Stocke, J.T., Shull, J.M., & Tumlinson, J. 2001a, AJ, 122, 3280
- Gibson, B.K., Giroux, M.L., Stocke, J.T., & Shull, J.M. 2001b, in "Gas & Galaxy Evolution", ASP Conference Series 240, eds. J.E. Hibbard, M. Rupen, & J.H. van Gorkom (San Francisco: ASP), 493
- Haardt, F., & Madau, P. 1996, ApJ, 461, 20
- Hartmann, D., & Burton, W.B. 1997, Atlas of Galactic Neutral Hydrogen (Cambridge: Cambridge Univ. Press)
- Haud, U. 1992, MNRAS, 257, 70
- Heckman, T.M. 2002, in "Extragalactic Gas at Low Redshift", ASP Conference Series 254, eds. J.S. Mulchaey & J.T. Stocke, (San Francisco: ASP), 292
- Heckman, T.M., Norman, C., Strickland, D.K., & Sembach, K.R. 2002, ApJ, in press [astro-ph/0205556]
- Heckman, T.M., Sembach, K.R., Meurer, G.R., Strickland, D.K., Martin, C.L., Calzetti, D., & Leitherer, C. 2001, ApJ, 554, 1021
- Hirashita, H., Kamaya, H., & Mineshige, S. 1997, MNRAS, 290, L33
- Holweger, H. 2001, in "Solar and Galactic Composition", AIP Conference Proceeding 598, ed. R.F. Wimmer-Schweingruber, (New York: American Institute of Physics), 23
- Hoopes, C.G., Sembach, K.R., Howk, J.C., & Blair, W.P. 2001, ApJ, 558, L35
- Hoopes, C.G., Sembach, K.R., Howk, J.C., Savage, B.D., & Fullerton, A.W. 2002, ApJ, 569, 233
- Houck, J.C., & Bregman, J.N. 1990, ApJ, 352, 506
- Howk, J.C., Savage, B.D., Sembach, K.R., & Hoopes, C.G. 2002a, ApJ, 572, 264

Howk, J.C., Sembach, K.R., Savage, B.D., Massa, D., Friedman, S., & Fullerton, A.W. 2002b, ApJ, 569, 214

Hulsbosch, A.N.M., & Wakker, B.P. 1998, A&AS, 75, 191

Ibata, R. Lewis, G.F., Irwin, M., Totten, E., & Quinn, T. 2001, ApJ, 551, 294

Irwin, M.J., Demers, S., & Kunkel, W.E. 1990, AJ, 99, 191

Iwan, D. 1980, ApJ, 239, 316

Jenkins, E.B. 1978a, ApJ, 219, 845

Jenkins, E.B. 1978b, ApJ, 220, 107

Jenkins, E.B., Bowen, D.V., & Sembach, K.R. 2002, to appear in the Proceedings of the XVII<sup>th</sup> IAP Colloquium: "Gaseous Matter in Galactic and Intergalactic Space"

Karachentsev, I.D., & Makarov, D.I. 1996, AJ, 111, 794

Kepner, J., Tripp, T.M., Abel, T., & Spergel, D. 1999, AJ, 117, 2603

Kepner, M.E. 1970, A&A, 5, 44

Lehner, N. 2002, ApJ, in press [astro-ph/0206250]

Lockman, F.J. 1984, ApJ, 238, 90

Lockman, F.J., Murphy, E.M., Petty-Powell, S., & Urick, V. 2002, ApJS, in press [astro-ph/0201039]

Lu, L., Savage, B.D., & Sembach, K.R. 1994, ApJ, 426, 563

Lu, L., Savage, B.D., Sembach, K.R, Wakker, B.P., Sargent, W.L.W., Oosterloo, T.A. 1998, AJ, 115, 162

Madau, P. 1992, ApJ, 389, L1

Majewski, S.R., Hawley, S.L., & Munn, J.A. 1996, in "Formation of the Galactic Halo...Inside and Out", ASP Conference Series 92, eds. H. Morrison & A. Sarajedini, (San Francisco: ASP), 119

Martínez-Delgado, D., Aparicio, A., Gómez-Flechoso, M.A., & Carrera, R. 2001, ApJ, 549, L199

Martin, C.L. 2002, in "Extragalactic Gas at Low Redshift", ASP Conference Series 254, eds. J.S. Mulchaey & J.T. Stocke, (San Francisco: ASP), 305

Mayer, L., Governato, F., Colpi, M., Moore, B., Quinn, T., Wadsley, J., Stadel, J., & Lake, G. 2001, ApJ, 547, L123

Mihalas, D. & Binney, J. 1981, Galactic Astronomy, (2nd ed; San Francisco: Freeman), Ch. 6

Miller, W.W., & Cox, D.P. 1993, ApJ, 417, 579

Moore, B., & Davis, M. 1994, MNRAS, 270, 209

Moos, H.W., et al. 2000, ApJ, 538, L1

Moos, H.W., et al. 2002, ApJS, 140, 3

Morras, R., Bajaja, E., Arnal, E.M., & Pöppel, W.G.L. 2000, A&AS, 142, 25

Morton, D.C. 1991, ApJS, 77, 119

Murali, C. 2001, ApJ, 529, L81

Murphy, E.M., Lockman, F.J., Laor, A., & Elvis, M. 1996, ApJS, 105, 369

Murphy, E.M., et al. 2000, ApJ, 538, L35

Newberg, H.J., et al. 2002, ApJ, 569, 245

Nicastro, F., et al. 2002, ApJ, 573, 157

Norman, C., & Ikeuchi, S. 1989, ApJ, 345, 372

Oegerle, W.R., et al. 2000, ApJ, 538, L23

Oort, J.H. 1970, A&A, 7, 381

Putman, M.E. 2000, PASA, 17, 1

Putman, M.E., et al. 2002, AJ, 123, 873

Putman, M.E., et al. 1998, Nature, 394, 752

Quilis, V., & Moore, B. 2001, ApJ, 555, L95

Rasmussen, J., & Pedersen, K. 2001, ApJ, 559, 892

Reynolds, R.J. 1993, in "Back to the Galaxy", eds. S. Holt & F. Verter (New York: American Institute of Physics), 156

Richter, P., Sembach, K.R., Wakker, B.P., Savage, B.D., Tripp, T.M., Murphy, E.M., Kalberla, P.M.W., & Jenkins, E.B. 2001, ApJ, 559, 318

Richter, P. Wakker, B.P., Savage, B.D., & Sembach, K.R. 2002, in preparation

Ryans, R.S.I., Keenan, F.P., Sembach, K.R., & Davies, R.D. 1997, MNRAS, 289, 986

Sahnow, D.S., et al. 2000a, ApJ, 538, L7

Sahnow, D.S., et al. 2000b, SPIE, 4013, 334

Savage, B.D., Massa, D., & Sembach, K.R. 1990, ApJ, 355, 114

Savage, B.D., & Sembach, K.R. 1996, ARA&A, 34, 279

Savage, B.D., & Sembach, K.R. 1991, ApJ, 379, 245

Savage, B.D., et al. 2000, ApJ, 538, L27

Savage, B.D., Sembach, K.R., & Lu, L. 1997, AJ, 113, 2158

Savage, B.D., Sembach, K.R., Tripp, T.M., & Richter, P. 2002a, ApJ, 564, 631

Savage, B.D., Sembach, K.R., Wakker, B.P., Richter, P., Meade, M., Jenkins, E.B., Shull, J.M., Moos, H.W. & Sonneborn, G. 2002b, ApJS, submitted

Sembach, K.R. 1999, in "The Stromlo Workshop on High Velocity Clouds", ASP Conference Series 166, eds. B.K. Gibson & M.E. Putman, (San Francisco: ASP), 243

Sembach, K.R. 2002, in "Extragalactic Gas at Low Redshift", ASP Conference Series 254, eds. J.S. Mulchaey & J.T. Stocke, (San Francisco: ASP), 283

Sembach, K.R., Gibson, B.K., Fenner, Y., & Putman, M.E. 2002, ApJ, 572, 178

Sembach, K.R., Howk, J.C., Savage, B.D., & Shull, J.M., 2001a, ApJ, 561, 573 [Erratum: 2002, AJ, 123, 3488]

Sembach, K.R., Howk, J.C., Savage, B.D., Shull, J.M., & Oegerle, W.R. 2001b, ApJ, 561, 573

Sembach, K.R., & Savage, B.D. 1992, ApJS, 83, 147

Sembach, K.R., Savage, B.D., & Lu, L. 1995a, ApJ, 439, 672

Sembach, K.R., Savage, B.D., Lu, L., & Murphy, E.M. 1995b, ApJ, 451, 616

Sembach, K.R., Savage, B.D., Lu, L., & Murphy, E.M. 1999, ApJ, 515, 108

Sembach, K.R., Savage, B.D., & Massa, D. 1991, ApJ, 372, 81

Sembach, K.R., et al. 2000, ApJ, 538, L31

Sembach, K.R., Savage, B.D., & Tripp, T.M. 1997, ApJ, 420, 216

Shapiro, P.R., & Field, G.B. 1976, ApJ, 205, 762

Shapiro, P.R., & Moore, R.T. 1976, ApJ, 207, 460

Shull, J.M., Roberts, D., Giroux, M., Penton, S.V., & Fardal, M.A. 1999, AJ, 118, 1450

Simon, J.D., & Blitz, L. 2002, ApJ, submitted [astro-ph/0204042]

Slavin, J.D., & Cox, D.P. 1992, ApJ, 392, 131

Slavin, J.D., Shull, J.M., & Begelman, M.C. 1993, ApJ, 407, 83

Snowden, S.L., et al. 1995, ApJ, 454, 643

Snowden, S.L., et al. 1997, ApJ, 485, 125

Spitzer, L. 1996, ApJ, 458, L29

Stanimirovic, S., Dickey, J.M., Krčo, M., & Brooks, A.M. 2002, ApJ, in press [astro-ph/0205327]

Sterling, N.C., Savage, B.D., Richter, P., Fabian, D., & Sembach, K.R. 2002, ApJ, 567, 354

Sutherland, R.S., & Dopita, M.A. 1993, ApJS, 88, 253

Tripp, T.M., & Savage, B.D. 2000, ApJ, 542, 42

Tripp, T.M., Savage, B.D., & Jenkins, E.B. 2000, ApJ, 534, L1

Tripp, T.M., et al. 2002, in preparation

Tufte, S.L., Reynolds, R.J., & Haffner, L.M. 1998, ApJ, 504, 773

Tufte, S.L., Wilson, J.D., Madsen, G.J., Haffner, L.M., & Reynolds, R.J. 2002, ApJ, in press [astro-ph/0206198]

van Woerden, H., Peletier, R.F., Schwarz, U.J., Wakker, B.P., & Kalberla, P.M.W. 1999a, in "The Stromlo Workshop on High Velocity Clouds", ASP Conference Series 166, eds. B.K. Gibson & M.E. Putman, (San Francisco: ASP), 1

van Woerden, H., Schwarz, U.J., Peletier, R.F., Wakker, B.P., & Kalberla, P.M.W. 1999b, Nature, 400, 138

Wakker, B.P. 2001, ApJS, 136, 463

Wakker, B.P., et al. 1999, Nature, 402, 388

Wakker, B.P., Kalberla, P.M.W., van Woerden, H., de Boer, K.S., & Putman, M.E. 2001, ApJS, 136, 537

Wakker, B.P., & van Woerden, H. 1991, A&A, 250, 509

Wakker, B.P., & van Woerden, H. 1997, ARA&A, 35, 217

Wakker, B.P., Savage, B.D., Sembach, K.R. Richter, P., Meade, M., et al. 2002, ApJS, submitted

Wannier, P.G., & Andersson, B.-G. 2002, ApJ, submitted

Weiner, B.J., & Williams, T.B. 1996, AJ, 111, 1156

Zirakashvili, V.N., Breitschwerdt, D., Ptuskin, V.S., & Voelk, H.J. 1996, A&A, 311, 113

Zsargo, J., Sembach, K.R., Howk, J.C, & Savage, B.D. 2002,

Zwaan, M.A., & Briggs, F.H. 2000, ApJ, 530, L61 in preparation

This preprint was prepared with the AAS LATEX macros v5.0.

## FIGURE CAPTIONS

Unfortunately, all figures are in PNG format due to size restrictions imposed by astro-ph. These figures look "best" displayed on a computer screeen or printed as gray-scale images. Higher quality (postscript) versions are available upon request.

Fig. 1.— (See accompanying PNG file.) FUSE LiF1A observations of the 1015–1040 Å spectral region of three AGN/QSOs in the high velocity O VI survey. The data have a velocity resolution of  $\sim 20~{\rm km\,s^{-1}}$  (FWHM) and are binned to  $\sim 10~{\rm km\,s^{-1}}$  ( $\sim 0.033~{\rm Å}$ ) samples. Prominent interstellar lines, including the two lines of the O VI doublet at 1031.926 Å and 1037.617 Å, are identified above each spectrum at their rest (laboratory) wavelengths. The wavelengths of strong molecular hydrogen lines in the J=0-4 rotational levels are indicated in the top panel; the H<sub>2</sub> lines decrease in strength from the top to bottom panels. Additional H I and metal lines from intervening intergalactic clouds are present in the middle and bottom panels. Crossed circles mark the locations of terrestrial airglow lines of H I and O I. High velocity O VI  $\lambda 1031.926$  absorption is present along all three sight lines.

Fig. 2.— (See accompanying PNG file.) Upper panels: Normalized intensity profiles for the O VI  $\lambda\lambda 1031.926, 1037.617$  lines toward Mrk 509, ESO 572-G34, and PG 1116+215. The O VI  $\lambda 1031.926$  line is shown at the top of each panel, together with a model of the H<sub>2</sub> (6–0) P(3)  $\lambda 1031.191$  and (6–0) R(4)  $\lambda 1032.349$  absorption features (thin solid line). The O VI  $\lambda 1037.617$  line is shown below the 1031.926 Å line, together with horizontal bars indicating the integration ranges of the high velocity absorption. The high velocity portions of the  $\lambda 1037.617$  absorption are sometimes blended with other Galactic ISM features [C II  $\lambda 1036.337$ , C II\*  $\lambda 1037.012$ , H<sub>2</sub> (5–0) R(1)  $\lambda 1037.149$  and P(1) 1038.157]. Bottom panels: Apparent column density profiles for the O VI  $\lambda 1031.926$  absorption (heavy line) and  $\lambda 1037.617$  absorption (light line). The values of  $N_a(v)$  for the two lines agree well when a direct comparison is possible, indicating that there are no unresolved saturated structures within the lines at these velocities.

Fig. 3.— (See accompanying PNG files.) (*Top panel:*) All-sky Hammer-Aitoff projection of the 102 sight lines in the *FUSE* O VI survey. In this projection, the Galactic anti-center is at the center of the figure, and Galactic longitude increases to the left. The locations and names of the 100 QSOs/AGNs and 2 halo stars are indicated. In a few cases, the names have been abbreviated for clarity. (*Bottom panel:*) High velocity O VI identifications. The "type" of high velocity gas (if any) observed along each sight line is coded according to the categories described in Table 3. For some sight lines, multiple high velocity features are present. Plus symbols indicate the positions of the high velocity gas non-detections listed in Table 2.

- Fig. 4.— (See accompanying PNG file.) Logarithmic O VI column densities [log N(O VI) (cm<sup>-2</sup>)] for the Milky Way thick disk/halo (dashed line) and high velocity (solid line) absorption features listed in Table 1. The bin size for these distributions is 0.10 dex.
- Fig. 5.— (See accompanying PNG file.) (Top panel:) A comparison of the O VI column densities of the thick disk/halo and high velocity absorption along the 59 sight lines where high velocity O VI absorption is observed. Open circles indicate sight lines with  $b < 0^{\circ}$ ; filled circles indicate sight lines with  $b > 0^{\circ}$ . A modest anti-correlation of the two quantities exists (dashed line). (Bottom panel:) A comparison of the high velocity O VI column densities and sight-line-averaged ROSAT 0.25 keV X-ray intensities (I(X), in units of  $10^{-6}$  cnt s<sup>-1</sup> arcmin<sup>-2</sup>). A modest anti-correlation of the two quantities exists (dashed line).
- Fig. 6.— (See accompanying PNG files.) All-sky Hammer-Aitoff projections of the high velocity O VI column densities listed in Table 1. In the top panel, the logarithmic column density is coded according to symbol size (see legend), with the symbol split in in half if two features are present. In the bottom panel, the column density is color coded. Detections are plotted as colored circles that are 12° in radius. When two features were detected within 12° of each other (either along the same sight line or along adjoining sight lines), the shaded area size is adjusted accordingly. The mottled appearance of some regions indicates lower reliability measurements. Null detections are indicated as either downward-pointing triangles with a size proportional to the upper limit on the column density (top panel) or as small (2.5° radius) color-coded regions indicating the upper limit (bottom panel).
- Fig. 7.— (See accompanying PNG file.) Distributions of high velocity O VI profile centroids in the Local Standard of Rest, Galactic Standard of Rest, and the Local Group Standard of Rest reference frames for the 85 features listed in Table 1. The distributions for the subsample of 50 LG, EPn, and MSe features considered in §§8.2 and 10.4 are shown as shaded regions. By definition, the absence of features at  $-100 \lesssim v_{LSR} \lesssim 100 \text{ km s}^{-1}$  in the top panel occurs because of blending with the Galactic thick disk/halo O VI distribution. The bin size for these distributions is 20 km s<sup>-1</sup>. The dashed Gaussian profiles are fits to the distributions containing all the high velocity features; in the top panel, the fit is performed only for  $|v_{LSR}| \geq 100 \text{ km s}^{-1}$ . The ensemble velocity centroids ( $\langle \bar{v} \rangle$ ) and widths ( $\sigma$  and FWHM) are given in the upper left corner for each distribution (see also Table 6).
- Fig. 8.— (See accompanying PNG file.) High velocity O VI centroids in the Local Standard of Rest reference frame. In the top panel, filled circles denote sight lines with  $b > 0^{\circ}$ , and open circles denote sight lines with  $b < 0^{\circ}$ . In the bottom panel, filled circles denote sight lines with  $180^{\circ} < l < 360^{\circ}$ , and open circles denote sight lines with  $0^{\circ} < l < 180^{\circ}$ . The vertical bar on each point is the velocity width ( $\pm$ b) measured for each feature. By definition, few points fall in the region with  $-100 \lesssim \bar{v}_{LSR} \lesssim 100 \text{ km s}^{-1}$ .

Fig. 9.— (See accompanying PNG file.) High velocity O VI centroids in the Galactic Standard of Rest reference frame. Filled circles denote sight lines with  $b > 0^{\circ}$ , and open circles denote sight lines with  $b < 0^{\circ}$ . The vertical bar on each point is the velocity width (±b) measured for each feature. The dashed curves bound the region of the plot that would be occupied by gas in the Galactic disk ( $|b| \le 20^{\circ}$ ) with  $|\bar{v}_{LSR}| \le 100 \text{ km s}^{-1}$ ; by definition of the sample, few points fall in this region.

Fig. 10.— (See accompanying PNG files.) All-sky Hammer-Aitoff projections of the O VI velocities in the LSR and GSR reference frames. These maps include features listed in Table 1 and do not include gas at velocities attributed to the thick disk/halo of the Galaxy. The velocities of the O VI features are color coded and displayed as filled regions of radius 12° for each direction where high velocity gas is detected. When two features were detected within 12° of each other (either along the same sight line or along adjoining sight lines), the shaded area size is adjusted accordingly. Points with no colors indicate null detections of high velocity O VI.

Fig. 11.— (See accompanying PNG files.) (a) Hammer-Aitoff projection of the high velocity H I sky based on 21 cm emission measurements (adapted from Wakker et al. 2002). The H I data has a spatial resolution of approximately 36' and is representative of gas with  $N({\rm H~I}) > 2 \times 10^{18}$  cm<sup>-2</sup>. Data for  $|b| < 20^{\circ}$  have been omitted for clarity. The positions of the high velocity O VI features listed in Table 1 are denoted by the large circles, with the fill color indicating velocity on the same color scale used for the H I emission. If more than one high velocity O VI feature is present, the circle is split and the velocities are color-coded in each section of the circle. Open circles indicate null detections (Table 2). "X" marks indicate the locations of the two stellar sight lines in the sample. (b) Azimuthal equal-area projection of the data shown in Figure 11a, looking up toward the north Galactic pole. (c) Azimuthal equal-area projection of the data shown in Figure 11a, looking down toward the south Galactic pole.

Fig. 12.— (See accompanying PNG file.) O VI profile widths for the Milky Way thick disk/halo (dashed line) and high velocity (solid line) absorption features. These observed widths have not been corrected for the small amount of instrumental line broadening; this broadening ( $b_{inst} \sim 12 - 15 \text{ km s}^{-1}$ ) is important only for the narrowest lines observed. The bin size for these distributions is  $5 \text{ km s}^{-1}$ . The arrow indicates the thermal width ( $b = 17.6 \text{ km s}^{-1}$ ) for a single component at  $T = 3 \times 10^5 \text{ K}$ .

- Fig. 13.— (See accompanying PNG files.) A Leiden-Dwingeloo survey grey-scale map of the high velocity H I 21 cm emission in the region of sky near Complex C. The contours denote an H I column density of  $5 \times 10^{18}$  cm<sup>-2</sup>. The top panel shows the emission over the velocity range  $-200 \le v_{\rm LSR} \le -150~{\rm km\,s^{-1}}$ . The bottom panel shows the emission over the velocity range  $-150 \le v_{\rm LSR} \le -100~{\rm km\,s^{-1}}$ . The FUSE sight lines are marked in red. Additional features in this region of the sky (Complex A, IV Arch, Complex K) are also indicated in the lower panel.
- Fig. 14.— (See accompanying PNG file.) H I 21 cm emission, O VI  $\lambda 1031.926$ , and C II  $\lambda 1036.337$  absorption profiles for nine sight lines in the general direction of Complex C. The NRAO 140-foot H I spectra have a beam size of 21' (FWHM). The solid line overplotted on the O VI profile is a model of the interstellar H<sub>2</sub> absorption in the (6–0) P(3) and R(4) lines. The horizontal bar below the O VI profile shows the integration range for the high velocity O VI. C II\*  $\lambda 1037.018$  absorption is seen at a velocity of  $\sim 197~{\rm km\,s^{-1}}$  relative to the C II line.
- Fig. 15.— (See accompanying PNG file.) H I 21 cm emission, O VI  $\lambda 1031.926$ , and C II  $\lambda 1036.337$  absorption profiles for six directions identified in Table 1 as Magellanic Stream (MS/MSe) sight lines. The top set of panels shows sight lines containing high negative velocity gas, and the bottom set of panels shows sight lines containing high positive velocity gas. The H I spectra come from a variety of sources (Green Bank/NRAO, Parkes, Villa-Elisa). The values of  $T_b$  have been scaled in the plots by the factors indicated to show the HVC emission. The solid line overplotted on the O VI profile is a model of the interstellar H<sub>2</sub> absorption in the (6–0) P(3) and R(4) lines. The horizontal bar above the C II profile shows the integration range for the high velocity gas. C II\*  $\lambda 1037.018$  absorption is seen at a velocity of  $\sim 197$  km s<sup>-1</sup> relative to the C II line.
- Fig. 16.— (See accompanying PNG file.) Normalized intensity versus LSR velocity for 22 objects in our sample with high positive velocity O VI absorption wings. These components are identified in Table 1 with a dagger (†) symbol attached to the feature identification. Identifications of all high velocity O VI features are provided above each spectrum. In many cases, the absorption wings join smoothly with the low velocity absorption produced by the Galactic thick disk/halo. The smooth solid curves overplotted on some of the spectra are models of the  $H_2$  (6–0) P(3) and R(4) absorption along the sight lines. The IGM absorption feature in the 3C 273 spectrum is H I Ly $\beta$  at a redshift  $z \approx 0.0053$ .

- Fig. 17.— (See accompanying PNG file.) All-sky distribution of 22 sight lines containing high positive velocity O VI absorption wings. This map includes those sight lines for which a dagger (†) symbol is attached to the high velocity feature identifications in Table 1. The symbol size indicates the O VI column density of the absorption feature. Note that most of these sight lines are located in the northern Galactic hemisphere.
- Fig. 18.— (See accompanying PNG file.) Ratios of N(O VI)/N(C IV) and N(O VI)/N(N V) as a function of temperature (in K) under conditions of collisional ionization equilibrium (Sutherland & Dopita 1993). The calculations assume intrinsic solar abundance ratios, (O/C) = 1.4 and (O/N) = 6.4 (Holweger 2001), and identical gas-phase depletions onto dust grains,  $\delta(C) = \delta(N) = \delta(O)$ . Differential depletion of these elements onto dust grains will raise or lower the resulting curves by less than  $\sim 0.3$  dex since none of these elements is strongly depleted from the gas-phase in diffuse cloud environments (see Savage & Sembach 1996).
- Fig. 19.— (See accompanying PNG file.) Ionization fractions of O VI, N V, C IV, and H I versus ionization parameter,  $U = \langle n_{\gamma}/n_{H} \rangle$ , and gas density,  $n_{H}$ , for uniform dust-free gas clouds with 1/3 solar metallicity subjected to the extragalactic ionizing background at z = 0. Models for two values of total H I column density are plotted. The models assume an incident AGN/QSO spectrum with an intensity  $J_{\nu_0} = 10^{-23}$  erg cm<sup>-2</sup> s<sup>-1</sup> Hz<sup>-1</sup> sr<sup>-1</sup> at the Lyman limit. The curves shown do not vary strongly as a function of metallicity for Z = 0.01 1.0.
- Fig. 20.— (See accompanying PNG file.) O VI column density as a function of ionization parameter and gas density for extragalactic clouds similar to those considered in Figure 19. N(O VI) is shown for four values of the assumed H I column density. N(O VI) scales roughly linearly with metallicity for the range of N(H I) values shown. At a given ionization parameter (or density), the cloud size, D, increases with the H I column density; values of D (in kpc) are given immediately above several of the points.
- Fig. 21.— (See accompanying PNG file.) Column density ratios  $N(O\ VI)/N(C\ IV)$  and  $N(O\ VI)/N(N\ V)$  as a function of ionization parameter and gas density for the extragalactic cloud considered in Figure 19, assuming solar relative abundances for C, N, and O. Models for two values of total H I column density are plotted. The ratios do not change substantially for metallicities in the range 0.01–1.0 solar.

Fig. 22.— (See accompanying PNG file.) O VI column density  $[N({\rm O~VI})~{\rm cm}^{-2}]$  versus line width  $[{\rm b~(km\,s}^{-1})}]$  for a variety of O VI absorption systems. Data points include absorption observed by FUSE in the Galactic halo (Savage et al. 2002), high velocity clouds (this paper), the SMC (Hoopes et al. 2002), and the LMC (Howk et al. 2002). Data points for absorption in the Galactic disk are from the Copernicus O VI survey (Jenkins 1978a, 1978b). The straight diagonal line indicates the approximate detection limit for FUSE data if  $W_{1032}=30~{\rm m~\mathring{A}}$ . Note the good correlation between N and b. The thermal widths of single components at various temperatures are indicated at the top of the figure.

Fig. 23.— (See accompanying PNG file.) Deviations of the O VI velocities from those predicted by the corotating halo model described in the text versus Galactic longitude (upper panel) and latitude (lower panel). The deviation velocity,  $\Delta v = \bar{v} - v_{\rm pred}$ , is defined as the difference between the measured velocity centroid of the high velocity O VI feature and the velocity extremum of the  $\lambda 1031.926$  absorption expected for a smooth, corotating, exponentially-stratified O VI gas layer with a scale height of 2.3 kpc, and an intrinsic gas velocity dispersion (b =  $\sqrt{2}\sigma$ ) of 60 km s<sup>-1</sup>. The different symbols denote the various high velocity feature designations according to the code given to the right of the lower panel.

Fig. 24.— (See accompanying PNG file.) Same as Figure 23, except for the non-corotating gas layer described in the text.

Table 1. High Velocity O VI Detections

Name	<i>l</i> (°)	b (°)	Qa	${ m ID^b}$	$v_{min}$ ( km	$s^{-1}$	$\bar{v}$ ( km s <sup>-1</sup> )	$b^{c}$ $(km s^{-1})$	$\log N \pm \sigma_{sc} \pm \sigma_{sys}$	$\frac{W_{\lambda}}{\sigma_W}$
PKS 2155-304	17.73	-52.25	4	LG	-180	-85	-129	35±3	$13.80 \pm 0.03 \pm 0.11$	17.5
				$_{ m LG}$	-280	-180	-232	$42 \pm 4$	$13.57 \pm 0.05 \pm 0.14$	8.6
$\mathrm{Mrk}509$	35.97	-29.86	4	$_{ m LG}$	-345	-180	-247	$(57\pm4)$	$14.24 \pm 0.02 \pm 0.08$	25.0
				$_{ m LG}$	-180	-100	-143	$((31\pm3))$	$13.76 \pm 0.04 \pm 0.15$	12.6
				$\mathrm{Oth}^{\dagger}$	115	200	152	$((34\pm4))$	$13.55 \pm 0.06 \pm 0.22$	7.0
MRC2251-178	46.20	-61.33	3	$_{ m LG}$	-340	-180	-258	65±4	$13.91 \pm 0.11 \pm 0.05$	3.7
				$_{ m LG}$	-145	-65	-95	$31\pm4$	$14.06 \pm 0.06 \pm 0.10$	8.4
PHL 1811	47.46	-44.81	3	$_{ m LG}$	-360	-295	-322	$21\pm3$	$13.85 \pm 0.09 \pm 0.09$	5.2
				$_{ m LG}$	-200	-65	-142	$(42\pm 3)$	$14.38 \pm 0.04 \pm 0.08$	13.0
${ m Mrk}506$	54.18	31.50	1	$\mathbf{C}$	-180	-100	-144	$(33\pm 4)$	$14.05 \pm 0.11 \pm 0.14$	4.5
$\mathrm{Mrk}478$	59.24	65.03	3	Oth	340	435	385	$35\pm 4$	$13.83 \pm 0.10 \pm 0.05$	4.4
3C382.0	61.31	17.45	1	OA	-130	-50	-90	$((30\pm3))$	$14.14 \pm 0.10 \pm 0.09$	5.1
$\mathrm{Mrk}501$	63.60	38.86	2	$\mathbf{C}$	-150	-100	-122	$((22\pm3))$	$13.81 \pm 0.11 \pm 0.19$	4.3
$\mathrm{Mrk}1513$	63.67	-29.07	3	MSe	-390	-220	-293	49±4	$14.29 \pm 0.05 \pm 0.04$	9.0
${ m Mrk}926$	64.09	-58.76	1	LG	-220	-65	-125	$(60\pm 5)$	$14.44 {\pm} 0.12 {\pm} 0.05$	4.5
				MSe	-395	-220	-295	$(57\pm5)$	$14.41 {\pm} 0.12 {\pm} 0.04$	3.8
$\mathrm{Mrk}304$	75.99	-34.22	3	MSe	-355	-240	-304	$40 \pm 3$	$14.47 {\pm} 0.06 {\pm} 0.04$	11.4
NGC7469	83.10	-45.47	4	MS	-370	-235	-304	$(54 \pm 5)$	$14.18 \pm 0.04 \pm 0.11$	11.9
				LG	-235	-120	-185	$((43\pm 4))$	$14.22 {\pm} 0.03 {\pm} 0.16$	14.2
PG 1626 + 554	84.51	42.19	2	$\mathrm{Oth}^{\dagger}$	85	210	132	$(48\pm 4)$	$14.08 \pm 0.11 \pm 0.07$	4.1
				$\mathbf{C}$	-260	-65	-152	$((81\pm6))$	$14.35 \pm 0.08 \pm 0.05$	5.9
NGC7714	88.22	-55.56	2	MS	-310	-230	-259	$(26\pm 3)$	$14.13 \pm 0.09 \pm 0.09$	5.6
$\mathrm{Mrk}290$	91.49	47.95	1	$\mathbf{C}$	-190	-70	-132	$((52\pm5))$	$14.20 {\pm} 0.09 {\pm} 0.07$	4.7
PG 2349-014	91.66	-60.36	1	LG	-205	-90	-142	$(51\pm 5)$	$14.19 \pm 0.09 \pm 0.09$	5.5
				MS	-415	-270	-324	$(43\pm 8)$	$14.00 \pm 0.14 \pm 0.11$	3.0
UGC12163	92.14	-25.34	2	MSe	-345	-210	-274	$(41\pm 5)$	$14.16 \pm 0.08 \pm 0.05$	6.0
H1821 + 643	94.00	27.42	4	OA	-160	-100	-122	$((22\pm5))$	$13.87 {\pm} 0.04 {\pm} 0.18$	12.0
				Oth	-225	-160	-192	$(24 \pm 5)$	$13.72 \pm 0.05 \pm 0.13$	8.0
				Oth	-285	-235	-258	$16\pm5$	$13.24 {\pm} 0.13 {\pm} 0.20$	3.0
${ m Mrk}876$	98.27	40.38	4	$\mathrm{Oth}^{\dagger}$	85	140	107	$((20\pm 5))$	$13.23 {\pm} 0.13 {\pm} 0.31$	3.0
				$\mathbf{C}$	-200	-100	-142	$((38\pm5))$	$14.05 \pm 0.04 \pm 0.13$	14.1
$\mathrm{Mrk}817$	100.30	53.48	4	$Oth^{\dagger}$	60	140	+93	$((35\pm 5))$	$13.30 \pm 0.08 \pm 0.21$	4.8
				$\mathbf{C}$	-165	-90	-116	$((27\pm4))$	$13.88 {\pm} 0.03 {\pm} 0.17$	19.2
$\mathrm{Mrk}335$	108.76	-41.42	4	MSe	-375	-235	-305	$(40\pm 4)$	$13.87 {\pm} 0.05 {\pm} 0.14$	9.0
				LG	-225	-75	-178	$((54\pm4))$	$14.14 \pm 0.03 \pm 0.10$	16.9
PG 1351 + 640	111.89	52.02	3	$\mathbf{C}$	-160	-100	-124	$((25\pm3))$	$13.67 {\pm} 0.08 {\pm} 0.23$	4.9
				$\mathrm{Oth}^{\dagger}$	100	160	125	$((27\pm4))$	$13.44 {\pm} 0.13 {\pm} 0.22$	3.1

Table 1—Continued

Name	l (°)	<i>b</i> (°)	Qa	${ m ID^b}$	$v_{min}$	$(s^{-1})$	$\bar{v}$ $(\mathrm{kms}^{-1})$	$b^{c}$ $(km s^{-1})$	$\log N \pm \sigma_{sc} \pm \sigma_{sys}$	$\frac{W_{\lambda}}{\sigma_W}$
						-				
Mrk 279	115.04	46.86	4	$^{\mathrm{C}}$	-210	-115	-154	$(34\pm 3)$	$13.67 \pm 0.05 \pm 0.13$	8.8
PG 1259 + 593	120.56	58.05	4	$\mathrm{Oth}^{\dagger}$	100	185	139	$34 \pm 7$	$13.06 \pm 0.15 \pm 0.27$	2.3
				$\mathbf{C}$	-150	-80	-110	$26\pm3$	$13.72 \pm 0.04 \pm 0.13$	14.2
Mrk 1502	123.75	-50.18	2	LG	-210	-95	-159	$(38\pm 3)$	$14.28 \pm 0.07 \pm 0.06$	7.0
PG0052+251	123.91	-37.44	2	LG	-240	-155	-193	$((21\pm3))$	$13.92 \pm 0.11 \pm 0.17$	3.5
				MSe	-415	-270	-334	$(59\pm 4)$	$14.17 \pm 0.09 \pm 0.05$	4.6
$\mathrm{Mrk}352$	125.03	-31.01	2	MSe	-365	-250	-300	$(42\pm 5)$	$13.96 \pm 0.14 \pm 0.08$	3.0
				LG	-250	-115	-185	$((48\pm6))$	$14.14 \pm 0.10 \pm 0.08$	4.6
$\mathrm{Mrk}357$	132.20	-39.14	2	LG	-220	-140	-183	$((34\pm4))$	$13.88 \pm 0.11 \pm 0.24$	3.8
				MSe	-340	-220	-279	$((44\pm4))$	$14.12 \pm 0.09 \pm 0.16$	5.5
NGC588	133.34	-31.39	2	$LG^d$	-310	-125	-212	$56\pm4$	$14.59 \pm 0.05 \pm 0.03$	9.7
				MSe	-420	-310	-372	$43\pm4$	$14.08 \pm 0.10 \pm 0.07$	4.5
NGC595	133.53	-31.31	2	M33	-215	-80	-149	$(46\pm 4)$	$14.35 {\pm} 0.07 {\pm} 0.04$	7.1
				MSe	-365	-215	-284	$(56\pm 4)$	$14.28 \pm 0.09 \pm 0.04$	4.9
Ton S180	139.00	-85.07	3	LG	-265	-100	-156	$46\pm6$	$14.18 \pm 0.05 \pm 0.04$	8.1
				Oth	220	280	251	$23 \pm 6$	$13.64 {\pm} 0.09 {\pm} 0.08$	4.7
NGC3310	156.60	54.06	4	Oth	-195	-135	-162	$(23\pm 4)$	$13.58 \pm 0.09 \pm 0.19$	4.7
$\mathrm{Mrk}106$	161.14	42.88	1	A	-150	-100	-125	$((22\pm4))$	$13.81 {\pm} 0.14 {\pm} 0.17$	3.0
PG0953+414	179.79	51.71	4	$\mathrm{EPn}^\dagger$	100	235	146	$((53\pm4))$	$13.83 \pm 0.06 \pm 0.13$	6.8
$\mathrm{Mrk}421$	179.83	65.03	4	$\mathrm{EPn}^\dagger$	100	185	135	$((34\pm4))$	$13.51 \pm 0.11 \pm 0.19$	3.4
PG0947 + 396	182.85	50.75	2	$\mathrm{EPn}^\dagger$	100	175	136	$((30\pm4))$	$14.19 \pm 0.10 \pm 0.11$	5.6
NGC3991	185.68	77.20	1	EPn	145	320	229	$(63\pm 5)$	$14.28 {\pm} 0.13 {\pm} 0.02$	3.2
HS1102 + 3441	188.56	66.22	1	$\mathrm{EPn}^\dagger$	95	210	144	$((48\pm7))$	$14.30 \pm 0.10 \pm 0.07$	4.3
PG0844 + 349	188.56	37.97	4	$\mathrm{EPn}^\dagger$	120	250	179	$(48\pm 5)$	$13.75 \pm 0.08 \pm 0.14$	4.8
PG1001+291	200.09	53.20	1	$\mathrm{EPn}^\dagger$	100	200	131	$((40\pm5))$	$13.97 {\pm} 0.13 {\pm} 0.16$	3.1
PKS 0405-12	204.93	-41.76	4	$\mathrm{Oth}^{\dagger}$	100	210	143	$(41\pm 4)$	$13.75 \pm 0.07 \pm 0.09$	6.1
NGC4670	212.69	88.63	3	Oth	320	420	363	29±4	$13.96 \pm 0.05 \pm 0.04$	8.1
PG1116+215	223.36	68.21	4	EPn	230	310	259	$(28\pm4)$	$13.28 \pm 0.13 \pm 0.30$	3.1
				EPn	115	230	181	42±4	$14.12 \pm 0.03 \pm 0.07$	19.0
Ton S210	224.97	-83.16	4	$_{ m LG}$	-250	-120	-187	$53 \pm 4$	$13.97 \pm 0.05 \pm 0.11$	8.3
$\mathrm{Mrk}734$	244.75	63.94	2	$\mathrm{EPn}^\dagger$	140	275	195	$((45\pm4))$	$14.10 \pm 0.10 \pm 0.16$	4.1
${ m HE}02264110$	253.94	-65.77	4	$\mathrm{MSe^e}$	80	260	164	59±4	$13.98 \pm 0.05 \pm 0.03$	8.8
PKS 0558-504	257.96	-28.57	3	$MSe^{e}$	210	315	258	$36 \pm 5$	$13.68 \pm 0.09 \pm 0.07$	4.5
NGC 1705	261.08	-38.74	4	$\mathrm{MS}^\dagger$	120	245	183	$((53\pm5))$	$13.78 \pm 0.04 \pm 0.41$	6.8
				MS	245	405	330	55±4	$14.31 \pm 0.02 \pm 0.14$	22.2
${ m HE}1115 – 1735$	273.65	39.64	1	$\mathrm{EPn}^\dagger$	90	175	131	$28 \pm 3$	$14.13 \pm 0.10 \pm 0.06$	5.0
IRAS F11431–1810	281.85	41.71	3	$\mathrm{EPn}^\dagger$	210	320	254	$37 \pm 5$	$13.85 \pm 0.11 \pm 0.08$	3.6

Table 1—Continued

Name	l (°)	<i>b</i> (°)	Qa	$\mathrm{ID^b}$	$v_{min}$ ( km	(max)	$\bar{v}$ ( km s <sup>-1</sup> )	$b^{c} (km s^{-1})$	$\log N \pm \sigma_{sc} \pm \sigma_{sys}$	$\frac{W_{\lambda}}{\sigma_W}$
				$\mathrm{EPn}^\dagger$	100	210	139	$((41\pm4))$	$14.25 \pm 0.06 \pm 0.12$	8.9
$\rm ESO265G23$	285.91	16.59	1	EPn	200	310	262	$(39\pm 5)$	$14.44 {\pm} 0.09 {\pm} 0.07$	6.1
$\rm ESO572G34$	286.12	42.12	3	$\mathrm{EPn}^\dagger$	100	275	171	$((65\pm4))$	$14.47 {\pm} 0.03 {\pm} 0.06$	16.6
3C273.0	289.95	64.36	4	$\mathrm{EPn}^\dagger$	105	160	125	$(16\pm 4)$	$13.17 \pm 0.11 \pm 0.33$	3.4
				$\mathrm{EPn}^\dagger$	160	260	210	$31\pm4$	$13.52 {\pm} 0.07 {\pm} 0.08$	6.3
Fairall 9	295.07	-57.83	2	MS	100	275	183	$(72 \pm 4)$	$14.33 \pm 0.07 \pm 0.07$	7.4
$\operatorname{Tol} 1247 – 232$	302.60	39.30	2	$\mathrm{EPn}^\dagger$	100	255	168	$((66\pm6))$	$14.18 {\pm} 0.10 {\pm} 0.07$	4.4
PG 1302-102	308.59	52.16	4	EPn	190	340	256	$51\pm4$	$13.95 {\pm} 0.06 {\pm} 0.04$	7.5
ESO141G55	338.18	-26.71	4	Oth	140	225	176	$(28\pm 3)$	$13.45 {\pm} 0.11 {\pm} 0.14$	3.6
$\mathrm{Mrk}1383$	349.22	55.12	4	$\mathrm{Oth}^{\dagger}$	100	160	125	$(23\pm3)$	$13.42 {\pm} 0.09 {\pm} 0.18$	5.0
$\mathrm{PKS}2005489$	350.37	-32.60	3	$\mathrm{Oth}^{\dagger}$	120	225	156	$((42\pm 5))$	$13.92 \pm 0.06 \pm 0.17$	7.9

<sup>a</sup>Data quality  $(S/N \text{ per } 20 \text{ km s}^{-1} \text{ resolution element})$ : Q = 1 (S/N = 3 - 5), Q = 2 (S/N = 5 - 9), Q = 3 (S/N = 9 - 14), Q = 4 (S/N > 14).

<sup>b</sup>HVC identification: A = Complex A, C = Complex C, EPn = Extreme Positive (North), LG = Local Group, MS = Magellanic Stream, MSe = Magellanic Stream extension, OA = Outer Arm, Oth = Other. A dagger symbol (†) indicates that the feature is also considered a high velocity "wing" feature, as described in §8.1

<sup>c</sup>Observed line width as defined in §3.3. These widths have not been corrected for the FUSE instrumental broadening ( $b_{inst} \sim 12-15 \text{ km s}^{-1}$ ). Values in parentheses are somewhat uncertain because they depend upon the integration limits adopted. Double parentheses indicate that the velocity cutoffs used for the integration are not well constrained by the data and were chosen according to the rules outlined in the text.

 $^{
m e}$ These features toward HE 0226-4410 and PKS 0558-504 are probably closely related to the MS components (see  $\S6.3$ ).

<sup>&</sup>lt;sup>d</sup>This NGC 588 component may contain a contribution from M 33 (see Wakker et al. 2002).

Table 2. Sight Lines with No High Velocity O VI Detected by FUSE

		-		, l.	1 37/0	
Name	l	<i>b</i>	$Q^{a}$	$\sigma_W^{\mathbf{b}}$	$\log N({\rm O~VI})^{\rm c}$	Note <sup>d</sup>
	(°)	(°)		(mÅ)	$(3\sigma)$	
PG 1352+183	4.37	72.87	1	51.6	<14.09	
PG 1404 + 226	21.48	72.37	1	33.6	<13.91	
NGC5548	31.96	70.50	2	29.1	<13.84	
PG 1402+261	32.96	73.46	2	24.3	<13.76	1
$ m vZ1128^e$	42.50	78.68	4	4.5	<13.04	
$\mathrm{Mrk}829$	58.76	63.25	2	21.1	<13.70	5
PG 1444+407	69.90	62.72	2	30.0	<13.86	
SBS 1415 + 437	81.96	66.20	2	25.7	<13.79	
PG 1411+442	83.83	66.35	2	42.4	<14.01	3
PG 1415+451	84.72	65.32	1	28.6	<13.84	4
$\mathrm{Mrk}487$	87.84	49.03	2	45.1	<14.03	
$\mathrm{Mrk}59$	111.54	82.12	3	9.5	<13.36	5
$\mathrm{Mrk}205$	125.45	41.67	1	52.2	<14.10	
3C249.1	130.39	38.55	2	28.2	<13.83	1,2
$\mathrm{Mrk}209$	134.15	68.08	3	14.7	< 13.55	4
PG0804+761	138.28	31.03	4	7.1	<13.23	1,2
${ m HS}0624{+}6907$	145.71	23.35	2	19.7	< 13.67	1,2
$PG0832 + 675^{e}$	147.75	35.01	3	18.3	<13.64	1,3,4
VIIZw118	151.36	25.99	4	8.4	<13.30	1,2
MS0700.7+6338	152.47	25.63	1	42.0	<14.00	1
NGC4151	155.08	75.06	3	11.1	<13.42	1,4
$\mathrm{Mrk}9$	158.36	28.75	3	16.1	< 13.59	1,2
$\mathrm{Mrk}116$	160.53	44.84	3	19.3	< 13.67	1,2
Mrk79	168.60	28.38	2	21.2	<13.70	1,2
NGC1068	172.10	-51.93	4	10.5	<13.40	1,4
NGC985	180.84	-59.49	3	14.9	< 13.55	1
Ton 1187	188.33	55.38	2	36.9	< 13.95	
$\operatorname{SBS}0335052$	191.34	-44.69	2	36.0	<13.94	
PG0832+251	199.49	33.15	1	44.4	<14.03	1
HE0238 – 1904	200.48	-63.63	1	47.3	< 14.05	1,4
$\mathrm{Mrk}1095$	201.69	-21.13	3	9.2	<13.34	1,2
$\mathrm{Mrk}36$	201.76	66.49	1	57.0	<14.14	1

OD 11	0	$\alpha$	1
Table	·/	Continuo	ച
Table	4	$\cos a$	$\overline{}$

Name	l (°)	<i>b</i> (°)	Qa	$\sigma_W^{'\mathrm{b}}$ (mÅ)	$\frac{\log N(\text{O VI})^{\text{c}}}{(3\sigma)}$	Note <sup>d</sup>
NGC 3504	204.60	66.04	1	42.2	<14.00	5
$\mathrm{Mrk}618$	206.72	-34.66	2	22.4	<13.73	1,2
PG 1004+130	225.12	49.12	3	16.3	< 13.59	1,2,4
${\rm HE}0450 – 2958$	231.13	-37.59	2	54.2	<14.11	
NGC1399	236.72	-53.63	2	50.3	<14.08	
PG 1211+143	267.55	74.32	3	16.9	<13.61	1,4
$\mathrm{Mrk}771$	269.44	81.74	1	24.1	< 13.76	
NGC4649	295.88	74.34	1	47.4	< 14.05	
PG 1307 + 085	316.79	70.71	3	18.6	< 13.65	1
${\rm HE}1326\!\!-\!\!0516$	320.07	56.07	1	45.2	<14.03	
Tol 1924–416	356.94	-24.10	2	19.3	<13.67	1

<sup>a</sup>Data quality  $(S/N \text{ per } 20 \text{ km s}^{-1} \text{ resolution element})$ : Q=1 (S/N=3-5), Q=2 (S/N=5-9), Q=3 (S/N=9-14), Q=4 (S/N>14).

<sup>b</sup>Scaled equivalent width error  $(1\sigma)$ . This error was derived from the equivalent width error found for the Galactic thick disk/halo O VI absorption along the sight line (Wakker et al. 2002; Savage et al. 2002b) and is appropriate for a velocity integration range spanning 100 km s<sup>-1</sup>. It includes statistical and continuum placement uncertainties.

<sup>c</sup>These are  $3\sigma$  limits set by the listed value of  $\sigma'_W$  and the assumption of a linear curve of growth (see §3.2).

## <sup>d</sup>Notes:

- (1) Sight line contains  $H_2$  (6–0) P(3)  $\lambda 1031.191$  absorption. Actual limit may be higher if considering absorption near  $\approx -214$  km s<sup>-1</sup>.
- (2) Sight line contains  $H_2$  (6–0) R(4)  $\lambda 1032.349$  absorption. Actual limit may be higher if considering absorption near  $\approx +123$  km s<sup>-1</sup>.
- (3) Due to other absorption features, actual limit may be higher if considering absorption at high negative velocities.
- (4) Due to other absorption features, actual limit may be higher if considering absorption at high positive velocities.
- (5) Actual limit may be higher, depending on velocity range chosen because continuum placement is difficult at high velocities.

 $^{
m e}$ Stellar sight line with z = 9.8 kpc for vZ 1128 and z = 4.7 kpc for PG 0832+675.

Table 3. O VI High Velocity Classifications

Classification	ID	#	$\langle \log N \rangle$	$\langle \bar{v} \rangle$ $(\mathrm{km}\mathrm{s}^{-1})$	$\langle b \rangle$ $(km s^{-1})$	<i>l</i> (°)	<i>b</i> (°)
Complex A	A	1	13.81	-125	22	161.1	42.9
Complex C	$\mathbf{C}$	9	13.93 (0.24)	-132 (15)	37 (18)	54.2 to 120.6	31.5 to 58.0
Extreme Positive North	EPn	19	13.96 (0.37)	181 ( 49)	42 (13)	179.8 to 308.6	16.6 to 77.2
Magellanic Stream $ (v_{LSR} > 0  \text{km s}^{-1}) $ $ (v_{LSR} < 0  \text{km s}^{-1}) $	MS MS	3	14.14 (0.31) 14.10 (0.10)	232 ( 84) -296 ( 34)	60 (10) 40 (13)	261.1 to 295.1 83.1 to 91.7	-57.8 to -38.7 -60.4 to -45.5
Magellanic Stream Ext. $ (v_{LSR} > 0 \ \rm km  s^{-1}) $ $ (v_{LSR} < 0 \ \rm km  s^{-1}) $	MSe MSe	2 10	13.83 (0.21) 14.18 (0.19)	211 ( 66) -304 ( 29)	47 (16) 47 (7)	253.9 to 258.0 63.7 to 133.5	-65.8 to -28.6 -58.8 to -25.3
Outer Arm	OA	2	14.01 (0.19)	-106 ( 22)	26 ( 6)	61.3 to 94.0	17.5 to 27.4
Local Group	LG	19	14.08 (0.26)	-182 ( 54)	43 (12)	17.7 to 225.0	−85.1 to −29.9
Other $(v_{LSR} > 0 \text{ km s}^{-1})$ $(v_{LSR} < 0 \text{ km s}^{-1})$	Oth Oth	13 3	13.59 (0.31) 13.51 (0.25)	180 ( 94) -204 ( 49)	32 ( 8) 21 ( 4)	36.0 to 350.4 94.0 to 156.6	-85.1 to 88.6 27.4 to 54.1

Table 4. High Velocity O VI Detection Summary

$\Sigma W_{\lambda}$ Threshold	Number of Sight Lines with $\left[\frac{W_{\lambda}}{\sigma_W}\right]_{tot} > 3.0^{\text{ a,b}}$								
(mÅ)	All $Q$	Q = 1	Q = 2	Q=3	Q = 4				
30	59 (58%) <sup>c</sup>	11 (48%) <sup>c</sup>	14 (47%) <sup>c</sup>	12 (52%) <sup>c</sup>	22 (85%)				
50	$55 (54\%)^{c}$	11 (48%) <sup>c</sup>	$14 (47\%)^{c}$	$12 (52\%)^{c}$	18 (69%)				
100	40 (39%)	9 (39%)	13~(43%)	7 (30%)	11 (42%)				
150	27~(26%)	6~(26%)	9(30%)	7 (30%)	5~(19%)				
200	19 (19%)	3~(13%)	7~(23%)	5~(22%)	4~(15%)				

<sup>a</sup>Number of sight lines (and percentages) with total integrated high velocity O VI  $\lambda 1031.926$  equivalent widths,  $\Sigma W_{1032}$ , greater than the listed equivalent width threshold.

<sup>b</sup>There are 102 sight lines in the sample: 23 with  $Q=1,\ 30$  with  $Q=2,\ 23$  with  $Q=3,\ and\ 26$  with Q=4.

<sup>c</sup>These Q=1-3 values should be treated with caution since the data quality is not sufficient to reliably exclude weak features. These values are likely to be lower limits if the Q=4 values are representative of the true detection frequency (see text).

Table 5. High Velocity O VI Sky Covering Percentages – Column Densities  $^{\rm a}$ 

Galactic Region	Sight Lines in Sample	$1.0\times10^{13}$		umn Density $5.0 \times 10^{13}$		- ' '	$2.5 \times 10^{14}$
All Sky	102	59 (58%)	55 (54%)	48 (47%)	38 (37%)	31 (30%)	6 (6%)
$0^{\circ} < l < 180^{\circ}$							
$b < 0^{\circ}$	20	19 (95%)	18 (90%)	15 (75%)	11 (55%)	9 (45%)	1 (5%)
$b > 0^{\circ}$	40	16 (40%)	16 (40%)	15 (38%)	12 (30%)	11 (28%)	2 (5%)
$180^{\circ} < l < 360^{\circ}$							
$b < 0^{\circ}$	16	8 (50%)	7 (44%)	6 (38%)	6 (38%)	4 (35%)	1 (6%)
$b > 0^{\circ}$	26	16 (62%)	14 (54%)	12 (46%)	9 (35%)	7 (27%)	2 (8%)

<sup>&</sup>lt;sup>a</sup>Number (percentage) of sight lines for which  $\sum N(\text{O VI})_{\text{HV}} \geq N_0$ . Entries for  $N_0 < 10^{14} \text{ cm}^{-2}$  should be treated as provisional since data quality may prevent detection of weaker features along some sight lines.

Table 6. Velocity Centroid Means and Standard Deviations<sup>a</sup>

Reference Frame	Longitude Range	b < 0°	$b > 0^{\circ}$	All b
Local Standard of Rest	$0^{\circ} < l < 180^{\circ}$	$-205 \pm 127$	$-38 \pm 158$	$-138 \pm 162$
	$180^\circ < l < 360^\circ$	$156\pm142$	$193 \pm 64$	$181 \pm 95$
	All $l$	$-129\pm196$	$66 \pm 170$	$-33 \pm 207$
Galactic Standard of Rest	$0^{\circ} < l < 180^{\circ}$	$-85 \pm 111$	$88 \pm 142$	$-15 \pm 150$
	$180^\circ < l < 360^\circ$	$55 \pm 106$	$108 \pm 92$	$91 \pm 98$
	All $l$	$-56 \pm 123$	$97 \pm 121$	$20 \pm 144$
Local Crown Standard of Doct	$0^{\circ} < l < 180^{\circ}$	$-40 \pm 110$	$94 \pm 136$	$14 \pm 137$
Local Group Standard of Rest	$180^{\circ} < l < 360^{\circ}$	$-40 \pm 110$ $56 \pm 94$		$65 \pm 102$
	All $l$	$-19 \pm 113$	$82 \pm 124$	$31 \pm 128$
		Number of H	ligh Velocity	O VI Features
	$0^{\circ} < l < 180^{\circ}$	[34]	[23]	[57]
	$180^\circ < l < 360^\circ$	[ 9]	[19]	[28]
	All $l$	[43]	[42]	[85]

<sup>&</sup>lt;sup>a</sup>Velocity centroid means,  $\langle \bar{v} \rangle$ , and standard deviations,  $\sigma_{\langle \bar{v} \rangle}$ , of the high velocity O VI features. All velocities are in km s<sup>-1</sup>. The number of features in each longitude-latitude interval is listed in square brackets below the velocity entries.

Table 7. High Velocity O VI Sky Covering Percentages – Centroid Velocities<sup>a</sup>

Velocity Threshold $v_0 \; (\mathrm{km}\mathrm{s}^{-1})$	All Sky	$\frac{0^{\circ} < l}{b < 0^{\circ}}$	$\frac{<180^{\circ}}{b>0^{\circ}}$	$\frac{180^{\circ} <}{b < 0^{\circ}}$	$\frac{l < 360^{\circ}}{b > 0^{\circ}}$
-300 $-250$ $-200$ $-150$ $-90$	8 ( 8%) [ 8%]	8 (40%)	0 ( 0%)	0 ( 0%)	0 ( 0%)
	16 (16%) [12%]	15 (75%)	1 ( 3%)	0 ( 0%)	0 ( 0%)
	18 (18%) [19%]	17 (85%)	1 ( 3%)	0 ( 0%)	0 ( 0%)
	24 (24%) [31%]	19 (95%)	4 (10%)	1 ( 6%)	0 ( 0%)
	33 (32%) [42%]	19 (95%)	13 (33%)	1 ( 6%)	0 ( 0%)
90	33 (32%) [58%]	2 (10%)	8 (20%)	7 (44%)	16 (62%)
150	20 (20%) [31%]	2 (10%)	1 ( 3%)	6 (38%)	11 (42%)
200	11 (11%) [15%]	1 ( 5%)	1 ( 3%)	2 (13%)	7 (27%)
250	9 ( 9%) [12%]	1 ( 5%)	1 ( 3%)	2 (13%)	5 (19%)
300	3 ( 3%) [ 4%]	0 ( 0%)	1 ( 3%)	1 (6%)	1 (4%)
# Sight Lines <sup>b</sup>	102 [26]	20	40	16	26

aNumber (percentage) of sight lines in the sample that contain at least one high velocity O VI feature with either  $\bar{v} \leq v_0$  (for  $v_0 < 0 \, \mathrm{km \, s^{-1}}$ ) or  $\bar{v} \geq v_0$  (for  $v_0 > 0 \, \mathrm{km \, s^{-1}}$ ). Data quality affects these percentages since weak features are below the detection limits for some sight lines (i.e., these values should probably be treated as lower limits – see text). Values listed in square brackets [] are for the highest quality (Q=4) sight lines only.

 $<sup>^{\</sup>mathrm{b}}\mathrm{Number}$  of sight lines in each longitude-latitude region.

Table 8. H I - O VI Comparison for Complex C Sight Lines

Sight Line	l (°)	b (°)	$\bar{v}_{\mathrm{HI}}{}^{\mathrm{a}}$ ( km s <sup>-1</sup> )	$N({ m H~I})^{ m a}$ $(10^{18}~{ m cm}^{-2})$	$\bar{v}_{ m OVI}$ $({ m kms^{-1}})$	$N({ m O~VI})$ $(10^{13}~{ m cm}^{-2})$	$\bar{v}_{\mathrm{HI}}$ - $\bar{v}_{\mathrm{OVI}}$ ( km s <sup>-1</sup> )	$\frac{N(HI)}{N(OVI)}$ $(x10^5)$	Note
Mrk 279	115.04	46.86	-137/[-102]	20.4/[12.3]	-154	4.68	-17	4.4	1
$\mathrm{Mrk}290$	91.49	47.95	-134/[-105]	94.7/[38.5]	-132	15.8	+2	6.0	1
$\mathrm{Mrk}501$	63.60	36.86	-116	10.7	-122	6.46	-6	1.7	
$\mathrm{Mrk}506$	54.18	31.50	-155	4.4	-144	11.2	+11	0.4	
$\mathrm{Mrk}817$	100.30	53.48	-109	32.4	-116	7.59	(-7)	4.3	2
$\mathrm{Mrk}876$	98.27	40.38	[-173]/-133	[4.7]/19.9	-142	11.2	(-9)	1.8	1,2
PG 1259+593	120.56	58.05	-128	89.5	-110	5.25	+18	17.	
PG 1351+640	111.89	52.02	-154/[-115]	59.6/[7.7]	-124	5.68	(+30)	13.	1,2
PG 1626+554	84.51	42.19	-131	26.9	-152	22.4	-21	1.2	
Averages:			•••				$-2\pm15$	$5.5 \pm 5.7$	3,4

<sup>&</sup>lt;sup>a</sup>Values derived from Effelsberg H I 21 cm spectra. Values in brackets [ ] indicate secondary features.

<sup>&</sup>lt;sup>b</sup>Notes:

<sup>(1)</sup> Values for  $\bar{v}_{\rm HI} - \bar{v}_{\rm OVI}$  and  $N({\rm H~I})/N({\rm O~VI})$  do not include the H I components listed in brackets.

<sup>(2)</sup> Velocity difference is uncertain because  $\bar{v}_{\rm OVI}$  relies on integration limits that are based on something other than the O VI data (i.e., the H I velocity structure).

<sup>(3)</sup> If the uncertain values listed in parentheses are included, the average of  $\bar{v}_{\rm HI} - \bar{v}_{\rm OVI}$  becomes  $0 \pm 17~{\rm km\,s^{-1}}$ .

<sup>(4)</sup> The quoted uncertainties are standard deviations of the mean values.

Table 9. High Velocity H I 21 cm Emission Features with No O VI

Object	l (°)	<i>b</i> (°)	$\bar{v}_{21cm} (\mathrm{km}\mathrm{s}^{-1})$	$\frac{\log N(\mathrm{H~I})^{\mathrm{a}}}{(3\sigma)}$	$\log N({\rm O~VI})^{\rm b}$	$Q^{\mathrm{c}}$	Comment
PG 0052+251 Mrk 205 HS 0624+6907 Mrk 116 Ton 1187 ESO 265-G23	123.91 125.45 145.71 160.53 188.33 285.91	-37.44 41.67 22.35 44.84 55.38 16.59	-121 $-202$ $-100$ $-170$ $-104$ $+117$	18.60 19.21 19.32 19.33 19.23 19.71	$< 13.72$ $< 13.79$ $< 13.61$ $< 13.49$ $< 13.65$ $< 13.86^{d}$	2 1 2 3 2	WW478 WW84 Outer Arm Complex A Complex M Complex WD

<sup>&</sup>lt;sup>a</sup>The H I 21 cm emission profiles are shown in Figure 1 of Wakker et al. (2002).

 $<sup>^</sup>b O$  VI column density limit over an integration range of  $\approx 50~\rm km\,s^{-1}$  centered on the observed velocity of the H I 21 cm emission.

 $<sup>^{\</sup>mathrm{c}}\mathrm{Data}$  quality of the FUSE observation.

 $<sup>^{\</sup>rm d}{\rm A}$  higher quality FUSE Guest Investigator observation obtained recently by B.K. Gibson and colleagues confirms this non-detection.

Table 10. Velocity Summary of Possible Local Group Features<sup>a</sup>

Reference Frame	$\langle \bar{v} \rangle$ ( km s <sup>-1</sup> )	$\begin{array}{c} \sigma_{\langle \bar{v} \rangle} \\ (\mathrm{km}\mathrm{s}^{-1}) \end{array}$
Local Standard of Rest	-53	214
Galactic Standard of Rest	-22	123
Local Group Standard of Rest	-21	63

 $^{
m a}$ The 50 O VI absorption features considered have classifications of EPn, MSe, or LG as defined in Table 3.

Table 11. High Ion Column Density Ratios

Sight Line	$\bar{v}$ ( km s <sup>-1</sup> )	ID	$\log N({\rm O~VI})$	$\frac{N(\text{O VI})}{N(\text{C IV})}$	$\frac{N(\text{O VI})}{N(\text{N V})}$	Notes <sup>b</sup>
$\mathrm{Mrk}509$	-247	LG	14.24	< 0.3	< 0.2	1
PKS 2155-304	-232	LG	13.57	$\sim 1$	> 3	2
	-129	LG	13.80	$\sim 2$	> 4.6	2
NGC 1705	+330	MS	14.31	> 3		3
Fairall 9	+183	MS	14.33	$\sim 7$	> 3	4
PG 1259+593	-110	$\mathbf{C}$	13.72	$\sim 3.5$	> 3.8	5
$\langle { m Galactic~Halo} \rangle$	$\sim 0$		$\sim 14.37 \pm 0.18$	$\sim 1.5$	$\sim 5$	6
Model Predictions <sup>a</sup>						
Turbulent Mixing				0.1-0.8	2.5-8	7
Radiative Cooling	•••		• • •	2-10	7 - 14	8
Conduction			• • •	1.6–4.5	4–7	9
Supernova Remnants	•••			5-10	12–16	10
C.I.E. $(T < 2 \times 10^5 \mathrm{K})$			•••	< 2.6	< 0.7	11
C.I.E. $(T = 3 \times 10^5 \mathrm{K})$				134	50	11
C.I.E. $(T = 5 \times 10^5 \mathrm{K})$				50	47	11
Photo. $(n_H = 10^{-5} \text{ cm}^{-3})$				1.0	3.6	12
Photo. $(n_H = 10^{-4} \text{ cm}^{-3})$				0.01	0.5	12

 $<sup>^{\</sup>mathrm{a}}\mathrm{Model}$  predictions assume solar abundance ratios unless otherwise noted.

<sup>&</sup>lt;sup>b</sup>Notes: (see next page)

## Table 11 (continued)

## Notes:

- (1) C IV and N V from Sembach et al. (1999). The values listed are the sums for the two C IV-HVCs along the sight line at -283 and -228 km s<sup>-1</sup>. An additional high velocity O VI feature at  $\bar{v} = -143$  km s<sup>-1</sup> (see Table 1) has no obvious counterpart in C IV or N V.
- (2) C IV and N V from Sembach et al. (1999).
- (3) C IV from Sembach (2002). Continuum placement for C IV is difficult.
- (4) C IV from Lu, Savage, & Sembach (1994).
- (5) C IV and N V from extant STIS data. See Fox et al. (2002).
- (6) Galactic halo averages from data compiled by Sembach, Savage, & Tripp (1997), Savage, Sembach, & Lu (1997), and Savage et al. (2002b).
- (7) Turbulent mixing layer results from Slavin, Shull, & Begelman (1993) for TMLs with post-mixed temperatures  $T = (1-3) \times 10^5 \,\mathrm{K}$  and hot gas entrainment velocities of  $25-100 \,\mathrm{km}\,\mathrm{s}^{-1}$ .
- (8) Radiative cooling results from Edgar & Chevalier (1986) for a range of models with varying assumptions about the transition of the flow from isochoric to isobaric cooling.
- (9) Magnetized thermal conduction front results from Borkowski, Balbus, & Fristrom (1990) for a range of magnetic field orientations inclined between  $0^{\circ}$  to  $60^{\circ}$  to the face of the cloud at an age of  $2.5 \times 10^{5}$  years.
- (10) Evolved supernova remnant results from Slavin & Cox (1992) for isolated explosions in a medium with densities of  $0.1-0.3~{\rm cm^{-3}}$  and  $B\approx 1\mu{\rm G}$ . Values are for remnants with ages of  $4\times 10^5$  to  $5\times 10^6$  years.
- (11) Collisional ionization equilibrium ratios assuming solar abundance ratios (Sutherland & Dopita 1993; Holweger 2001).
- (12) Photoionization model results shown in Figure 19. The values quoted are appropriate for models with  $N({\rm H~I}) = 10^{14}~{\rm cm}^{-2}$ , a metallicity of  $\sim 1/3$  solar, and a solar relative abundance pattern. If the relative abundances are not in their solar proportions (e.g., if N/O is sub-solar as appears to be the case for Complex C), the ratios may differ from those plotted. Higher values of  $N({\rm H~I})$  result in lower ratios. See §9.2 for additional descriptions of the model.

Table 12. Means and Standard Deviations of  $\Delta v$   $^{\mathrm{a},b}$ 

Rotation Model	Longitude Range	$b < 0^{\circ}$	$b > 0^{\circ}$	All b
Corotating Halo	$l < 180^{\circ}$ $l > 180^{\circ}$ All $l$	$-110 \pm 88$ $71 \pm 81$ $-72 \pm 113$	$8 \pm 76$ $94 \pm 65$ $47 \pm 83$	$-62 \pm 101$ $86 \pm 70$ $-13 \pm 115$
Decoupled Halo	$l < 180^{\circ}$ $l > 180^{\circ}$ All $l$	$-27 \pm 76$ $0 \pm 56$ $-22 \pm 73$	$70 \pm 71$ $33 \pm 89$ $52 \pm 81$	$11 \pm 87$ $23 \pm 80$ $15 \pm 84$

 $<sup>^{\</sup>rm a} \rm Values$  listed are  $\langle \Delta v \rangle \pm \sigma_{\langle \Delta v \rangle}.$  All velocities are in  $\,\rm km\,s^{-1}.$ 

 $<sup>{}^{\</sup>mathrm{b}}\Delta v=\bar{v}-v_{pred}.$  See Table 1 for values of  $\bar{v}.$ 

This figure "f1.png" is available in "png" format from:

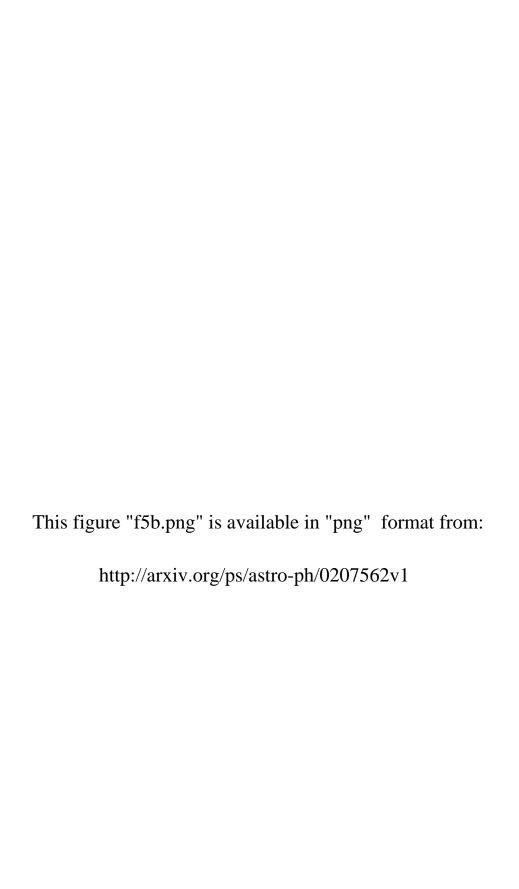
This figure "f2.png" is available in "png" format from:

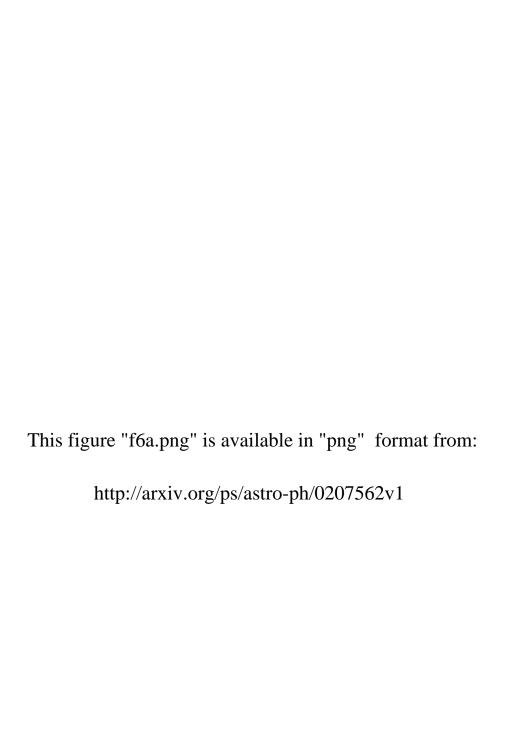
This figure "f3a.png" is available in "png" format from:

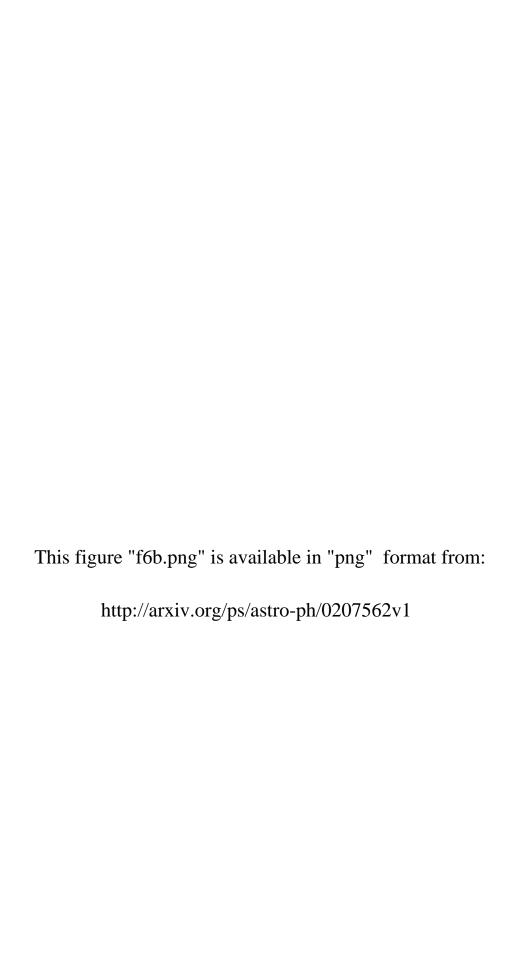
This figure "f3b.png" is available in "png" format from: http://arxiv.org/ps/astro-ph/0207562v1

This figure "f4.png" is available in "png" format from:

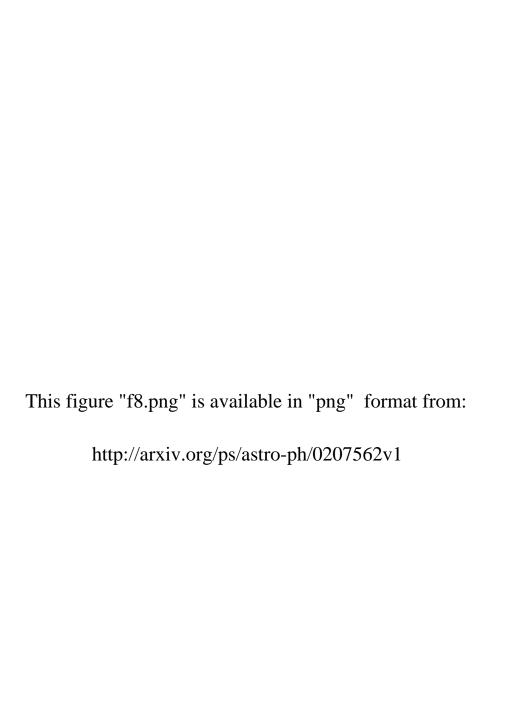
This figure "f5a.png" is available in "png" format from:



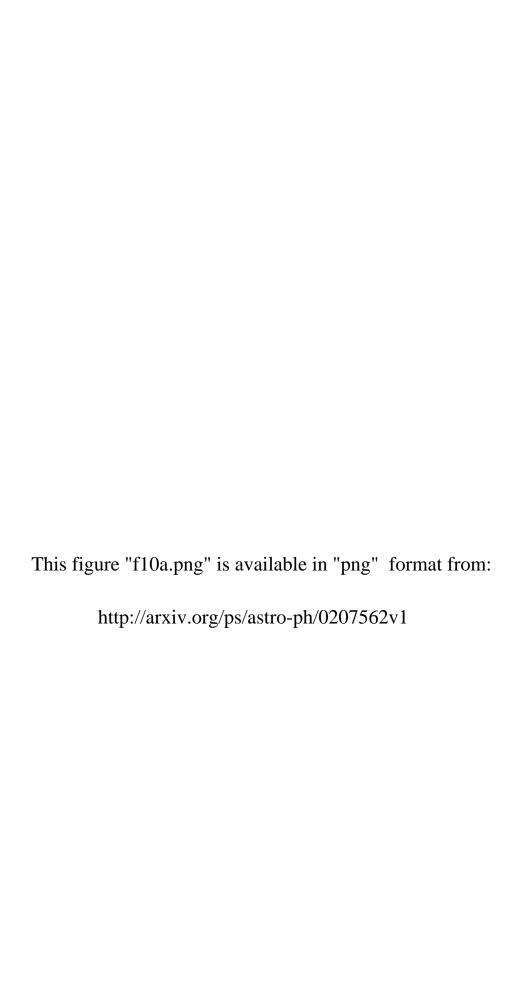


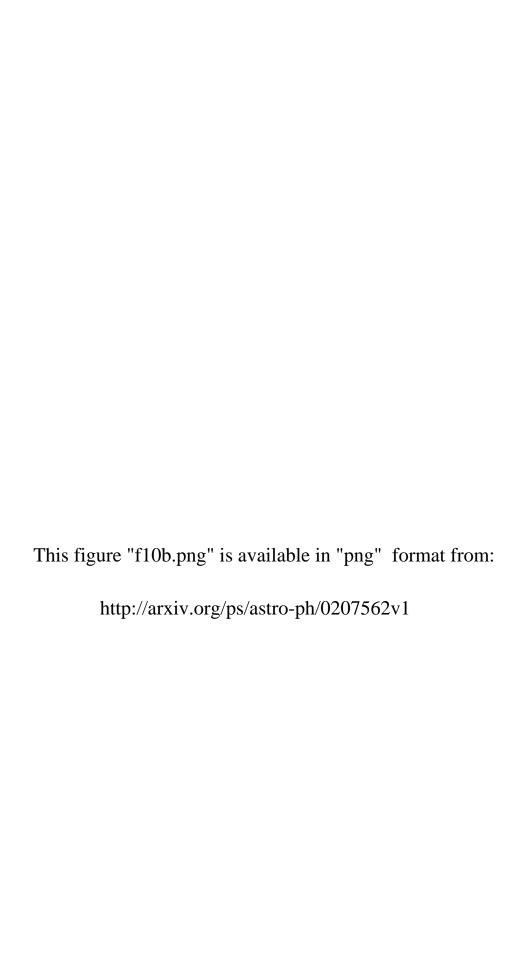


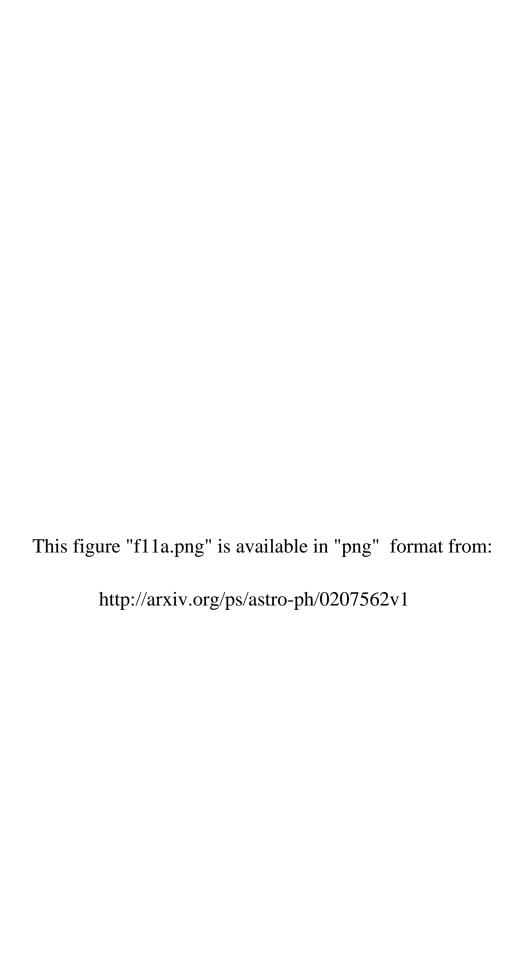
This figure "f7.png" is available in "png" format from:

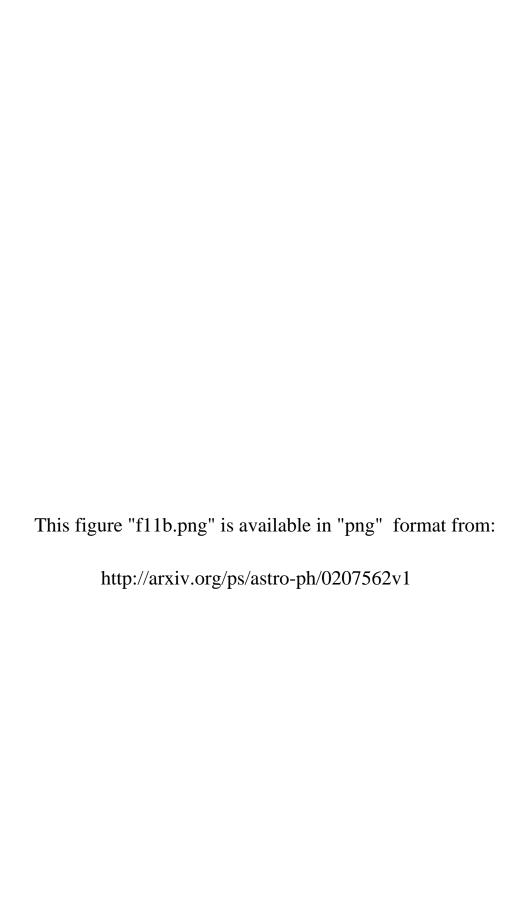


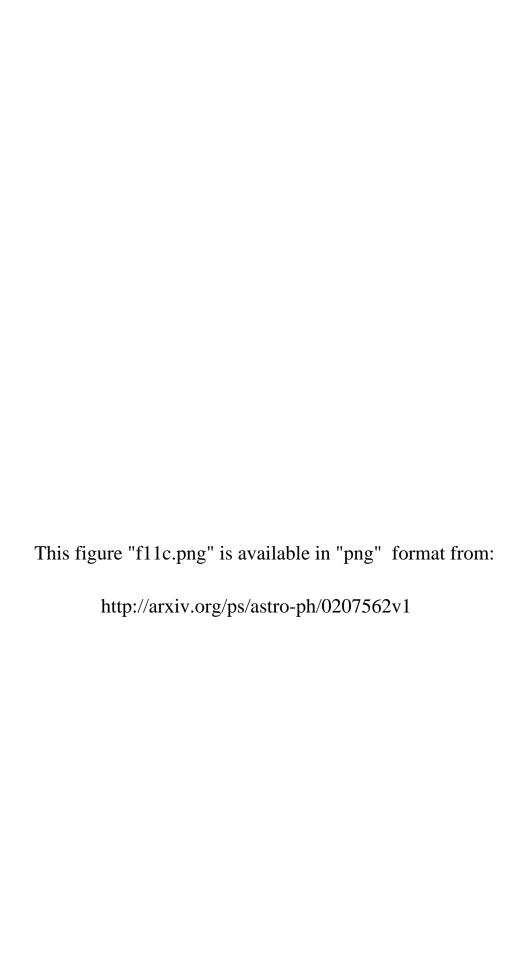
This figure "f9.png" is available in "png" format from:











This figure "f12.png" is available in "png" format from:

This figure "f13a.png" is available in "png" format from:

http://arxiv.org/ps/astro-ph/0207562v1

This figure "f13b.png" is available in "png" format from: http://arxiv.org/ps/astro-ph/0207562v1

This figure "f14.png" is available in "png" format from:

This figure "f15.png" is available in "png" format from:

This figure "f16.png" is available in "png" format from: http://arxiv.org/ps/astro-ph/0207562v1

This figure "f17.png" is available in "png" format from:

This figure "f18.png" is available in "png" format from:

This figure "f19.png" is available in "png" format from:

This figure "f20.png" is available in "png" format from:

This figure "f21.png" is available in "png" format from:

This figure "f22.png" is available in "png" format from:

This figure "f23.png" is available in "png" format from:

This figure "f24.png" is available in "png" format from: